2023

SER14-RPN6 PHOSPHORYLATION MEDIATES THE ACTIVATION OF 26S PROTEASOMES BY CYCLIC AMP AND PROTECTS AGAINST CARDIAC PROTEOTOXIC STRESS IN MICE

Liuqing Yang

SER14-RPN6 PHOSPHORYLATION MEDIATES THE ACTIVATION OF 26S PROTEASOMES BY CYCLIC AMP AND PROTECTS AGAINST CARDIAC PROTEOTOXIC STRESS IN MICE

By

Liuqing Yang

B.S., The Hong Kong Polytechnic University, Hong Kong, 2013
M.S., University of Illinois at Chicago, 2015

A Dissertation Submitted in Partial Fulfillment of the Requirements for the Degree of Doctor of Philosophy

---

Division of Biomedical Sciences

Basic Biomedical Sciences Program
In the Graduate School
The University of South Dakota
August 2023

The members of the Committee appointed to examine
the Dissertation of Liuqing Yang find it
satisfactory and recommend that it be accepted.

Chairperson

DocuSigned by:
Xuejun Wang
E0DF2ED7B582479...

DocuSigned by:
Yifan Li
AE32C7B4EBBE406...

DocuSigned by:
Khosrow Pezvani
55F3B8D0E065450...

DocuSigned by:
Hongmin Wang
C6A404A4E08B404...

DocuSigned by:
Hong Zheng
A669B3E3E65348D...

ABSTRACT

A better understanding of how proteasome activity is regulated can facilitate the search for proteasome enhancement strategies for disease treatment. A cell culture study shows cAMP-dependent protein kinase (PKA) activates 26S proteasomes by phosphorylating Ser14 of RPN6 (pS14-RPN6), but this discovery and its physiological significance remain to be established *in vivo*. To test the hypothesis that pS14-RPN6 mediates the activation of proteasomes by PKA and reduces proteotoxicity in animals, two knock-in mouse models with Ser14 of endogenous Rpn6 mutated to either Ala (S14A) or Asp (S14D) to respectively block or mimic pS14-Rpn6 were created. In a PKA-dependent manner, cAMP augmentation increased pS14-Rpn6 and 26S proteasome activities in wild-type (WT) but not S14A embryonic fibroblasts (MEFs), adult cardiomyocytes (AMCMs), and mouse hearts. Basal 26S proteasome activities were significantly greater in the myocardium and AMCMs from S14D mice than those from WT mice. When coupled with transgenic mice expressing GFPdgn (a proven UPS substrate), significantly lower myocardial GFPdgn protein but not mRNA levels were observed in S14D::GFPdgn mice compared with littermate GFPdgn control mice. In $CryAB^{R120G}$ mice, a model of cardiac proteotoxicity, basal myocardial pS14-Rpn6 was significantly lower compared with non-transgenic littermates at both 3 and 6 months of age, which was not always associated with reduction of other phosphorylated PKA substrates. Proteasomal degradation of $CryAB^{R120G}$ was faster in cultured S14D neonatal mouse cardiomyocytes (NMCMs) than in WT NMCMs. Compared with $CryAB^{R120G}$ mice, S14D::$CryAB^{R120G}$ mice showed significantly greater myocardial proteasome activities, lower levels of total and K48-linked ubiquitin conjugates and of aberrant $CryAB^{R120G}$ protein aggregates, less reactivation of fetal genes and cardiac hypertrophy, and delays in cardiac malfunction and premature death. This study establishes in animals that pS14-Rpn6 is responsible for the activation of 26S proteasomes by PKA and reduced pS14-Rpn6 is a key pathogenic factor in cardiac proteinopathy, thereby identifies a new therapeutic target to reduce cardiac proteotoxicity.

Advisor Approval Signature: 

Xuejun Wang, M.D., Ph.D.

ACKNOWLEDGEMENT

First and foremost, I would like to express my sincerest appreciation to my advisor, Dr. Xuejun Wang, for his unwavering dedication and support over the past 6 years. He has given me endless opportunities to learn and manage responsibilities as a scientific researcher and to attend and present at conferences which significantly enriched my experience. I have learned a great deal from his expertise and insights, which have been instrumental in shaping the direction of my personal and professional growth. Working under the guidance of Dr. Wang has been an exceptional privilege.

I would also like to express my gratitude to my dissertation committee: Drs. Yifan Li, Khosrow Rezvani, Hongmin Wang, Hong Zheng, and Douglas Martin. I am grateful for them taking extra time to serve on my committee and offering insightful feedback and help.

I am deeply thankful for the resources, support, and guidance provided by the Division of Basic Biomedical Sciences.

My heartfelt gratitude also goes out to all the present and former members of the Wang Lab for their support and assistance as well as friendship: Nirmal Parajuli, Penglong Wu, Samiksha Giri, Mingqi Cai, Md Salim Ahammed, Jose Lira, Jack Sternburg, Mark Bouska, Megan Lewno, Hanming Zhang, Bo Pan, and Addilyn Hillinger. I want to express my special thanks to Jessica Freeling for teaching me the animal physiological assessments.

And lastly, I would like to acknowledge and extend my deepest appreciation to my family and friends, whose love, understanding, and support have been a constant source of strength throughout my academic pursuit. Their encouragement during challenging times kept me motivated.

LIST OF ABBREVIATIONS AND ACRONYMS

Ad: Adenovirus

Ala: Alanine

AMCM: Adult mouse cardiomyocyte

ANF: Atrial natriuretic factor

ANOVA: Analysis of variance

ARMS-PCR: Amplification refractory mutation system-polymerase chain reaction

Asp: Aspartic acid

ATP: Adenosine triphosphate

AUC: Area under curve

BAG3: Bcl-associated athanogene 3

BCA: Bicinchoninic acid

BDM: 2,3-butanedione monoxime

BNP: Brain natriuretic peptide

BSA: Bovine serum albumin

BW: Body weight

BZM: Bortezomib

CaMKII: Calcium/calmodulin-dependent protein kinase II

cAMP: Cyclic adenosine monophosphate

CDK: Cyclin-dependent kinase

CD lipid: Chemically defined lipid concentrate

cGMP: Cyclic guanosine monophosphate

CHIP: Carboxyl-terminus of heat shock protein 70-interacting protein

cMyBP-C: Cardiac myosin-binding protein C

CO: Cardiac output

CryAB: αB-crystallin

$CryAB^{R120G}$: R120G-mutant CryAB

DMEM: Dulbecco's modified Eagle's medium

DMSO: Dimethyl sulfoxide

DRC: Desmin-related cardiomyopathy

DRM: Desmin-related myopathy

DTT: Dithiothreitol

DUB: Deubiquitinating enzyme

DYRK2: Dual-specificity tyrosine-regulated kinase 2

E1: Ubiquitin activating enzyme

E2: Ubiquitin conjugating enzyme

E3: Ubiquitin ligase

E4: Ubiquitin elongation factor

ECL: Enhanced chemiluminescence

EF: Ejection fraction

ER: Endoplasmic reticulum

FBS: Fetal bovine serum

FS: Fractional shortening

Fsk: Forskolin

GFP: Green fluorescent protein

Gly: Glycine

HA: Hemagglutinin

HECT: Homologous to the E6-AP C terminus

HFpEF: Heart failure with preserved ejection fraction

HFrEF: Heart failure with reduced ejection fraction

HOIP: HOIL-1L interacting protein

HR: Heart rate

HSP: Heat shock protein

HW: Heart weight

IFN: Interferon

IPTS: Increased proteotoxic stress

I/R: Ischemia/reperfusion

ITS: Insulin, transferrin, selenium

JAMM: JAB/MPN/MOV34 metalloenzyme

K: Lysine

L.C.: Loading control

LUBAC: Linear ubiquitin chain assembly complex

LUBEL: Linear ubiquitin E3 ligase

LV: Left ventricle/ventricular

LVEDV: LV end-diastolic volume

LVESV: LV end-systolic volume

LVID;d: End-diastolic LV internal diameter

LVID;s: End-systolic LV internal diameter

LVPW;d: End-diastolic LV posterior wall thickness

LVPW;s: End-systolic LV posterior wall thickness

M1: Ubiquitin N-terminal methionine

M2: Muscarinic 2

MEF: Mouse embryonic fibroblast

MINDY: Motif interacting with ubiquitin-containing novel DUB family

MJD: Machado-Joseph disease protease

MOI: Multiplicities of infection

NMCM: Neonatal mouse cardiomyocyte

NRCM: Neonatal rat cardiomyocyte

ns: Not significant

OTU: Ovarian tumor protease

PA28: Proteasome activator 28

PAM: protospacer adjacent motif

PARP1: Poly(ADP-ribose)polymerase-1

PBS: Phosphate-buffered saline

PCR: Polymerase chain reaction

PDE: Phosphodiesterase

PFA: Paraformaldehyde

PFI: Proteasome functional insufficiency

Picl: Piclamilast

PKA: cAMP-dependent protein kinase; protein kinase A

PKG: cGMP-dependent protein kinase; protein kinase G

PP2A: Protein phosphatase 2A

PQC: Protein quality control

P/S: Penicillin/Streptomycin

pS14-Rpn6: Serine14-phophorylated Rpn6

PVDF: Polyvinylidene difluoride

qPCR: quantitative real-time PCR

R120G: Transgenic CryAB^{R120G}

RING: Really interesting new gene

Rpn: Regulatory particle non-ATPase

Rpt: Regulatory particle triple A-ATPase

ROS: Reactive oxygen species

RT-PCR: Reverse transcription-PCR

S14A: Rpn6/Psmd11^{S14A}

S14D: Rpn6/Psmd11^{S14D}

SD: Standard deviation

SDS: sodium dodecyl sulfate

SDS-PAGE: SDS-polyacrylamide gel electrophoresis

SEM: Standard error of the mean

Ser: Serine

sGC: Soluble guanylate cyclase

Smad: Suppressor of mothers against decapentaplegic

Smurf: Smad ubiquitination regulatory factor

SV: Stroke volume

TAC: Transverse aortic constriction

TBST: Tris-buffered saline containing 0.2% Tween-20

TEMED: N,N,N',N'-Tetramethylethylenediamine

tg: Transgenic

TGF: Transforming growth factor

TNF: Tumor necrosis factor

Ub: Ubiquitin

UCH: Ubiquitin carboxyl-terminal hydrolase

UPS: Ubiquitin-proteasome system

USP/UBP: Ubiquitin-specific proteases

VW: Ventricular weight

WT: Wild-type

WWP2: WW domain-containing E3 ubiquitin protein ligase 2

ZUFSP: Zinc finder with UFM1-specific peptidase domain protein

TABLE OF CONTENTS

LIST OF TABLES

TABLE PAGE

LIST OF FIGURES

FIGURE PAGE

INTRODUCTION

1. Protein quality control (PQC) and the ubiquitin proteasome system (UPS)

A polypeptide after ribosomal synthesis undergoes folding and assembly processes to acquire and maintain a proper three-dimensional structure that is vital to ensuring normal functioning of the protein and cell integrity.[1] Even though the amino acid sequence of a polypeptide dictates its ultimate conformation and folding is thermodynamically preferred, the folding process is challenging: an enormous amount of energy is required for chaperones to assist in folding;[2] stochastic mistakes might happen during folding; a protein must be conformationally flexible to function properly, which makes its structure thermodynamically unstable.[3] Genetic mutations or environmental stress, such as heat and radiation, can interrupt proper folding and lead to protein misfolding, resulting in protein dysfunction and aberrant aggregation in the cell.[4] To maintain proper protein folding and minimize the cellular toxicity of misfolded proteins, the cell in nature has evolved a set of multi-layered protein quality control (PQC) mechanisms that assist in folding and refolding of polypeptides and prompt removal of terminally misfolded proteins.[5] The demand for PQC is greater in cells with higher metabolic activity such as cardiomyocytes. PQC is carried out by collaboration between molecular chaperones and targeted protein degradation. Molecular chaperones surveille the protein integrity and participate in the folding of newly synthesized proteins and refolding of misfolded proteins. Targeted protein degradation includes the ubiquitin-proteasome system (UPS)-mediated protein degradation and lysosome-executed autophagy. When the chaperones are overwhelmed by misfolded protein overload and no longer able to repair them, terminally misfolded individual protein molecules will be channeled for degradation by the UPS or chaperone-mediated autophagy. Otherwise, misfolded proteins form aggregates that may be removed by macroautophagy.[6]

The UPS is responsible for the degradation of the vast majority of intracellular proteins. By targeted and timely degradation of terminally misfolded proteins, the UPS is pivotal to PQC which senses and minimizes the level and toxicity of misfolded proteins.[7] The UPS also plays a vital regulatory role by removing normal but no longer needed proteins in the cell, such as transcription factors,[8] signaling proteins,[9,10] cell cycle regulators,[11] and cell death regulators.[12] The UPS carries out protein degradation in the cytoplasm and nucleus of the cell.[13,14] UPS-mediated proteolysis generally consists of two sequential steps: covalent attachment of a substrate protein with a chain of ubiquitin molecules and subsequent degradation of the ubiquitinated protein by the 26S proteasome.[15]

1.1. Ubiquitin and ubiquitination

Ubiquitin is a 76-amino acid protein, which is evolutionarily conserved in nearly all eukaryotic cells. Ubiquitination is an ATP-dependent process in which ubiquitin is covalently attached to the substrate protein or a preceding ubiquitin, via a cascade of enzymatic reactions catalyzed by the ubiquitin-activating enzyme E1, ubiquitin-conjugating enzymes E2, and ubiquitin ligases E3.[16,17] E1 first utilizes ATP to activate the C-terminus of ubiquitin by forming a high-energy thioester bond and then transfers the activated ubiquitin to E2, which subsequently transfers the ubiquitin to target substrate protein with the help of an E3 ligase. The E3 ubiquitin ligase interacts with both E2 and the target substrate and catalyzes the direct or indirect transfer of ubiquitin from the E2 to the ε-amino group of a lysine residue in the substrate protein by forming an isopeptide bond.[18-20] The human genome encodes 2 E1s, 30-50 E2s, and more than 600 different E3s.[21] Polyubiquitination of a substrate protein molecule can be achieved by multiple cycles of ubiquitin attachment to form a ubiquitin chain *de novo*, or transfer of a pre-assembled polyubiquitin chain

from E2.[22] Occasionally, a ubiquitin elongation factor E4 takes a part in the extension of the ubiquitin chain.[23]

The essential features of ubiquitin protein are accomplished by its seven lysine residues (K6, K11, K27, K29, K33, K48, and K63) and, in some cases, its N-terminal methionine (M1). Most ubiquitination chains are formed by conjugating the C-terminal glycine (Gly76) of a ubiquitin moiety via an isopeptide bond to an ε-NH_2 group of an internal lysine residue in the substrate or the preceding ubiquitin moiety, while in some cases, the C-terminal Gly76 of a ubiquitin moiety can also be fused linearly via a regular peptide bond to the M1 of the substrate or the preceding ubiquitin moiety.[24] Each of the residues can form different ubiquitin linkage types respectively, and the polyubiquitin chains with different linkages perform distinct cellular functions.[25] K48- and K63-linked polyubiquitination are the most well studied among the linkage types. Generally, a polyubiquitin chain formed by four or more ubiquitin moiety-linkage via K48 serves as a degradation signal for targeted protein degradation by the proteasome.[26] The K48-linked chain typically adopts a conformation with the hydrophobic residuals of ubiquitin molecules exposed at the interface, which is crucial for the recognition by the proteasome.[27,28] Monoubiquitination or polyubiquitin chains via K63-linkage, on the other hand, are mainly involved in non-proteolytic pathways such as DNA damage repair,[29] protein trafficking,[30] immune signaling,[31] ribosomal protein synthesis,[32] or autophagic degradation signaling.[33] More recently, K63-linked ubiquitin chains were shown to also direct substrate for proteasomal degradation by triggering K48/K63 branched ubiquitin chain.[34] M1-linked linear ubiquitin chains are also implicated in PQC. M1-linkage is catalyzed by the linear ubiquitin chain assembly complex (LUBAC) consisting of two E3 ligases, HOIP (HOIL-1L interacting protein) and HOIL-1, and an adaptor protein SHARPIN in mammals or by a recently described E3 ligase LUBEL (linear ubiquitin E3 ligase) in

Drosophila.[35] It was reported that LUBAC can be recruited to cytosolic protein aggregates, for example Huntingtin, to form the M1-linked polyubiquitin chain, which shielded the misfolded Huntingtin species from unfavorable interactions with low complexity domain-containing transcription factors that cause transcriptional dysregulation in Huntingtin's disease, and facilitates proteasomal degradation of misfolded Huntingtin species.[36]

The substrate specificity of the ubiquitination cascade is determined by E3 ligases. E3 ligases are generally categorized into four classes: the RING (Really Interesting New Genes) finger E3 ligases, U-box E3 ligases, the HECT (Homologous to the E6AP Carboxyl Terminus) domain E3 ligases, and RBR (RING-between-RING) E3s.[20] Although they all carry out the final step of ubiquitylation, they differ in composition and catalytic mechanism. The RING finger E3s and topologically similar U-box E3s act as the scaffold that mediates direct transfer of the ubiquitin from E2 to the target substrate by the interaction of E2 and the RING domain or U-box domain, respectively,[37,38] whereas HECT domain E3s mediate transfer of the ubiquitin from E2 to its active cysteine site to form an E3-ubiquitin intermediate before the final conjugation to the target substrate.[39] The RBR E3s are proved as RING-HECT hybrid E3 family and specialized by a conserved catalytic region which contains a RING1, a central in-between-RINGs, and a RING2 domain. RBR E3s mediate the ubiquitination by two-step reactions, in which the ubiquitin is transferred to the active cysteine site on RING2 and subsequently to the substrate.[40] Emerging evidence shows that E3 ligases play a critical role in modulating protein homeostasis (or proteostasis) owing to their efficient regulation and substrate specificity. Over the past decades, a number of studies focusing on cardiac E3 ligases have unveiled their significant involvement in (patho)physiology of cardiac diseases.[41-43] For example, ITCH was shown to attenuate pressure overload-induced cardiac hypertrophy by targeting principal protein Dvl for UPS degradation and

thereby inhibiting Wnt/β-catenin signaling;[44] it also can ameliorate oxidative species-induced cardiotoxicity in myocardial infarction and doxorubicin-induced cardiomyopathy by targeting thioredoxin-interacting protein for degradation.[45] WW domain-containing E3 ubiquitin protein ligase 2 (WWP2) showed protective effect in isoproterenol-induced cardiac hypertrophy by mediating poly(ADP-ribose) polymerase-1 (PARP1) degradation.[46] The Smad (suppressor of mothers against decapentaplegic) ubiquitination regulatory factor 1 (Smurf1) and factor 2 (Smurf2) were both shown to block cardiac fibrosis by binding to transforming growth factor (TGF)-β receptors via Smad7 and mediating TGF-β receptor degradation.[47,48]

Ubiquitination is reversible. The counter-process of ubiquitination is deubiquitination, in which deubiquitination enzymes (or deubiquitinase, DUBs) remove ubiquitin from ubiquitinated proteins. The DUBs can be classified into seven categories: ubiquitin-specific proteases (USPs/UBPs), ubiquitin C-terminal hydrolases (UCHs), ovarian tumor proteases (OTUs), Machado-Joseph disease proteases (MJDs), JAB/MPN/MOV34 metalloenzymes (JAMMs), motif interacting with ubiquitin-containing novel DUB family (MINDYs), and zinc finder with UFM1-specific peptidase domain proteins (ZUFSPs).[49] JAMM family belongs to zinc metalloproteinases, while the rest are classified as cysteine proteases. DUBs break down the (iso)peptide bonds between the ubiquitin and the conjugated substrate or between cojoined ubiquitin molecules to release ubiquitins. Some DUBs act to specific chain linkage types, such as K48- or K63-linked polyubiquitin chains, while some display less specificity that are capable of cleaving multiple chain types and ubiquitin-like modifiers.[50] Upon the recognition and binding to a polyubiquitinated substrate, the proteasome rapidly disassembles and removes the polyubiquitin chain via proteasome-associated DUBs (RPN11, USP14 and UCHL5) to facilitate the subsequent substrate unfolding and proteolysis.[51] Therefore, the balance between the opposing actions of ubiquitin E3

ligases and DUBs will ultimately determine the ubiquitination status of the proteasome substrate, enabling ubiquitination as a rate-limiting step in UPS-mediated protein degradation.

1.2. The 26S proteasome

The 26S proteasome is a ~2.5MDa multi-subunit protease complex that is localized in the cytosol, free or attached to the endoplasmic reticulum (ER), and in the nucleus of all eukaryotic cells, and confers the final step of UPS-mediated protein degradation.[52] A functional 26S proteasome is typically composed of a catalytic 20S core subcomplex which is coupled to one (26S) or two (30S) 19S regulatory particles at its end(s). Both 26S and 30S proteasomes are generally referred to as the 26S proteasome. Besides the 19S proteasome, the 20S proteasome can sometimes be capped by 11S proteasome(s), also known as Proteasome Activator 28 (PA28), to form an 11S-20S-11S complex or a 19S-20S-11S hybrid complex.[53] The 11S proteasome is assembled by PA28α and PA28β in the form of heteroheptamer (α3β4 or α3β4) or by PA28γ in the form of homoheptamer (γ7).[54,55] Both 19S and 11S proteasomes are capable of enhancing 20S proteolytic activity. Generally, the recognition and binding of ubiquitinated substrates triggers the conformational changes of the 26S proteasome, which drives subsequent substrate unfolding, deubiquitination, and translocation of the substrate into the 20S core particle for proteolysis.[56]

1.2.1. The 20S proteasome

The 20S proteasome is a cylindrical particle consisting of four stacked heteroheptameric rings, two outer and two inner, and harbors the proteolytically active sites in the interior surface of the barrel. Each of the two outer rings is composed of seven homologous but different α subunits (α1

through α7), forming a narrow channel for substrate entry. Each of the two inner rings is composed of seven highly conserved β subunits (β1 through β7) and contains the protease activity. Only three of seven β subunits, β1, β2, and β5, harbor protease catalytic sites, and confer the ability to cleave peptide bonds at the C-terminal side of acidic (caspase-like activity), basic (trypsin-like activity), and hydrophobic (chymotrypsin-like activity) amino acid residues respectively. All the active peptidase sites face the interior of the 20S cavity. The N-termini of the α subunits form a physical barrier or gate to preclude substrate access to the proteolytically active chamber. Gate opening is normally triggered by the docking of C-termini of ATPases of the regulatory particle.[57] Alternatively in lymphocytes and monocytes or in cells exposed to proinflammatory cytokines, such as tumor necrosis factor (TNF)-α or interferons (IFN)-α/β/γ, the constitutive proteolytically active subunits, β1, β2, and β5, are replaced by their inducible or immuno- counterparts, β1i/LMP2, β2i/MECL-1, and β5i/LMP7, during the *de novo* formation of the 20S proteasome.[58,59] The resultant proteasome isoform is so called "immunoproteasome" to emphasize its specialized 20S particle with altered proteolytic properties for more efficient antigen processing and presentation to the immune system.[60] The expression of inducible subunits (β1i, β2i, and β5i) was also detected in parallel with their constitutive counterparts in the normal adult heart.[61]

1.2.2. The 19S proteasome

The 19S proteasome is composed of six homologous AAA-ATPases (Regulatory Particle Triple A-ATPase; RPT1 through RPT6) and thirteen non-ATPases (Regulatory Particle Non-ATPase; RPNs) subunits, forming two sub-complexes: the base and the lid. A hexameric complex of the six RPTs together with scaffolding subunits (RPN1, RPN2, and RPN13) form the base,

whereas the rest of RPN subunits (RPN3, RPN5–RPN9, RPN11, RPN12, and RPN15/SEM1) form the lid with RPN10 mainly bound to the lid subunits.[62] RPN1, RPN10 and RPN13 contain domains that can bind to the ubiquitin or ubiquitin receptor, enabling them to recognize and anchor the substrate. Once bound, the polyubiquitin chain conjugated to the substrate is rapidly removed by the proteasome intrinsic DUB (RPN11) and/or proteasome-associated DUBs (USP14 and UCHL5). The RPTs dock on top of the 20S particle to open the α gate,[63] and unfold the substrate and translocate it into the catalytic core through the gate in an ATP-dependent manner.[64] Cryo-electron microscopy reconstructions reveal that RPN3, RPN5, RPN6, RPN7, RPN9, and RPN12 contain PCI-domain, which can form a horseshoe shape with radiating protrusions. PCI domains interact with each other by lateral interactions to stabilize the lid and can also interact with RPT ring and 20S subunits to serve as a scaffold of the proteaome.[65,66] Of these PCI domain-containing subunits, RPN6 has been shown to interact with both RPT6 and α2, which may enable its possible involvement in the stabilization of 20S-19S coupling as well as opening of the 20S gate.[67]

2. PQC in cardiac proteotoxicity and proteinopathy

Intracellular proteostasis is crucial to maintaining optimal cellular function.[68] Proteotoxicity refers to all toxic effects exerted by misfolded proteins or their derivatives such as aberrant protein aggregation. Proteinopathy is disease caused by misfolded proteins. Generally in most organ systems, proteostasis requires a sum balance of protein synthesis, post-translational processing, trafficking, folding, assembly/disassembly and degradation.[69,70] Perturbations to any of these processes by internal or external stimuli must be adeptly controlled by either tight regulation of that specific process or compensatory responses; otherwise, alterations to proteostasis will lead the cell to pathological consequences, ultimately cell death at cellular level.[71] Hence, the pathogenic

impact of impaired proteostasis is maximally manifested in organs with poor, if any, capacity of regeneration, such as the brain and the heart. In the heart particularly, cardiomyocytes are subjected to more challenges than most other cells to maintain proteostasis.[72] First, cardiomyocytes have highly specialized proteins that participate in electrical conduction and contraction. This requires specialized PQC surveillance by, for example, small heat shock proteins (HSPs) that favorably bind to sarcomere-associated proteins to preserve normal cellular function.[73] Second, the massive metabolic demand for cardiomyocyte contraction is fulfilled by oxidative phosphorylation in the mitochondria, which consequently produces abundant proteotoxic reactive oxygen species (ROS) even under healthy condition.[74] Third, cardiomyocytes are generally terminally differentiated and lack the ability to reduce protein aggregates and damaged intracellular proteins through cell division.[75] As a consequence, a sophistical PQC system is required for cardiomyocytes to sense and minimize proteotoxicity.

The (patho)physiological significance of cardiac PQC is best illustrated in cardiac proteinopathies that are caused by increased expression of misfolded proteins and characterized by the accumulation of aberrant protein aggregates in cardiomyocytes. Emerging evidence has suggested that increased proteotoxic stress (IPTS) in cardiomyocytes also can occur in the common forms of cardiomyopathies, including hypertrophic cardiomyopathy, ischemic cardiomyopathy, and diabetic cardiomyopathy, situating them into the cardiac proteinopathy family. Both excess production of misfolded proteins and impaired PQC resulted from genetic mutations, environmental stimuli, and/or aging can cause IPTS, which is a major pathogenic factor in the progression from a large subset of cardiac disease, including proteinopathies, to heart failure.[76] The production of misfolded proteins can be markedly increased in cardiomyocytes under various pathological conditions, both inherited and acquired. The abundant accumulation of misfolded

proteins and protein aggregates during cardiac IPTS further cause PQC impairment, mitochondrial dysfunction and increased cell death, which have been evident in a transgenic (tg) mouse model of cardiac proteinopathy.[5,77]

The central mechanical function of cardiomyocytes is performed by the contractile apparatus where PQC plays a vital role to maintain normal protein turn over and prevent cardiac proteinopathy in response to mechanical stress. For example, variants that truncate titin proteins (TTNtv), the most common genetic cause of dilated cardiomyopathy, lead to cytoplasmic aggregation of the truncated titin and thereby UPS impairment;[78-80] mutations in a sarcomere-associated HSP co-chaperone, Bcl2-associated athanogene 3 (BAG3), were found to be associated with dilated cardiomyopathies as well as impaired protein turnover;[81,82] multiple E3 ligases, such as muscle RING fingers (MuRFs)-1/2/3, TRIM32 and CHIP (carboxyl-terminus of HSP70-interacting protein, are localized at the sarcomere to facilitate UPS-mediated degradation of sarcomere-associated proteins in a timely manner to avoid aberrant protein aggregation.[83]

3. Proteasome functional insufficiency (PFI) in cardiomyopathies

When chaperone-mediated repair and the UPS are overwhelmed, misfolded proteins escape from the proteasomal degradation and sequentially form soluble oligomers and insoluble aggregates in the cell.[84] The shared conformation of misfolded protein oligomers enables them to bind the proteasome with low nanomolar affinity and prevent substrate entry into the 20S proteasome for degradation through allosteric stabilization of the closed α gate, thereby impairing ubiquitin-dependent and -independent proteasome function.[85] Hence, both proteasome impairment and misfolded protein overload can lead to proteasome functional insufficiency (PFI), which denotes that proteasomes functionally fail to fulfill the demand for a timely degradation of the

proteins designated for proteasomal degradation.[76] There is growing evidence identifying PFI as a major pathogenic factor for cardiomyopathies and heart failure, which is summarized in this section.

3.1. PFI in human heart disease

Despite that no serum biomarkers or any other noninvasive assessments are currently available for the evaluation of myocardial proteasome function in living humans, scientists have attempted to measure the proteasome peptidase activities as well as the abundance of the proteasome subunits in the myocardial biopsy specimens from human hearts.[86] PFI in human cardiac proteinopathies was best demonstrated by Day's team, who detected markedly lower ATP-dependent myocardial 26S proteasome chymotrypsin-like and caspase-like activities in human heart failure and hypertrophic cardiomyopathy than that in non-failing control hearts, with no changes in the abundance of proteasome subunits observed.[87] The left ventricular (LV) assist device (LVAD) is clinically used as a bridge for cardiac transplantation for patients who have reached end-stage heart failure and has been demonstrated to partially recover LV function due to mechanical unloading. The 26S proteasome chymotrypsin-like activity was significantly increased after 31 weeks of LVAD treatment, indicating proteasome functional upregulation associated with LV functional recovery due to mechanical unloading.[87] Similarly, the myocardial 20S proteasome chymotrypsin-like activity in the LV tissue from patients with idiopathic dilated cardiomyopathy was also discernibly elevated after 214 days of LVAD treatment.[88] In congestive heart failure, the abundance of sarcoplasmic 20S proteasome subunits was significantly decreased compared with that in control hearts, but was markedly increased after unloading. This depressed proteasome abundance was shown to be reversely correlated with cardiomyocyte hypertrophy, DNA content

and cell cycle regulatory proteins, suggesting the involvement of proteasome insufficiency in the pathogenesis of cardiac hypertrophy and heart failure.[89] The 26S proteasome dysfunction in human end-stage heart failure was reported to be associated with the impairment of 26S proteasome assembly as a result of diminished 19S docking onto the 20S proteasome, as these failing hearts exhibited decreased 30S proteasomes, RPT ATPase activity and α subunit phosphorylation.[90] These results provide compelling evidence directly indicating proteasome impairment in multiple forms of human heart disease.

PFI is normally accompanied by increased production of misfolded proteins and accumulation of aberrant protein aggregates, which further impairs UPS proteolytic function resulting in elevated levels of ubiquitin conjugates.[77] Hence, other studies evaluated the 26S proteasome functioning in human cardiac disease indirectly by assessing the accumulation of disease-associated misfolded protein aggregates and ubiquitin conjugates in the hearts. Experimental and clinical evidence has indicated that soluble pre-amyloid oligomers, rather than the mature amyloid fibril aggregates, contribute to the proteotoxicity in proteinopathies.[91] The cytoskeletal protein desmin was shown to be differentially modified by phosphorylation and proteolytic cleavage to form amyloid-like oligomers in human heart failure.[92,93] Proteotoxic pre-amyloid oligomers were abundantly presented in the heart of patients suffering from hypertrophic cardiomyopathy and dilated cardiomyopathy with complicating episodes of arrhythmia, pneumonia and congestive heart failure.[94] Emerging evidence suggests that pre-amyloid oligomer deposits are also associated with atrial fibrillation and potentially contribute to the pathogenesis.[95-98] Furthermore, a number of studies have revealed elevated myocardial accumulation of ubiquitinated proteins and ubiquitin-positive aggregates in dilated or ischemic cardiomyopathies.[99-102]

Hence, these findings arguably place a large subset of human cardiomyopathy and heart failure into the proteinopathy category and strongly indicate PFI as the common feature in these disorders. The cardiotoxicity observed in multiple myeloma patients who were treated with three proteasome inhibitors, bortezomib, izazomib or carfilzomib, highlights the detrimental effect of PFI in human hearts.[103]

3.2. PFI is a major pathogenic factor in animal models of cardiomyopathy

The myocardial PFI implicated in human cardiomyopathies and heart failure has been recapitulated in animal models of multiple forms of cardiomyopathies and further investigations have been pursued to identify the pathogenic role of PFI in the disease development.

Desmin-related cardiomyopathy (DRC), which can present as restrictive, hypertrophic or dilated cardiomyopathies during the disease progression, is caused by mutations in either desmin or other essential proteins for desmin filament formation,[104,105] such as a 7-amino-acid (R173 through E179) deletion of the desmin gene (D7-des)[106] and a R120G-missense mutation of the αB-crystallin gene ($CryAB^{R120G}$).[107] The presence of aberrant desmin-positive protein aggregates inside cardiomyocytes is the pathological hallmark of DRC. Human DRC can be recapitulated by tg mouse models with overexpression of D7-des or $CryAB^{R120G}$ in mouse hearts, which mimic the increased production of misfolded proteins in cardiomyocytes. The accumulation of intrasarcoplasmic desmin-positive protein aggregates and marked increase in polyubiquitinated proteins were detected in the myocardium of both tg mice, but not mice with tg overexpression of wild-type (WT) desmin or CryAB, suggesting that PFI is present in DRC. When coupled with a UPS reporter mouse model that overexpresses a surrogate UPS substrate, these tg mice exhibited severe inadequacy in cardiac UPS performance as evident by the accumulation of the reporter

protein. Along with the observations of increased ubiquitinated proteins, the UPS impairment in both tg mice was likely resulted from PFI.[106,107] These results for the first time demonstrate that aberrant protein aggregation resulted from increased misfolded protein production suffices to cause PFI and thereby overall UPS insufficiency in animals with cardiomyopathies. Further analysis on CryAB^{R120G}-based DRC revealed that PFI can be attributable to deficiency in the substrate delivery into 20S proteasome.[77] Cardiac PFI was subsequently demonstrated in mouse models with other forms of cardiomyopathies, such as ischemia/reperfusion (I/R) injury,[108,109] dilated cardiomyopathy created by a mutant nuclear envelope protein,[110] streptozotocin-induced Type I diabetes,[111] and hypertrophic cardiomyopathy induced by a truncated cardiac myosin-binding protein (cMyBP-C) or knocking out cMyBP-C.[112]

With the creation of a mouse model of cardiomyocyte-restricted proteasome functional enhancement, PFI was first established as a major pathogenic factor in cardiac proteinopathy and myocardial I/R injury.[108] Overexpression of PA28α increased 11S-coupled 20S proteasomes by stabilizing PA28β and thereby improved the proteasome activity and overall UPS proteolytic function, which led to significant reduction of aberrant protein aggregates when coupled with tg overexpression of CryAB^{R120G} in mice. Functionally, PA28α overexpression attenuated cardiac hypertrophy and delayed premature death of mice with CryAB^{R120G}-based DRC. Similarly, enhancement of proteasome function by PA28α overexpression reduced the infarct size and rescued cardiac function after I/R injury. On the contrary, a tg mouse model with cardiomyocyte-restricted overexpression of a peptidase-disabled β5 displayed exacerbated infarct size, cardiomyocyte apoptosis and cardiac dysfunction due to I/R injury, supporting the pathogenic role of PFI.[109] Furthermore, chronic proteasome inhibition was shown in pigs to cause cardiac structural and functional alterations in common with a hypertrophic-restrictive cardiomyopathy phenotype,

indicating that PFI is sufficient to induce cardiac dysfunction.[113] Hence, improvement of proteasome function has the potential to become a new therapeutic strategy for the treatment of heart diseases with IPTS. However, this is hindered by the lack of effective pharmacological methods.

4. Phosphoregulation of the 26S proteasome

It was widely assumed that the rate of UPS-mediated protein degradation is solely determined by the rate of ubiquitination. However, emerging evidence suggests that the functionality of 26S proteasomes is vigorously regulated and dictates the degradation efficiency of ubiquitinated proteins, especially misfolded proteins.[76,114,115] Therefore, a better understanding of the regulation of proteasome functioning should facilitate the search for ways to improve proteasome proteolytic function and accelerate the breakdown of unwanted and toxic proteins in the cell, a conceivable strategy to prevent or more effectively treat disease with IPTS.[76]

Phosphorylation has emerged as an important post-translational mechanism for the regulation of 26S proteasomes in health and disease. Over 455 phosphosites on the human 26S proteasome from primarily preparations processed *in vitro* were detected by the large-scale phosphoproteomics, including ~200 phospho-serine sites, ~100 phospho-threonine sites, and ~150 phospho-tyrosine sites;[116] however, the physiological relevance of only a few of them has been studied to some extent. There is growing evidence that several protein kinases are able to phosphorylate the proteasome, but only few of them have been studied for their targeted proteasome subunits and residues and for the effects on proteasomal protein degradation rate or disease progression.[117,118]

4.1. The cAMP-dependent kinase (PKA)

Among these kinases, PKA is the first and arguably the best studied. PKA has been long known to phosphorylate proteasome subunits and contribute to proteasome phosphoregulation.[119,120] Active PKA treatment or protein phosphatase 2A (PP2A) inhibition was shown to enhance the peptidase activities of 20S proteasomes purified from murine hearts *in vitro* and proteomic analyses of purified cardiac 20S proteasomes revealed multiple potential PKA-targeting phosphosites at 20S proteasomes.[121,122] However, the physiological relevance of those 20S proteasome phosphosites has not been investigated either in cultured cells or in the heart.

It was once reported that, instead of 20S subunits, phosphorylation of a 19S subunit RPT6 at Ser120 mediated the activation of proteasomes by PKA, but this was refuted by a more recent and more convincing study.[123,124] The latter showed that Ser14-Rpn6 was selectively phosphorylated by cAMP/PKA and this phosphorylation was solely responsible for cAMP/PKA-mediated 26S proteasome activation in cultured non-cardiac cells.[123] The biochemical importance of Ser14-RPN6 was tested using site-directed mutagenesis to generate phospho-dead and phosphomimetic Rpn6 mutants by replacing Ser14 by Ala (S14A) and Asp (S14D) respectively to block or mimic Ser14-Rpn6 phosphorylation (pS14-Rpn6 hereafter).[123] In HEK293 cells and purified proteasomes, S14A mutation repressed the 26S proteasome peptidase activities, while overexpression of S14D mutant stimulated the proteasomal degradation of aggregation-prone proteins.[123] In addition to the comprehensive cell culture study that discovered pS14-Rpn6 as the specific target of PKA to activate 26S proteasomes, follow-up studies further demonstrate that activating cAMP/PKA signaling by hormones, intense exercise or fasting phosphorylates Ser14-Rpn6 and enhances proteasome activity in hepatocytes, working hearts and skeletal muscles;[125] and pharmacological augmentation of cAMP prevents tau-driven proteasome impairment and cognitive dysfunction.[126]

Moreover, increasing cAMP also seemed to promote the assembly of 30S proteasome, which possibly contributes to the proteasome enhancement by PKA as well,[123,127] but the underlying mechanism remains uncertain. Notably, cAMP augmentation facilitated the proteasomal removal of short-lived proteins that are ubiquitinated, but not long-lived cellular proteins, and thereby reduced total ubiquitin conjugates in the cell.[123] The short-lived proteins targeted by cAMP/PKA-mediated proteasome activation include regulatory proteins, such as transcription factors SP1, Nrf2, and c-Myc, and aggregation-prone mutant proteins, such as neurodegeneration-associated mutant Tau, FUS, and TDP43.[123,124,126] These discoveries have shown obvious clinical relevance and suggested new promising approaches to upregulate the 26S proteasomes and halt proteinopathies.

Such effects of PKA were supported by a recent study of our lab, which demonstrated that cAMP augmentation by an adenylate cyclase activator increased pS14-Rpn6 in a PKA-dependent manner and improved UPS proteolytic function in cultured cardiomyocytes; increasing cAMP by a selective inhibitor of phosphodiesterase (PDE) type 4 elevated 26S proteasome chymotrypsin-like activity along with increased pS14-Rpn6, in mice with $CryAB^{R120G}$-based DRC.[128] However, there have been no reports confirming that proteasomes are activated by PKA via pS14-Rpn6 in intact animals; moreover, the role of pS14-RPN6 in cardiac health and disease remains to be established.

4.2. Protein kinase G (PKG)

There is compelling evidence showing that the cGMP-dependent protein kinase or PKG is also involved in the regulation of protein turnover in the cell and capable of modulating pathogenesis of the diseases with proteotoxicity. Research on cGMP/PKG has focused on its role in peripheral smooth muscle, including blood vessel relaxation and intestinal secretion, which has significant

medical implications.[129-131] For instance, a soluble guanylate cyclase (sGC) stimulator (riociguat) that triggers cGMP synthesis and three inhibitors of PDE5 (sildenafil, tadalafil and vardenafil) that hydrolyze cGMP, are FDA-approved drugs to treat pulmonary hypertension and/or erectile dysfunction; another sGC stimulator (vericiguat) and a neprilysin inhibitor (sacubitril+valsartan) are approved for treating heart failure with reduced ejection fraction (HFrEF) and/or heart failure with preserved ejection fraction (HFpEF).[131]

Our lab has previously discovered that PKG positively regulates the proteasome. Overexpression of constitutively active PKG1α or cGMP augmentation by sildenafil increased proteasome peptidase activities, promoted the degradation of disease-associated proteins in cardiomyocytes, and protected the cardiomyocytes against proteotoxic stress, whereas genetic or pharmacological inhibition of PKG elicited the opposite responses. Moreover, sildenafil enhanced myocardial proteasome-mediated misfolded protein degradation and reduced aberrant protein aggregates in mice with $CryAB^{R120G}$-based cardiac proteinopathy, and eventually attenuated cardiac malfunction.[132] cGMP/PKG in the heart can be triggered by the neurotransmitter acetylcholine via cardiac muscarinic 2 (M2) receptors.[133,134] Stimulation of M2 receptors was shown to increase proteasome peptidase activities and enhance proteasome-dependent proteolysis, which was abolished by the inhibition of PKG, suggesting that PKG may mediate M2-dependent proteasome activation.[135] The effects of cGMP/PKG were substantiated by subsequent studies. Human neuroblastoma cells (SH-SY5Y) and other cell lines treated with a PDE5 inhibitor or an sGC stimulator exhibited rapidly increased proteasome peptidase activities, which can be abolished by PKG inhibitors. Recombinant PKG stimulated the activation of the affinity-purified 26S proteasome, while λ phosphatase reversed the effects by the recombinant PKG or the PDE5 inhibitor, indicating PKG enhances the 26S proteasome activity by direct phosphorylation of the

proteasome or a protein copurified with the proteasome. Unlike PKA, it appeared that PKG stimulated the degradation of both short-lived and long-lived proteins but exerted no effect on the proteasome assembly.[136] Using zebrafish larvae models of tauopathies and Huntington's disease, raising cGMP by sildenafil promoted the degradation of disease-associated mutant Tau and Huntingtin proteins and attenuated neuronal death and developmental abnormalities.[136] Similarly, cGMP augmentation increased 26S proteasome activities and facilitated the degradation of disease-associated mutant proteins in a mouse model of demyelinating neuropathy caused by the expression of mutant myelin protein zero (S63del). These mice exhibited increased myelin thickness, decreased amyelinated axons, and improved nerve conduction with the treatment of sildenafil.[137]

Unfortunately, the specific proteasome subunit(s) and residue(s) targeted by PKG are still unclear. M2 receptor stimulation did not alter the abundance of β5 and Rpt6 in the cardiomyocytes, but exerted an acidic shift of their isoelectric points, suggesting their phosphorylation.[135] However, It was later shown that PKG did not phosphorylate Rpn6, Rpt3 or Rpt6 at lease in certain cell types.[136] Despite different cell types, these results may suggest β5 as a potential substrate of cGMP/PKG to activate the 26S proteasome. Further identification and characterization of the phosphosite(s) that mediate PKG-dependent proteasome activation will surely guide the search for suitable pharmacological agents that increase cGMP to treat diverse proteotoxic diseases, including cardiomyopathies.

4.3. Dual specificity tyrosine-phosphorylation-regulated kinase 2 (DYRK2)

The 26S proteasome is a central regulator of the cell cycle by degrading the ubiquitinated cell cycle regulatory proteins, such as cyclins and cyclin-dependent kinase (CDK) inhibitors, and

thereby tightly controlling the timing during the cell cycle transition.[11] Impairment of key protein degradation by proteasome inhibition or excess protein aggregation impedes cell proliferation, which contributes to the pathogenesis of certain diseases.[138-140] While the importance of phosphorylation-dependent ubiquitination of the UPS substrates in the cell cycle has been appreciated for decades, the crucial role of the 26S proteasome is revealed in the past decade. Large scale mass spectrometry has identified multiple proteasome phosphosites that are phosphorylated during the cell cycle.[141-144] The first kinase that has been detailed is DYRK2, which dynamically phosphorylates the 19S subunit, RPT3, at Thr25.[145,146] Thr25-Rpt3 phosphorylation was found *in vivo* and in purified 26S proteasomes from multiple cell lines and enriched through S to G2/M phases, suggesting Thr25-Rpt3 phosphorylation is functionally implicated in cell proliferation. DYRK2 was identified as the primary kinase that phosphorylates Thr25-Rpt3 with a kinome-wide screen and was shown to increase the proteasome proteolytic activity in a Thr25-Rpt3 phosphorylation-dependent manner. Blockade of this phosphorylation by CRISPR/Cas9-edited phospho-dead T25A mutant in human breast cancer cells abolished the proteasome activation by DYRK2 and caused remarkable accumulation of the CDK1 inhibitors, $p21^{Cip1}$ and $p27^{Kip1}$, stabilization of which is associated with prolonged S to G2/M phases. These findings were, to a certain extent, supported by a large-scale genome study, in which DYRK2 and Rpt3 were placed in the same "essential gene set" in human breast cancers.[146,147]

It is noted that the role of DYRK2-mediated Thr25-Rpt3 phosphorylation in the proteasome regulation has only been demonstrated in actively proliferating cells. Cardiomyocytes leave the cell cycle shortly after birth and are thought to be terminally differentiated.[148] Therefore, it is important to pursue further investigation on DYRK2's impact on the proteasome and the contribution of Thr25-Rpt3 phosphorylation in differentiated mature cardiomyocytes. Emerging

evidence shows that mature cardiomyocytes are able to re-enter the cell cycle with a much lower proliferation rate after injuries, such as myocardial infarction.[149-153] Upregulation of cell cycle inhibitors, $p21^{Cip1}$ and $p27^{Kip1}$, may contribute to the decline in post-mitotic proliferation capacity of cardiomyocytes.[154] Since DYRK2-mediated Thr25-Rpt3 phosphorylation is likely to regulate the degradation of $p21^{Cip1}$ and $p27^{Kip1}$ by proteasomes during cell proliferation, exploring its role in cardiomyocyte regeneration could potentially reveal a new therapeutic target for cardiac repair after injury.

4.4. Calcium/calmodulin-dependent protein kinase II (CaMKII)

CaMKII mediates physiological functions and pathological processes in the heart.[155-157] CaMKII activation is prominently involved in various common cardiac diseases, including cardiac hypertrophy and remodeling,[158,159] myocardial ischemic injury,[160] arrhythmia,[161] and cardiomyopathies;[162-164] and CaMKII inhibition has been extensively examined to improve cardiac function in animal models.[165,166] The novel role of CaMKII in the proteasome regulation may open up alternative CaMKII-based therapeutic strategies for cardiac disease with proteotoxicity.

It was first reported that phosphorylation of proteasome RPT6 at Ser120 mediated 26S proteasome by PKA.[124] However, this is refuted by later studies demonstrating that CaMKII, but not PKA, regulates RPT6 phosphorylation, and CaMKIIα stimulated proteasome activation in neurons and HEK293T cells in a Ser120-Rpt6 phosphorylation-dependent manner.[167,168] When expressed in HEK293 cells, the phospho-dead Rpt6-S120A mutant blocked CaMKII-dependent degradation of a UPS substrate, while the phosphomimetic Rpt6-S120D mutant had no discernible effect, indicating that Ser120-RPT6 phosphorylation is required but not sufficient for CaMKII-mediated proteasome activation.[168] CaMKIIα's translocation, independent of its kinase activity,

was shown to recruit proteasomes to dendrite spines by direct association with S120-phosphorylated Rpt6 for activity-dependent degradation of polyubiquitinated proteins.[168-170] In mice subjected to fear conditioning, activation of CaMKII increased proteasome activity and Ser120-Rpt6 phosphorylation during memory formation.[171] Another *in vivo* study demonstrated that a T-type calcium channel enhancer SAK3 enhanced the proteasome activity, which was likely associated with autophosphorylation of CaMKII and Ser120-Rpt6 phosphorylation, and ameliorated motor and cognitive impairments in amyloid precursor protein knock-in mice.[172]

Although CaMKII-phosphorylated Ser120-Rpt6 was demonstrated to enhance proteasome peptidase activity, none of the existing studies have tested its effect on the rate of proteasomal degradation of certain disease-associated proteins. Moreover, the role of Ser120-Rpt6 phosphorylation in mediating CaMKII-dependent proteasome activation *in vivo* remains to establish. Thus, *in vivo* evaluations of the phosphorylated Ser120-Rpt6's responsibility in CaMKII-mediated proteasome activation and its role in the disease progression will likely provide new insights into the pathogenesis and therapeutic development of proteinopathies, including cardiomyopathies.

5. Potential therapeutic strategies to target cardiac PFI

There are currently no approved therapeutic strategies to rescue PFI and improve PQC. Although the (patho)physiological significance of the proteasome phosphoregulation in the heart remains to be established, growing evidence has suggested that proteasome activation by cAMP/PKA and cGMP/PKG have promising pharmacological potential to treat cardiac proteinopathy. Earlier an FDA-approved PDE5 inhibitor, sildenafil, was first reported to prevent myocardial aberrant protein aggregation and attenuate cardiac dysfunction in DRC.[132] Another

study showed that an exercise-responsive myokine, osteocrin, protected against streptozotocin-induced diabetic cardiomyopathy through restoring PKG-dependent proteasome activation and had synergistic cardioprotection with sildenafil, further supporting that PKG signaling can be a therapeutic target for cardiomyopathy.[173] While several studies indicated the beneficial effects of cAMP/PKA-mediated proteasome activation in neurodegenerative disorders,[126,174,175] it remains undefined whether it alone benefits the treatment of heart disease with PFI. More recently, a selective PDE1 inhibitor IC86430, which activates both PKA and PKG, was demonstrated to improve myocardial 26S proteasome peptidase activity and promote proteasome-mediated degradation of misfolded proteins, in a PKA- and PKG-dependent fashion, in the heart of DRC. Mice treated with IC86430 displayed attenuated HFpEF-like phenotype and ultimately delayed pre-mature death; particularly, a PDE4 inhibitor, piclamilast, phosphorylated myocardial pS14-Rpn6 and increased the 26S proteasome peptidase activities.[128] Hence, the beneficial outcome of PDE1 inhibition may be, at least in part, mediated by PKA-phosphorylated Ser14-Rpn6.

6. Hypothesis and specific aims

Developing pharmacological strategies to attenuate PFI requires a better understanding of the mechanisms that regulate proteasome activity. A comprehensive study using exclusively cultured cells demonstrated that the activation of the 26S proteasome by cAMP/PKA is exclusively mediated by pS14-RPN6,[123] but this remains to be established *in vivo* or in animals. PKA-mediated proteasome activation was also demonstrated to facilitate the removal of disease-associated aggregation-prone proteins in cultured cells, implying the critical clinical relevance of this mechanism.[123] Epinephrine, which raises cAMP levels, was shown to increase proteasome peptidase activity and cardiac power output in perfused working rat hearts; 26S proteasomes purified from these hearts displayed increased pS14-Rpn6, suggesting that PKA-mediated proteasome activation in the heart can affect cardiac functioning, which may be mediated by pS14-Rpn6.[125] Thus, we speculated that pS14-Rpn6 mediates myocardial proteasome activation by PKA. Indeed, our lab has recently demonstrated that cAMP augmentation increased pS14-Rpn6 in a PKA-dependent manner and improved UPS proteolytic function in cultured cardiomyocytes, and elevated myocardial 26S proteasome peptidase activity along with increased pS14-Rpn6 in mice with $CryAB^{R120G}$-based cardiac proteinopathy; more importantly, the increased myocardial proteasome activity and pS14-Rpn6 were likely involved in the cardiac therapeutic benefits by PDE1 treatment.[128] However, there is no direct evidence that establishes the mediating role of pS14-Rpn6 in proteasome activation in animals or defines the role of this mechanism in cardiac response to IPTS. Hence, we conducted the present study to test the **central hypothesis** that pS14-RPN6 mediates the activation of proteasomes by PKA and reduces proteotoxicity in animals, by pursuit of the following two specific aims:

Specific aim 1: Establish the role of pS14-Rpn6 in PKA-induced proteasome activation *in vivo*. This is to test the hypothesis that Ser14-Rpn6 mediates the activation of 26S proteasomes by PKA in mice.

Specific aim 2: Determine the role of pS14-Rpn6 in cardiac response to IPTS. This is to test the hypothesis that pS14-Rpn6 activates the 26S proteasomes and thereby protects against cardiac proteotoxicity.

7. Novelty and significance

Clinical and experimental studies have revealed the occurrence of PFI and cardiac IPTS during the progression from a large subset of heart diseases, including cardiac proteinopathy, to heart failure.[84] Therefore, improvement of proteasome function has the potential to become a new therapeutic strategy for the treatment of heart diseases with IPTS.[76] However, this is hindered by the lack of effective pharmacological methods. A better understanding of the regulation of proteasome functioning should facilitate the search for ways to accelerate the breakdown of unwanted and toxic proteins in the cell, a conceivable strategy to prevent or more effectively treat disease with IPTS. The (patho)physiological significance of PKA was extensively studied but its role in proteostasis remains obscure. A cell culture study reveals that pS14-RPN6 mediates PKA-induced activation of 26S proteasomes. Consistently in various cell types and isolated organs, pS14-RPN6 and proteasome activities were shown to be significantly increased when cAMP is augmented by pharmacological agent, hormones, or physical activity.[125] Despite compelling *in vitro* evidence, only few *in vivo* studies have explored the *in vivo* relevance of proteasome phosphoregulation, but the evidence reported so far are all associative in nature.[125,126,128] None of the identified proteasome phosphosites, including pS14-RPN6, have been tested genetically for their physiological requirement and (patho)physiological significance in animals. Here we have conducted the present study to determine the role of pS14-RPN6 in the activation of 26S proteasomes by PKA in mice and to determine the physiological significance of this phosphorylation in disease progression of the $CryAB^{R120G}$-based proteinopathy mice. By creating knock-in mice and cells to block or mimic pS14-Rpn6, our results provide unequivocal evidence for the first time in animals that pS14-RPN6 is responsible for the activation of 26S proteasomes by PKA. We have also demonstrated that proteasome assembly was increased in $CryAB^{R120G}$-

induced proteinopathy. Although it mediates PKA-induced proteasome activation, pS14-Rpn6 does not appear to enhance the proteasome assembly. Moreover, we have discovered that myocardial pS14-Rpn6 is selectively decreased during disease progression of the CryAB^{R120G}-induced proteinopathy; and we demonstrate that this decrease plays a key pathogenic role in the cardiac proteinopathy, thereby identifies elevating pS14-RPN6 as a potential strategy to treat heart disease with IPTS.

MATERIALS AND METHODS

Mouse models

The protocols for animal care and use in this study have been approved by University of South Dakota Institutional Animal Use and Care Committee (IACUC). The animals were given *ad lib* access to food and water and housed in specific pathogen free control rooms with optimal temperature (22-24 °C) and 12-hour light/12-hour dark cycle.

$Rpn6^{S14A}$ and $Rpn6^{S14D}$ mice

The $Rpn6^{S14A}$ (S14A) and $Rpn6^{S14D}$ (S14D) knock-in mice were newly created in the C57BL/6J inbred background via a contract to Shanghai Biomodel Organism Science & Technology Development Co., Ltd. (Shanghai, China), using the CRISPR/Cas9 technology to target the point mutation to the endogenous *Psmd11/Rpn6* gene (MGI:1916327) which is located in chromosome 11.

The genomic DNA sequence immediately surrounding the point mutation (p.S14A, c.40T>G) for S14A is as follow:

CGTCGGCGGCCGCGGCCGGGGACGGTGTGAGAGCGGTAAGATGGCGGCCGCAGCG

GTGGTGGAGTTCCAGAGAGCCC*AG**T**CTCTACTCAGCACCGAC*CGGGAGGCCTCCATC

GACATCCTCCACTCCATCG, in which the italic region is gRNA position, the bold base (T) is the to-be-mutated base for creation of the mutant protein $Rpn6^{S14A}$, and the underlined is the protospacer adjacent motif (PAM). The oligo donor DNA sequence for S14A is as follows:

GCGGCCGGGGACGGTGTGAGAGCGGTAAGATGGCGGCCGCAGCGGTGGTGGAGTTC

CAGAGAGCCCAG**G**CTCTACTCAGCACCGACCGGGAGGCCTCCATCGACATCCTCCA

CTCCATCG.

The genomic DNA sequence immediately surrounding the point mutation [e(S14D)1] for S14D is as follow:

CGTCGGCGGCCGCGGCCGGGGACGGTGTGAGAGCGGTAAGATGGCGGCCGCAGCG

GTGGTGGAGTTCCAGAGAGCCC*AG**TC**TCTACTCAGCACCGAC*CGGGAGGCCTCCATC

GACATCCTCCACTCCATCG, in which the italic region is gRNA position, the bold bases (TC) is the to-be-mutated bases for creation of the mutant protein $Rpn6^{S14D}$, and the underlined is the PAM. The oligo donor DNA sequence for S14D is as follows:

GCGGCCGGGGACGGTGTGAGAGCGGTAAGATGGCGGCCGCAGCGGTGGTGGAGTTC

CAGAGAGCCCAG**GA**TCTACTCAGCACCGACCGGGAGGCCTCCATCGACATCCTCCA

CTCCATCG.

Through microinjections of Cas9 mRNA, gRNA, and donor DNA into fertilized eggs of C57BL/6J mice, multiple F0 mice positive for the mutations were generated. The mutation positive F0's were bred with C57BL/6J mice to generate 5 positive F1 mice which were further back-crossed into C57BL/6J mice and yielded the F2 generation heterozygotes. Homozygotes were then obtained from breeding between the heterozygotes. The F2 generation of heterozygous and homozygous S14A and S14D mice were shipped from Shanghai, China to Vermillion, SD. The genotype of each of them were confirmed by DNA sequencing analysis of the PCR products that cover the segment of genome containing the target point mutation.

S14A and S14D mice used in the present study were from breeders that had been subjected to at least 6 generations of back-cross into the C57BL/6J inbred background to eliminate any potential off-target mutations resulting from the CRISPR/Cas9 procedures.

GFPdgn tg mice

The creation and characterization of a tg mouse model expressing GFPdgn were reported before.[176] GFPdgn is a slightly shorter version of GFP^{u}, which is an enhanced green fluorescence protein (GFP) modified by carboxyl fusion of degron CL1. Degron CL1 is a 16-amino-acid sequence (ACKNWFSSLSHFVIHL) that is consensus among multiple short-living proteins of fission yeast and has proven to be a ubiquitination signal sequence. It seems to share a signature structure with misfolded proteins and signals for ubiquitination likely through surface exposure of a stretch of hydrophobic residuals.[177,178] GFP^{u} and GFPdgn are both proven substrates for the UPS.[176] GFPdgn tg mice in the C57BL/6J inbred background were used. S14D mice were cross-bred with the GFPdgn tg mice respectively to generate heterozygous and homozygous S14D-coupled hemizygous GFPdgn tg (S14D/+::GFPdgn, S14D/S14D::GFPdgn) mice, with their littermates of hemizygous GFPdgn tg mice serving as the control for assessing the effect of S14D on UPS performance.

CryAB^{R120G} tg mice

The line 134 tg mouse model expressing the CryAB^{R120G} specifically in cardiomyocytes was described previously.[107] The CryAB^{R120G} tg mouse is a well-established animal model of cardiac proteinopathy that has been widely for studying cardiac proteotoxicity. R120G mutation is a missense mutation in the *CryAB* gene. *CryAB^{R120G}* has been linked to desmin-related myopathy in humans. Desmin-related myopathy is characterized by intrasarcoplasmic accumulation of desmin-positive aberrant protein aggregates,[179] which eventually leads to heart failure. CryAB^{R120G} is a misfolded protein. CryAB^{R120G} mice display PFI resulting in further accumulation of misfolded protein aggregates in cardiomyocytes. These mice start to show early stage of compensatory

cardiac hypertrophy at 3 month of age (3m) and proceed to heart failure by 6 month of age (6m), making them an effective tool for therapeutic evaluation on disease progression.[107] CryAB^{R120G} tg mice were maintained in the FVB/N inbred background. S14A and S14D mice were cross-bred with CryAB^{R120G} tg mice respectively to generate heterozygous and homozygous S14A- or S14D-coupled hemizygous CryAB^{R120G} tg (S14A/+:: CryAB^{R120G}, S14A/S14A:: CryAB^{R120G} or S14D/+:: CryAB^{R120G}, S14D/S14D:: CryAB^{R120G}) mice, with their littermates of other genotypes used as controls to ensure the resultant mice are in the same genetic background.

Genotyping

The conventional polymerase chain reaction (PCR) was used for detection of tg GFPdgn and CryAB^{R120G} in mice using toe or tail clips and specific primers as previously reported.[107,176] The genotypes of Rnp6^{S14A} and Rpn6^{S14D} mice were determined with a modified PCR strategy using genomic DNA isolated from toe or tail clips, based on the tetra-primer amplification refractory mutation system (ARMS)-PCR principle described previously,[180,181] in which two non-allele-specific outer primers and two allele-specific inner primers were employed to detect single nucleotide polymorphisms. In brief, each PCR reaction was carried out in a total volume of 20 µl, containing ~200 ng of template DNA, 2 µl of 10X DreamTaq^{Tm} DNA Polymerase Green Buffer, 0.5 U of DreamTaq^{TM} DNA polymerase (Cat#EP0705, Thermo Scientific, Waltham, MA), 0.2 mM of dNTPs, outer primers, and inner primers; for S14A: 350 nM of outer primers and 150 nM of inner primers; for S14D: 200 nM of outer primers and 200 nM of inner primers. The primer sequences are listed below:

Outer (forward): 5'-GAGATGGCGATGGGGGAGCTCGTTTGTC-3'

Outer (reverse): 5'-CACAGTGAGTCAGCAGCACCATAGCCGGC-3'

Inner for S14A (forward): 5’-GGTGGTGGAGTTCCAGAGAGCCCGGG-3’

Inner for S14A (reverse): 5’-GCCTCCCGGTCGGTGCTGAGTAGGGA-3’

Inner for S14D (forward): 5’-GGTGGTGGAGTTCCAGAGAGCCCGGGA-3’

Inner for S14D (reverse): 5’-GCCTCCCGGTCGGTGCTGAGTAGGGA-3’

PCR amplifications for both S14A and S14D were performed with the following profile: 94 °C for 3 min, followed by 30 cycles of 30 sec at 94 °C, 30 sec of annealing, and 45 sec at 72 °C, ending with 10 min at 72 °C. Annealing temperature was 74.9 °C and 74.7 °C for S14A and S14D respectively. The PCR products were electrophoresed in 2% agarose gel and then digitally imaged with the Syngene InGenius LHR2 Gel Imaging System (Frederick, MD). The S14A and S14D genotypes of all mice used in this study were further confirmed through DNA sequencing the PCR products encompassing the mutation.

Mouse embryonic fibroblast (MEF) isolation

Mouse embryonic fibroblasts (MEFs) from WT and homozygous S14A mouse embryos were isolated as reported previously.[182] Briefly, pregnant mice at 14.5 days of gestation were anesthetized by injecting 2.5% of Avertin. The abdominal cavity was then opened and the entire uterus containing all embryos was dissected out. Embryos were removed aseptically and placed in sterile phosphate buffer saline (PBS) to wash out blood. After removal of the head and viscera, all fetuses were teased into fine pieces in 25 ml of 0.25% trypsin-EDTA (Cat#25300-056, Invitrogen, Waltham, MA) and the tissue was kept in a tube for digestion at 4 °C overnight. On the following day, the tubes with half of the trypsin aspirated off were kept in a 37 °C water bath to further digest for 30 min. The digested tissue was next mixed with 25 ml of MEF media [Dulbecco's modified Eagle medium (DMEM), 10% fetal bovine serum (FBS), 0.1 mM β-mercaptoethanol, 50 U

penicillin, 50 µg/ml streptomycin] and pipetted vigorously, followed by sedimentation by gravity for 1 min. The collected supernatant was plated with additional MEF media for culture in T75 culture flasks. MEFs were amplified and used for experimentation after the sixth passages.

Isolation and culture of adult mouse cardiomyocytes (AMCMs)

Cardiomyocytes from adult WT, S14A, and S14D mice were isolated as described previously.[183] In brief, chest cavity of a mouse under anesthesia with 2% inhaled isoflurane was opened, and the descending aorta and the inferior vena cava were cut. The heart was perfused via right ventricle with 7 ml of an EDTA buffer (130 mmol/l NaCl, 5 mmol/l KCl, 0.5 mmol/l NaH_2PO_4, 10 mmol/l HEPES, 10 mmol/l Glucose, 10 mmol/l 2,3-butanedione monoxime (BDM), 10 mmol/l Taurine, and 5 mmol/l EDTA) to flush out blood from the heart. The ascending aorta was then clamped. The clamped heart was removed and submerged in a dish of the EDTA buffer and was perfused via the left ventricle with 10 ml EDTA buffer. After that, the heart was transferred to a dish containing a perfusion buffer (130 mmol/l NaCl, 5 mmol/l KCl, 0.5 mmol/l NaH_2PO_4, 10 mmol/l HEPES, 10 mmol/l Glucose, 10 mmol/l BDM, 10 mmol/l Taurine, and 1 mmol/l $MgCl_2$) and injected via the left ventricle with 3 ml of the perfusion buffer to clear EDTA. The heart was then transferred to a dish containing a pre-warmed collagenase buffer (0.5 mg/ml Collagenase 2, 0.5 mg/ml Collagenase 4, and 0.05 mg/ml Protease XIV) and subsequently digested by injections of the collagenase buffer. Once the digestion was satisfied, the ventricular tissue was dissociated mechanically, and the enzymatic activity was inhibited using a Stop buffer (perfusion buffer containing 5% FBS). Then, cardiomyocytes were separated and calcium reintroduction buffers (mixture of perfusion buffer and culture media) were introduced in gradual increments by gravity settling. These separated cardiomyocytes were first plated on laminin (15 µg/ml)-coated

6-well dishes in plating media (M199, 5% FBS, 10 mmol/l BDM, and 1x Penicillin /Streptomycin) for 3 hours and cultured in culture media [M199, 0.1% BSA, 1x ITS (insulin, transferrin, selenium), 10 mmol/l BDM, 1x chemically defined lipid concentrate (CD lipid), and 1x Penicillin /Streptomycin] for another 48 hours prior to further experimentation.

Neonatal rat/mouse cardiomyocyte culture and adenoviral infection

Neonatal rat cardiomyocytes (NRCMs) were isolated from the ventricles of 2-day-old male and female Sprague-Dawley rats, and neonatal mouse cardiomyocytes (NMCMs) were isolated from the ventricles of 1-day-old male and female WT and S14D mice with the Cellutron Neomyocytes Isolation System (Cat#nc-6031, Cellutron Life Technology, Baltimore, MD) following the manufacturer's instructions, plated on 35 mm dishes in 10% fetal bovine serum, and cultured as described previously[128]. The creation of the recombinant replication-deficient adenoviruses harboring the expression cassette for a Hemagglutinin epitope (HA)-tagged CryAB^{R120G} (Ad-HA-CryAB^{R120G}) was described.[77] The plated cells were infected with Ad-HA-CryAB^{R120G} virus at approximately 10 multiplicities of infection (MOIs) in serum-free Dulbecco's minimum essential medium (DMEM) for 6 hr. The cells were then cultured in DMEM containing 2% serum for 48 hr before drug treatment/harvest.

Methods for Randomization and Sample Size Determination

In assigning mice or cultured cells of the same genotype into different control and treatment groups, the flipping a coin randomization method was used. To determine the minimum number of mice per group required for the serial echocardiography study, power calculation was use with α=0.05, β=0.80, and the estimated differential and variation of cardiac output (CO, the preliminary

readout) generated from the pilot and prior studies. For experiments using primarily biochemical and molecular biology assessments, the sample size was determined empirically or on basis of prior reports, for example, 3 repeats for cell culture experiments.[77]

Total protein extraction

To extract total proteins, ventricular myocardium or cultured cardiomyocytes were homogenized in 1x sampling buffer [41 mM Tris-HCl (pH 6.8), 1.2% SDS and 8% glycerol]. A 1x complete protease and phosphatase inhibitor cocktail (containing 80 μM aprotinin, 5 mM bestatin, 1.5 mM E-64, 2 mM leupeptin hemisulfate, 10 mM β-glycerophosphate, 50 mM sodium fluoride, 1 mM sodium orthovanadate, and 10 mM sodium pyrophosphate decahydrate, Cat#HB9105, Hello Bio Inc., Princeton, NJ) was added to the sampling buffer to protect proteins from endogenous proteases and phosphatases. The protein homogenates were boiled for 5 min. After centrifugation at 10,621 x g for 10 min at 4 °C, the supernatant was collected as the total protein extracts. Protein concentrations were determined using Pierce™ bicinchoninic acid (BCA) protein assay reagents (Cat#23222 & #23224, Thermo Fisher Scientific, Waltham, MA).

Extraction of the NP-40–soluble and NP-40–insoluble fractions

The protocol for the fractionation of NP-40 soluble and insoluble proteins was developed by Guo et al..[184] Briefly, for cultured cells, cells were washed in cold PBS (pH 7.4) and harvested into cell lysis buffer [50 mM Tris-HCl (pH 8.8), 100 mM NaCl, 5 mM $MgCl_2$, 0.5% NP-40, and 2 mM dithiothreitol (DTT)] containing 1x complete protease and phosphatase cocktail. For tissue, frozen ventricular myocardium was powdered and gently homogenized in the cell lysis buffer. After incubation on ice for 30 min, cell lysates were centrifuged at 17,000 x g for 15 min at 4 °C. The

supernatant was collected as the NP-40–soluble (NS) fraction. The NS fraction added with 3x SDS boiling buffer [6% SDS, 20 mM Tris-HCl (pH 8.0), and 150 mM DTT] was boiled for 5 min. The pellets containing NP-40–insoluble (NI) fraction were washed with PBS and resuspended in cell pellet buffer [20 mM Tris-HCl (pH 8.0), 15 mM $MgCl_2$, 2 mM DTT and 1x complete protease and phosphatase inhibitor cocktail], followed by 30-min incubation on ice. The NI fraction was further solubilized in 3x SDS boiling buffer and boiled for 5 min. Protein concentrations were then determined with a reducing agent-compatible BCA protein assay kit (Cat#23252, Thermo Fisher Scientific, Waltham, MA).

Western blot analysis

Equal amounts of proteins were fractionated via 10-14% SDS-polyacrylamide gel electrophoresis (SDS-PAGE) and transferred onto a polyvinylidene difluoride (PVDF) membrane using a Trans-Blot apparatus (Bio-Rad, Hercules, CA). Five to 10 μg proteins were loaded for CryAB; 60 μg proteins were loaded for pS14-Rpn6; 15-20 μg proteins were loaded for examining other proteins. After blocking in 2% BSA or 2% ECL™ advanced blocking agents (Cat#RPN418, Cytiva, Marlborough, MA) in TBST for 1 hour at room temperature, the PVDF membrane was immunodetected with primary antibodies and subsequently appropriate horseradish peroxidase (HRP)-conjugated secondary antibodies (Jackson ImmunoResearch, West Grove, PA). The secondary antibodies bound to PVDF membrane were detected with SuperSignal™ West Pico PLUS Chemiluminescent Substrate (Cat#34578, Thermo Fisher Scientific, Waltham, MA). Blots were digitally imaged with the ChemiDoc™ MP imaging system and analyzed with Image Lab software (Bio-Rad, Hercules, CA). The in-lane total protein signals derived from the stain-free

image were used as the loading control as previously described.[185] The antibodies used for Western blot are listed below:

Target antigen	**Source**	**Working concentration**
Ser14-phosphorylated Rpn6	Custom made	1:20000
Phosphorylated PKA substrates	Cell Signaling Cat#9624	1:1000
Rpn6	MyBioSource Cat#MBS9605099	1:1000
β5	Custom made	1:10000
Rpt2	Enzo Life Sciences Cat#BML-PW8305	1:1000
GFP	Santa Cruz Biotechnology Cat#SC-9996	1:1000
CryAB	Enzo Life Sciences Cat#ADI-SPA-223	1:10000
Ubiquitin	Cell Signaling Cat#58395	1:1000
Ubiquitin, lys48-specific	Millipore Cat#05-1307	1:1000
HA-tag	Cell Signaling Cat#3724	1:5000
Peroxidase-conjugated AffiniPure Goat Anti-Mouse IgG (H+L)	Jackson ImmunoResearch Cat#115-035-003	1:10000
Peroxidase-conjugated AffiniPure Goat Anti-Rabbit IgG (H+L)	Jackson ImmunoResearch Cat#111-035-003	1:10000

Proteasome peptidase activity assays

Proteasome peptidase activity assays were performed as described previously.[132] Briefly, cultured cardiomyocytes or snap-frozen ventricular myocardial tissue samples were homogenized in the crude protein extraction buffer [50 mM Tris-HCl (pH 7.5), 250 mM sucrose, 5 mM $MgCl_2$, 0.5 mM EDTA, 1 mM DTT, 0.025% digitonin, and 1x complete protease and phosphatase inhibitor

cocktail] on ice, followed by centrifugation at 6800 x g for 10 min at 4 °C. The supernatant was collected, and protein concentrations were determined with BCA reagents. Five μg of cellular proteins or 10 μg of myocardial proteins in 200 μl proteasome assay buffer [50 mM Tris-HCl (pH 7.5), 40 mM KCl, 5 mM $MgCl_2$, 1 mM DTT, and 0.5 mg/ml BSA] were loaded in a 96-well microplate (#655076, Greiner Bio-One, Germany). The chymotrypsin-like, caspase-like and trypsin-like activities of 26S proteasomes were determined in the presence of 0.2 mM, 0.4 mM and 0.4 mM ATP, respectively. The assays were carried out in the presence or absence of the proteasome inhibitors: 0.28 μM bortezomib (BZM, Cat#B-1408, LC Laboratories, Woburn, MA) for chymotrypsin-like and caspase-like activities, and 5 μM epoxomicin (Cat#A2606, APExBIO, Houston, TX) for trypsin-like activity. The proteasome inhibitor suppressible portion of peptide cleavage activity is attributed to the proteasome. The following fluorogenic substrates were applied: Suc-LLVY-AMC (18 μM; Cat#10008119, Cayman Chemical, Ann Arbor, MI), Z-LLE-AMC (45 μM; Cat#10008117, Cayman Chemical, Ann Arbor, MI), and Bz-VGR-AMC (40 μM; Cat#BML-BW9375, Enzo Life Sciences, Farmingdale, NY), for chymotrypsin-like, caspase-like and trypsin-like activities, respectively. The temporal changes in fluorescence intensity were measured immediately after the initiation of the reaction using a Perkin Elmer plate reader (Model VICTOR Nivo™, Waltham, MA) at an excitation wavelength of 380 nm and an emission wavelength of 460 nm. The slope of the log phase of the reaction curve was measured as the indicator of the corresponding proteasome activity.

Echocardiography

Serial echocardiography was performed on mice as previously reported.[128] In brief, mice were kept in light anesthesia with inhalation of Isoflurane (4% for induction and 1-1.5% for maintenance)

via a face mask. Transthoracic echocardiography was performed using the VisualSonics Vevo 3100 system and a 40-MHz probe (FUJIFILM VisualSonics, Toronto, ON, Canada). A two-dimensional echocardiogram guided M-mode echocardiography was acquired through the LV anterior and posterior walls at the short axis view. Parameters of LV were derived from primary measurements using Vevo LAB software, based on the following formula:

$$\text{LVEDV } (\mu\text{l}) = \frac{7.0}{2.4 + \text{LVID;d}} \times \text{LVID;d}^3$$

$$\text{LVESV } (\mu\text{l}) = \frac{7.0}{2.4 + \text{LVID;s}} \times \text{LVID;s}^3$$

$$\text{EF } (\%) = \frac{\text{LVEDV} - \text{LVESV}}{\text{LVEDV}} \times 100\%$$

$$\text{FS } (\%) = \frac{\text{LVID;d} - \text{LVID;s}}{\text{LVID;d}} \times 100\%$$

$$\text{SV } (\mu\text{l}) = \text{LVEDV} - \text{LVESV}$$

$$\text{CO (ml/min)} = \text{SV} \times \text{HR} \,/\, 1000$$

$$\text{LV mass (mg)} = \left[(\text{LVID;d} + \text{LVPW;d} + \text{IVS;d})^3 - \text{LVID;d}^3\right] \times 1.05 \text{ g/ml}$$

LVEDV, LV end-diastolic volume; LVESV, LV end-systolic volume; LVID;d, LV end-diastolic internal dimension; LVID;s, LV end-systolic internal dimension; EF, ejection fraction; FS, fractional shortening; SV, stroke volume; CO, cardiac output; HR, heart rate; IVS;d, end-diastolic interventricular septum thickness.

RNA isolation and qRT-PCR

Total RNA was isolated from ventricular myocardium using the TRI Reagent® (Cat#TR 118, Molecular Research Center Inc., Cincinnati, OH) as described previously.[185] RNA concentrations were determined with a NanoDrop 2000 UV Spectrophotometer (Thermo Scientific, Waltham,

MA) following the manufacturer's instruction. A High Capacity cDNA Reverse Transcription Kit (Cat#4368814, Applied Biosystems, Waltham, MA) was used to generate cDNA by following the manufacturer's protocol. PowerUp™ SYBR™ Green Master Mix (Cat#A25742, Applied Biosystems, Waltham, MA) was used to conduct quantitative real-time PCR (qPCR) analysis. All qPCR reactions were performed under the following condition: 50 °C for 2 min, 95 °C for 10 min, followed by 40 cycles of amplification at 95 °C for 15 sec and 60 °C for 60 sec. All reactions for reference (*GAPDH*) and target (*GFPdgn*, *CryAB*^{tg}, *Nppa*, *Nppb*, *Myh7* and *Myh6*) genes were done in duplicate and the average value was used for subsequent quantification. The $2^{-\Delta\Delta Ct}$ method using *GAPDH* as the normalization gene was used to calculate the relative expression of target genes. Reverse transcription and qPCR were performed with a Techne 5PRIMEG/02 Thermal Cycler (United Kingdom) and Applied Biosystems StepOnePlus Real-Time PCR system (Waltham, MA), respectively. The following primer pairs were used in this study:

GAPDH (forward): 5'-ATGACATCAAGAAGGTGGTG-3'

GAPDH (reverse): 5'-CATACCAGGAAATGAGCTTG-3'

GFPdgn (forward): 5'-TCTATATCATGGCCGACAAGCAGA-3'

GFPdgn (reverse): 5'-ACTGGGTGCTCAGGTAGTGGTTGT-3'

CryAB^{tg} (forward): 5'-TTCTTCGGAGAGCACCTGTT-3'

CryAB^{tg} (reverse): 5'-CCCCAGAACCTTGACTTTGA-3'

Nppa (forward): 5'-GGAGGAGAAGATGCCGGTAGA-3'

Nppa (reverse): 5'-GCTTCCTCAGTCTGCTCACTCA-3'

Nppb (forward): 5'-CTGCTGGAGCTGATAAGAGA-3'

Nppb (reverse): 5'-TGCCCAAAGCAGCTTGAGAT-3'

Myh7 (forward): 5'-GGAGGCACAGACCAGGC-3'

Myh7 (reverse): 5'-GATAGGCGTTGTCAGAGATGG-3'

Myh6 (forward): 5'-GCCAAGGTCGTGTCCCG-3'

Myh6 (reverse): 5'-GGCACCACTTCCGCATTG-3'

Immunofluorescence staining and confocal microscopy

Immunofluorescence staining and confocal microscopy were performed as described.[128] In brief, ventricular myocardium was fixed with 4% paraformaldehyde, equilibrated in a gradual increment of sucrose, and embedded in the Tissue-Tek O.C.T in a Cryomold. The mold was placed on top of the aluminum plate on the dry ice-methanol bath for rapid freezing until the OCT was completely frozen. The frozen tissue block was then cut with a -20 °C cryostat to obtain 7-μm cryosections, or stored at -80 °C for future use. For GFPdgn direct fluorescence, the myocardial sections were stained with Alexa Fluor 568-conjugated phalloidin (1:400; Cat#A12380, Invitrogen, Waltham, MA) to reveal F-actin that identifies cardiomyocytes. For CryAB-positive aggregates, the myocardial sections were sequentially stained with the rabbit anti-CryAB antibody (1:100; Cat#ADI-SPA-223, Enzo Life Sciences, Farmingdale, NY), Alexa Fluor 647-conjugated anti-rabbit secondary antibody (1:500; Cat#111-605-003, Jackson ImmunoResearch, West Grove, PA), and Alexa Fluor 488-conjugated phalloidin (1:2000; Cat#20478, Cayman Chemical, Ann Arbor, MI). DAPI (Cat#0100-20, SouthernBiotech, Birmingham, AL) was used for staining nuclei. GFPdgn direct fluorescence (green), CryAB immunofluorescence, and the stained F-actin were visualized and imaged using a Leica TCS SP8 confocal microscope (Leica Microsystems Inc., Buffalo Grove, IL). The fluorescence micrographs of the experimental and control groups were collected using the same imaging setting and processed the same way.

Native gel electrophoresis followed by immunoblotting

Native gel electrophoresis followed by immunoblotting was performed as described,[128] with minor modification. Snap-frozen ventricular myocardial tissue samples were homogenized in the extraction buffer [50 mM Tris-HCl (pH 7.5), 250 mM Sucrose, 5 mM $MgCl_2$, 1 mM DTT, 1 mM ATP, and 1x complete protease and phosphatase inhibitor cocktail] before centrifugation at 15,000 x g for 30 min at 4 °C. Protein concentrations were determined using Pierce™ bicinchoninic acid (BCA) protein assay reagents (Cat#23222 & #23224, Thermo Fisher Scientific, Waltham, MA) and samples were diluted to comparable concentration with the extraction buffer. Then, 4x native gel loading buffer [200 mM Tris-HCl (pH 6.8), 60% (v/v) glycerol, and 0.05% (w/v) bromophenol blue] was added to each aliquot of protein samples before loading. Twenty-five μg of proteins were loaded in 4% native polyacrylamide gel and the gel electrophoresis was performed at 4 °C at a constant voltage of 100 V for 4-4.5 hours. The proteins were then transferred onto a PVDF membrane at a constant current of 250 mA for 90 min, or overnight at a constant current of 40 mA, for subsequent immunoblotting for β5 (1:10000; custom made) and Rpt2 (1:1000; Cat#BML-PW8305, Enzo Life Sciences, Farmingdale, NY). The in-lane total protein signal derived from the stain-free image was used as the loading control.

Statistical methods

GraphPad Prism version 9.5.0 (San Diego, CA) was used. All continuous variables are presented as Mean±SEM unless indicated otherwise. All data were examined for normality with the Shaprio Wilk's test prior to application of parametric statistical tests. Tests used for evaluation of statistical significance are specified in figure legends. In brief, unless otherwise indicated, differences between two groups were evaluated by two-tailed unpaired Student's *t* test; differences

among 3 or more groups were evaluated by one-way or, where appropriate, two-way ANOVA followed by Tukey's test for pairwise comparisons. Serial echocardiographic data were evaluated by two-way or, where appropriate, three-way repeated measures ANOVA followed by Tukey's multiple comparisons. Mouse Kaplan-Meier survival curves were compared with the log-rank test. A p value or adjusted p value <0.05 is considered statistically significant.

RESULTS

PART I. Creation and Baseline Characterization of Rpn6^{S14A} and Rpn6^{S14D} Mice

To facilitate the investigation in to the (patho)physiological significance of pS14-RPN6, we created two knock-in mouse models in which the codon for Ser14 of endogenous *Rpn6*/*Psmd11* gene was mutated via CRISPR/Cas9 to encode either Ala (S14A) or Asp (S14D) to block or mimic pS14-Rpn6, respectively. Mice harboring the *Rpn6^{S14A}* (referred as S14A hereafter) and *Rpn6^{S14D}* (referred as S14D hereafter) alleles were created in the C57BL/6J inbred background and were confirmed genetically by sequencing the targeted segment of the *Psmd11* gene (**Figure 1**). Both S14A and S14D mice used in the present study had undergone six or more generations of backcross into WT C57BL/6J inbred background to eliminate any off-target mutations potentially resulted from CRISPR/Cas9. Prior to applying the two knock-in mouse models to investigate the (patho)physiological significance of pS14-Rpn6, it is of great importance to determine the effect of these genetic modifications on the general wellbeing of the mice. Hence, in this section, we evaluated the baseline characteristics of S14A and S14D mice. Heterozygous and Homozygous S14A and S14D mice are viable and fertile and do not display discernible gross abnormalities compared with their littermate controls during the first 12 months of age, the longest time observed in full cohorts so far.

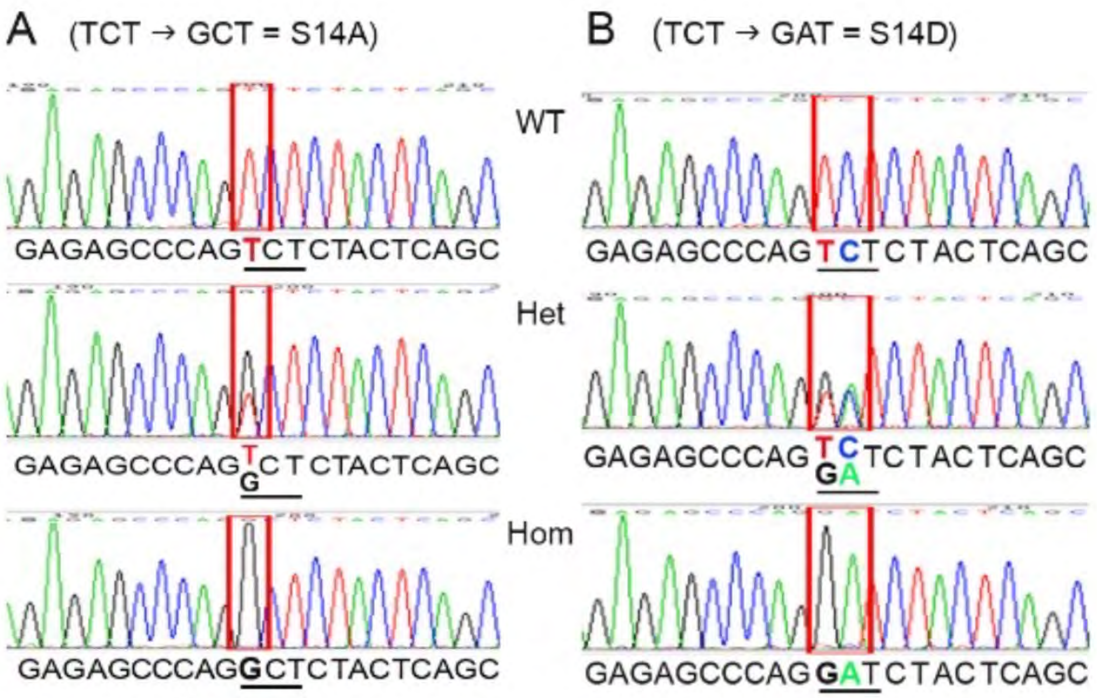

Figure 1. **Representative DNA sequencing histograms of genotyping PCR products of the genomic region harboring the coding sequence for Ser14 of Rpn6 in mice.**

Het, heterozygous; Hom, homozygous.

1.1. The basal effect of genetic blockade of pS14-Rpn6 on mice

1.1.1. Serial echocardiographic characterization of WT and S14A mice

To determine whether genetic blockade of pS14-Rpn6 might have an impact, we performed serial echocardiography on homozygous S14A mice and their littermate WT control mice monthly to characterize mouse cardiac morphology (**Figure 2B-2I, Table 1-6**) and function (**Figure 3, Table 1-6**). Virtually, we did not observe discernible differences in body weight (**Figure 2A, left panel**) echocardiogram-estimated LV mass (**Figure 2B, left panel**), LV mass-to-body weight ratio (LV mass/BW, **Figure 2C, left panel**), or any other essential echocardiographic parameters including LV posterior wall thicknesses (LVPW;d, LVPW;s; **Figure 2D, 2G, left panels**), internal dimensions (LVID;d, LVID;s; **Figure 2E, 2H, left panels**) and volumes (LVEDV, LVESV; **Figure 2F, 2I, left panels**) at both end-diastole and end-systole, ejection fraction (EF; **Figure 3A, left panel**), fractional shortening (FS; **Figure 3B, left panel**), stroke volume (SV; **Figure 3C, left panel**), cardiac output (CO; **Figure 3D, left panel**), and heart rate (HR; **Figure 3E, left panel**) between S14A mice and WT mice of the same sex, throughout 7 months, the longest period for serial echocardiography assessment. This is confirmed by statistical analyses, with the exceptions that S14A males displayed lower EF at 4 months (4m) ($p=0.0469$, **Table 3**) and LV mass at 7m ($p=0.0444$, **Table 6**) than WT males. The difference in EF can be explained by the exceptionally greater EF in WT mice at this time point, which could have been picked up randomly by manual handling or mouse circumstances. Furthermore, we discovered that female WT mice exhibited smaller LV chamber size prominently at end-diastole (LVID;d, LVEDV) than male WT mice, while sex differences disappeared in S14A mice at individual time points; this is consistent with the lower body weight and/or LV mass of female WT mice than male ones (**Figure 2A, 2B, 2E, 2F, left panels, Table 1-6**). We further analyzed the integrated data of the entire 7 months of

assessment period using area under curve (AUC) of each parameter which reflects the mouse kinetic adaption to S14A knock-in (**Figure 2 and Figure 3, right panels**). The overall differences due to S14A knock-in were found only in SV ($p=0.0201$) and HR ($p=0.0001$); more specifically, S14A male mice displayed smaller SV (**Figure 3C, right panel**) and higher HR (**Figure 3E, right panel**) than WT male mice. The raise in HR was likely a compensatory response to the decreased SV, resulting in unchanged CO. Although no significant differences were obtained from individual time-point assessment, AUC analyses revealed that female mice overall had smaller body weight ($p<0.0001$) and LV mass ($p<0.0001$), thinner LVPW;d ($p<0.0001$) and LVPW;s ($p=0.0009$), smaller LV chamber (LVID;d, $p<0.0001$; LVID;s, $p=0.0012$; LVEDV, $p<0.0001$; LVESV, $p=0.0007$), and lower SV ($p=0.0046$) and CO ($p=0.0010$) than male mice, along with comparable LV mass/BW, EF, FS and HR (**Figure 2 and Figure 3, right panels**); notably, sex differences in LVPW;s (**Figure 2G, right panel**), SV (**Figure 3C, right panel**) and CO (**Figure 3D, right panel**) were obtained only in WT mice.

We also checked the body weight of older mice (10m). Similar to the findings from the first 7-month assessment, no discernible changes due to S14A knock-in were found in either males or females. Although there was a statistically significant difference in body weight between males and females overall ($p=0.0107$), it was not attained within the same genotype (**Figure 4**).

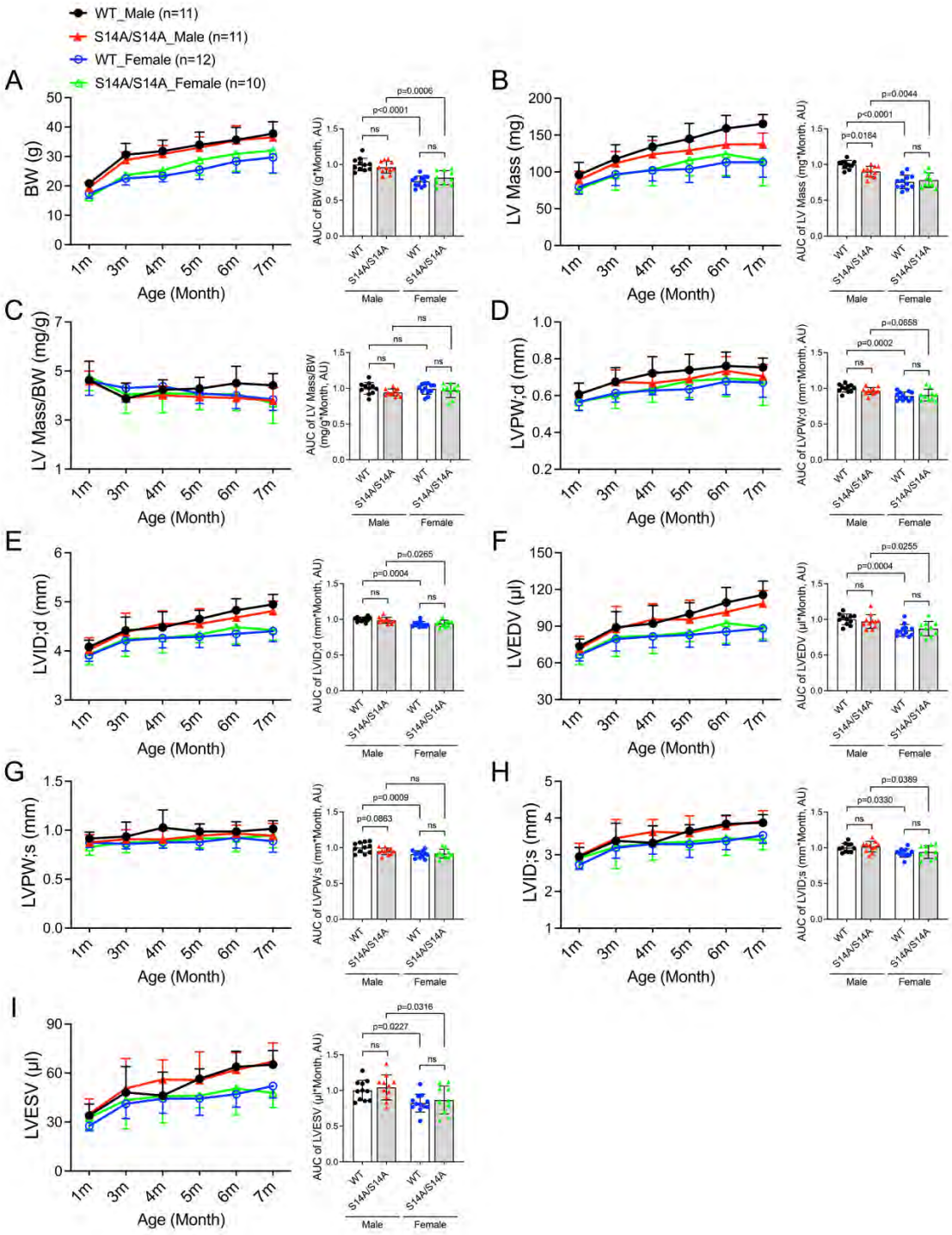

Figure 2. Body weight and cardiac morphometric characteristics of WT and S14A mice.

A ~ I, Littermate mice of indicated genotypes were subjected to serial echocardiography at 1, 3, 4, 5, 6, and 7 months (m). LV morphological parameters derived from the echocardiography are presented. The stacked line chart of each panel summarizes the time course of changes in the indicated parameter. The detailed values of echocardiographic parameters are listed and statistical significance between genotypes or sexes at the same time point are indicated in **Table 1 ~ 6**. The bar graph with scattered dots of each panel presents the Area Under Curve (AUC) of the indicated parameter versus time obtained with the trapezoidal rule. Each dot represents an individual mouse; mean±SD; repeated three-way ANOVA followed by Tukey's test for the time-course curves, and two-way ANOVA followed by Tukey's test for the bar graphs; BW, body weight; LVPW;d/LVPW;s, LV posterior wall thickness at end-diastole/end-systole; LVID;d/LVID;s, LV internal dimension at end-diastole/end-systole; LVEDV/LVESV, LV volume at end-diastole/end-systole; ns, not significant.

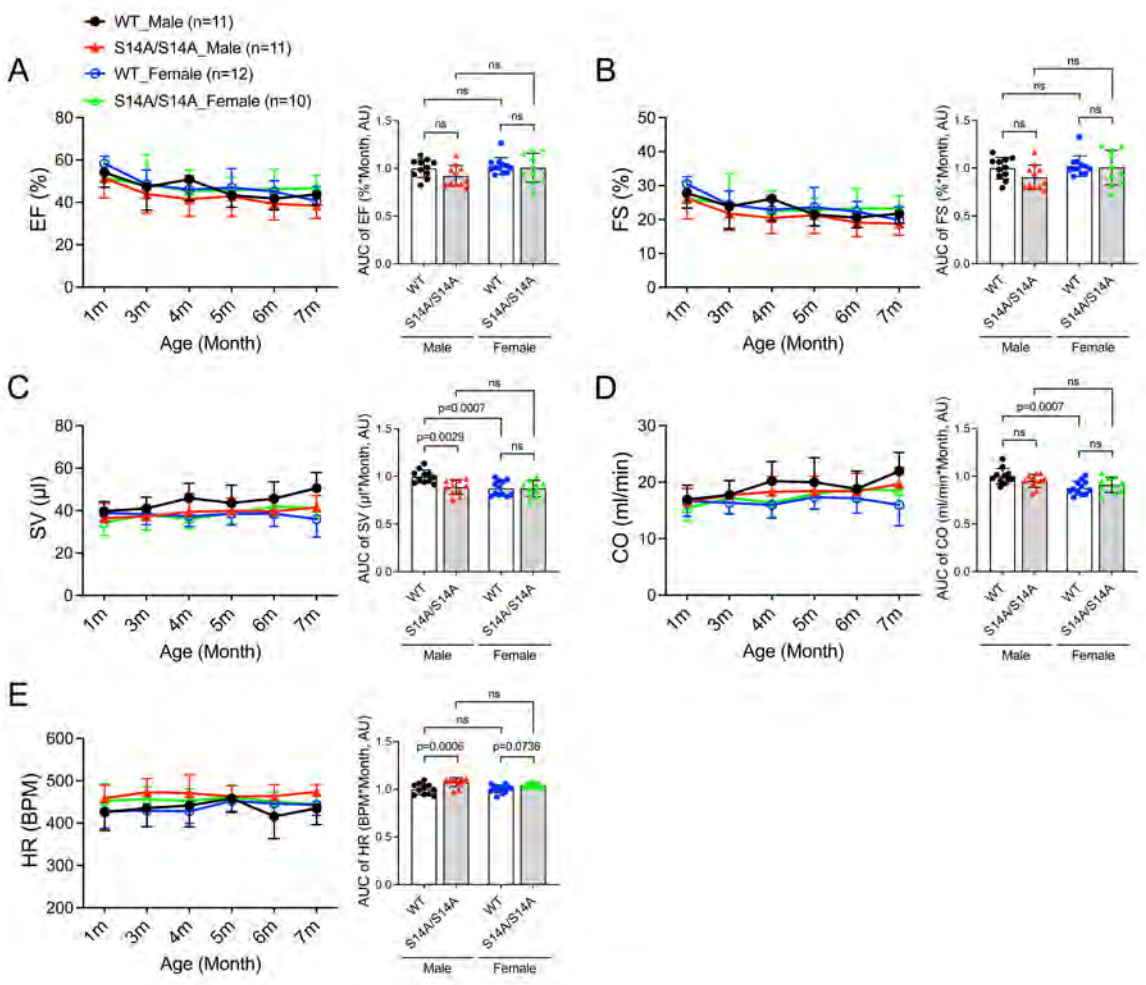

Figure 3. **Cardiac functional characteristics of WT and S14A mice.**

A ~ **E**, LV echocardiographic functional parameters from the same cohort of mice used for Figure 2 are presented. The stacked line chart of each panel summarizes the time course of changes in the indicated parameter. The detailed values of echocardiographic parameters are listed and statistical significance between genotypes or sexes at the same time point are indicated in **Table 1 ~ 6**. The bar graph with scattered dots of each panel presents the AUC of the indicated parameter versus time obtained with the trapezoidal rule. Each dot represents an individual mouse; mean±SD; repeated three-way ANOVA followed by Tukey's test for the time-course

curves, and two-way ANOVA followed by Tukey's test for AUC; EF, ejection fraction; FS, fractional shortening; SV, stroke volume; CO, cardiac output per minute; HR, heart rate.

Table 1. Echocardiographic parameters from WT and S14A mice at 1m

	WT		S14A/S14A	
	Male	Female	Male	Female
N	11	12	11	10
BW (g)	20.8±1.4	17.4±1.7**	19.4±1.8	16.1±1.0
LV mass (mg)	96.2±16.8	79.4±9.4	89.1±11.9	76.5±6.7
LV mass/BW (mg/g)	4.63±0.77	4.59±0.58	4.58±0.42	4.76±0.57
HR (bpm)	425±43	428±40	459±31	453±41
EF (%)	54.16±7.04	58.39±3.35	51.41±9.31	51.41±8.22
FS (%)	27.83±4.47	30.41±2.27	26.19±6.03	26.04±5.10
SV (μl)	39.7±4.5	38.8±3.7	36.5±6.9	34.3±5.9
CO (ml/min)	16.9±2.6	16.7±2.7	16.6±2.3	15.4±2.2
LVPW;d (mm)	0.61±0.06	0.57±0.05	0.61±0.06	0.57±0.04
LVPW;s (mm)	0.91±0.07	0.87±0.05	0.88±0.08	0.83±0.089
LVID;d (mm)	4.09±0.14	3.91±0.12	4.03±0.24	3.92±0.20
LVID;s (mm)	2.95±0.25	2.72±0.12	2.98±0.34	2.90±0.28
LVEDV (μl)	73.7±5.7	66.5±4.9	71.5±10.2	67.0±8.5
LVESV (μl)	34.0±7.0	27.7±3.1	35.0±9.1	32.8±7.5

BW, body weight; LV, left ventricle; HR, heart rate; EF, ejection fraction; FS, fractional shortening; SV, stroke volume; CO, cardiac output per minute; LVPW;d, LV end-diastolic posterior wall thickness; LVPW;s, LV end-systolic posterior wall thickness; LVID;d, LV end-diastolic internal dimension; LVID;s, LV end-systolic internal dimension; LVEDV, LV end-diastolic volume;

LVESV, LV end-systolic volume. Mean±SD; repeated three-way ANOVA followed by Tukey's test; **$p<0.01$ vs. male mice with same genotype.

Table 2. Echocardiographic parameters from WT and S14A mice at 3m

	WT		S14A/S14A	
	Male	Female	Male	Female
N	11	12	11	10
BW (g)	30.6±3.9	22.5±2.2**	28.8±2.7	23.7±1.5*
LV mass (mg)	117.6±19.4	96.8±15.1	111.8±16.0	95.7±20.4
LV mass/BW (mg/g)	3.87±0.63	4.31±0.58	3.91±0.61	4.04±0.77
HR (bpm)	435±44	429±38	473±32	457±29
EF (%)	47.22±10.92	48.53±6.69	43.92±8.93	48.49±14.11
FS (%)	23.84±6.55	24.34±4.07	21.72±4.97	24.79±8.71
SV (μl)	40.9±5.4	38.3±5.0	37.3±4.4	37.9±7.2
CO (ml/min)	17.8±2.5	16.4±2.0	17.7±2.6	17.2±2.7
LVPW;d (mm)	0.68±0.08	0.61±0.05	0.67±0.07	0.60±0.08
LVPW;s (mm)	0.94±0.15	0.86±0.05	0.91±0.10	0.87±0.10
LVID;d (mm)	4.42±0.27	4.21±0.21	4.38±0.39	4.24±0.35
LVID;s (mm)	3.38±0.48	3.19±0.29	3.45±0.51	3.21±0.59
LVEDV (μl)	89.0±12.8	79.5±9.8	87.9±18.3	81.3±15.9
LVESV (μl)	48.1±15.9	41.2±9.1	50.6±18.3	43.4±17.7

Mean±SD; repeated three-way ANOVA followed by Tukey's test; *$p<0.05$, **$p<0.01$ vs. male mice with same genotype.

Table 3. Echocardiographic parameters from WT and S14A mice at 4m

	WT		S14A/S14A	
	Male	Female	Male	Female
N	11	12	11	10
BW (g)	31.8±3.7	23.4±2.0**	30.8±2.9	25.2±2.4
LV mass (mg)	134.1±14.1	102.2±14.4*	123.9±19.0	103.1±21.8
LV mass/BW (mg/g)	4.23±0.40	4.38±0.48	4.01±0.37	4.09±0.79
HR (bpm)	442±50	428±28	471±43	452±29
EF (%)	50.82±10.02	46.03±6.54	41.58±8.29$^{\#}$	45.34±9.97
FS (%)	26.07±6.41	22.85±3.85	20.44±4.61	22.57±5.79
SV (μl)	45.9±6.9	37.3±4.8	39.5±8.5	36.2±4.6
CO (ml/min)	20.2±3.5	16.0±2.4	18.3±2.7	16.4±2.5
LVPW;d (mm)	0.72±0.09	0.63±0.02	0.67±0.06	0.64±0.07
LVPW;s (mm)	1.03±0.18	0.88±0.06	0.91±0.09	0.89±0.07
LVID;d (mm)	4.48±0.32	4.26±0.20	4.55±0.26	4.27±0.30
LVID;s (mm)	3.33±0.46	3.29±0.27	3.63±0.33	3.32±0.47
LVEDV (μl)	92.2±14.7	81.7±9.1	95.5±12.7	82.0±14.6
LVESV (μl)	46.2±14.3	44.3±8.9	56.1±12.1	45.9±16.6

Mean±SD; repeated three-way ANOVA followed by Tukey's test; *$p<0.05$, **$p<0.01$ vs. male mice with same genotype; $^{\#}p<0.05$ vs. WT mice of same sex.

Table 4. Echocardiographic parameters from WT and S14A mice at 5m

	WT		S14A/S14A	
	Male	Female	Male	Female
N	11	12	11	10
BW (g)	33.9±4.3	25.4±3.2*	33.0±3.7	28.8±5.2
LV mass (mg)	145.0±21.0	103.9±18.3	129.2±12.4	115.7±21.0
LV mass/BW (mg/g)	4.28±0.46	4.08±0.41	3.94±0.36	4.06±0.63
HR (bpm)	458±33	452±24	463±25	462±28
EF (%)	43.34±5.64	46.98±8.92	42.85±9.65	45.72±5.88
FS (%)	21.42±3.33	23.59±5.86	21.21±5.42	22.68±3.43
SV (μl)	43.5±8.4	38.5±5.3	39.9±6.0	38.6±4.9
CO (ml/min)	20.0±4.3	17.3±2.1	18.4±2.6	17.9±2.7
LVPW;d (mm)	0.74±0.09	0.63±0.06	0.69±0.05	0.68±0.09
LVPW;s (mm)	0.99±0.08	0.88±0.08	0.95±0.12	0.92±0.10
LVID;d (mm)	4.65±0.18	4.29±0.22**	4.55±0.31	4.33±0.16
LVID;s (mm)	3.65±0.17	3.28±0.36	3.59±0.46	3.35±0.22
LVEDV (μl)	100.0±9.2	82.9±10.0**	95.5±15.8	84.8±7.5
LVESV (μl)	56.5±6.1	44.4±10.3	55.6±17.5	46.2±7.4

Mean±SD; repeated three-way ANOVA followed by Tukey's test; *$p<0.05$, **$p<0.01$ vs. male mice with same genotype.

Table 5. Echocardiographic parameters from WT and S14A mice at 6m

	WT		S14A/S14A	
	Male	Female	Male	Female
N	11	12	11	10
BW (g)	35.7±4.2	28.3±3.9	35.5±5.0	30.9±6.0
LV mass (mg)	159.0±17.7	113.1±20.4*	137.3±20.4	124.2±29.4
LV mass/BW (mg/g)	4.50±0.69	4.00±0.54	3.90±0.55	4.05±0.67
HR (bpm)	416±53	446±31	464±27	450±22
EF (%)	41.74±5.33	45.11±5.08	39.22±7.52	46.39±9.27
FS (%)	20.54±3.04	22.30±2.98	19.12±4.17	23.29±5.76
SV (μl)	45.6±7.9	38.5±5.9	39.6±7.1	41.9±5.3
CO (ml/min)	18.8±3.2	17.1±2.6	18.4±3.2	18.8±2.3
LVPW;d (mm)	0.76±0.08	0.68±0.07	0.74±0.08	0.69±0.10
LVPW;s (mm)	0.99±0.10	0.92±0.11	0.97±0.08	0.92±0.14
LVID;d (mm)	4.83±0.23	4.35±0.24*	4.68±0.15	4.49±0.34
LVID;s (mm)	3.84±0.24	3.38±0.24*	3.79±0.27	3.45±0.47
LVEDV (μl)	109.4±12.3	85.6±10.9*	101.6±7.9	92.4±16.6
LVESV (μl)	63.8±9.6	47.1±7.9*	62.0±10.6	50.5±16.0*

Mean±SD; repeated three-way ANOVA followed by Tukey's test; *$p<0.05$ vs. male mice with same genotype.

Table 6. Echocardiographic parameters from WT and S14A mice at 7m

	WT		S14A/S14A	
	Male	Female	Male	Female
N	11	12	11	10
BW (g)	37.7±4.0	29.7±5.3	36.5±5.2	32.0±7.7
LV mass (mg)	165.2±12.7	113.2±20.3***	137.3±15.3$^{\#}$	115.7±34.4
LV mass/BW (mg/g)	4.41±0.48	3.84±0.44	3.79±0.53	3.69±0.83
HR (bpm)	435±39	443±25	473±17	445±21
EF (%)	43.74±5.01	40.71±6.76	38.49±6.12	46.57±6.12
FS (%)	21.74±2.87	19.84±3.87	18.71±3.32	23.24±3.72
SV (μl)	50.5±7.4	36.0±8.5*	41.5±5.6	41.3±5.3
CO (ml/min)	21.9±3.3	16.0±3.7	19.7±2.9	18.4±3.1
LVPW;d (mm)	0.75±0.05	0.67±0.08	0.71±0.06	0.68±0.14
LVPW;s (mm)	1.01±0.08	0.89±0.11	0.94±0.13	0.95±0.13
LVID;d (mm)	4.95±0.20	4.40±0.22**	4.82±0.20	4.43±0.21
LVID;s (mm)	3.87±0.22	3.53±0.21	3.92±0.28	3.40±0.27
LVEDV (μl)	115.7±11.2	88.1±10.3**	108.5±10.6	89.2±9.9
LVESV (μl)	65.1±8.7	52.1±7.4	67.1±11.4	47.9±9.0

Mean±SD; repeated three-way ANOVA followed by Tukey's test; *$p<0.05$, **$p<0.01$, ***$p<0.001$ vs. male mice with same genotype; $^{\#}p<0.05$ vs. WT mice of same sex.

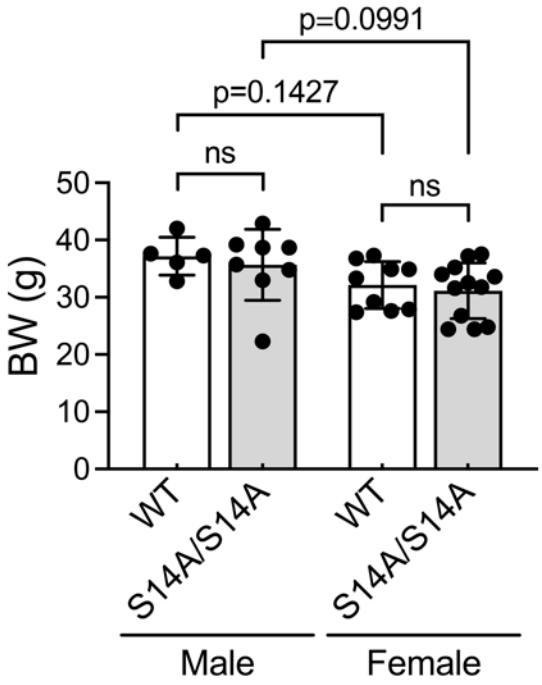

Figure 4. **Body weight of WT and S14A mice.**

Body weight of mice with indicated genotypes at 10m. Each dot represents an individual mouse; mean±SD; two-way ANOVA followed by Tukey's test.

1.1.2. Survival watch for WT and S14A mice

Serial echocardiographic data indicated that S14A mice exhibit comparable body weight and LV morphological and functional features, except for a lower SV in S14A male mice, compared with WT mice. Nevertheless, the S14A male mice were able to maintain their normal CO by raising HR. We therefore monitored the survival rate of a cohort of homozygous S14A mice (13 males and 11 females) and their WT littermates (15 males and 15 females). All of them survived for at least 358 days, the longest period of the observation, without visible abnormalities.

These data strongly suggest that, despite pS14-Rpn6 blockade, our S14A mice display similar cardiac functioning compared with WT mice for at least the first 7 months, and normal gross phenotypes and mortality for at least the first 12 months.

1.2. The basal effect of genetic mimicry of pS14-Rpn6 on mice

1.2.1. Serial echocardiographic characterization of WT and S14D mice

In terms of S14D mice, we are curious about whether constant stimulation of pS14-Rpn6 by genetic modification would alter the basal mouse cardiac function. With the same strategies used with S14A mice, we performed serial echocardiography on homozygous S14D mice and their littermate WT control mice at 1m, 3m, 4.5m, and 6m. Similarly, we observed virtually comparable body weight (**Figure 5A, left panel**), LVPW;d (**Figure 5D, left panel**), LVID;d (**Figure 5E, left panel**), LVEDV (**Figure 5F, left panel**), LVPW;s (**Figure 5G, left panel**), LVID;s (**Figure 5H, left panel**), LVESV (**Figure 5I, left panel**), EF (**Figure 6A, left panel**), FS (**Figure 6B, left panel**), SV (**Figure 6C, left panel**), CO (**Figure 6D, left panel**), and HR (**Figure 6E, left panel**) between S14D and WT mice of the same sex. Although the LV mass of WT females increased faster than that of S14D females (**Figure 5B, left panel; Table 10**), normalization by the body weight eliminated the difference (**Figure 5C, left panel**). Sex differences at individual time points were seen primarily in S14D mice: S14D females had lower body weight and/or LV mass throughout the 6-month assessment (**Table 7-10**), lower SV (p=0.0163) and CO (p=0.0061) at 3m (**Figure 6C, 6D, left panels; Table 8**), and smaller LV chamber at 4.5m (LVID;d, p=0.0010, **Figure 5E**; LVID;s, p=0.0109, **Figure 5H**; LVEDV, p=0.0010, **Figure 5F**; LVESV, p=0.0090, **Figure 5I, left panels**; **Table 9**) than S14D males. Again, we integrated the data of the entire period of assessment and analyzed AUC of each parameter (**Figure 5 and Figure 6, right panels**). The overall differences due to S14D knock-in were found in LV mass (p=0.0249) and LVPW;d (p=0.0102); more specifically, S14D females displayed lower LV mass (**Figure 5B, right panel**), thinner LVPW;d (**Figure 5D, right panel**) and LVPW;s (**Figure 5G, right panel**), and lower SV (**Figure 6C, right panel**) than WT females, whereas male WT and S14D mice showed no significant

differences in all parameters. Interestingly, these effects in S14D female mice seemed to manifest at early age and gradually diminish with the age. Nevertheless, these differences did not interfere with normal heart and body growth (LV mass/BW, body weight) or cardiac function (EF, FS, CO, HR). AUC analyses also revealed that female mice overall had lower body weight ($p<0.0001$) and LV mass ($p<0.0001$), thinner LVPW;d ($p=0.0019$) and LVPW;s ($p=0.0073$), smaller LV chamber (LVID;d, LVID;s, LVEDV, LVESV; $p<0.0001$), and lower SV ($p<0.0001$) and CO ($p=0.0006$) than male mice, along with comparable LV mass/BW, EF, FS and HR (**Figure 5 and Figure 6, right panels**); notably, sex differences in LVPW;d (**Figure 5D, right panel**), LVPW;s (**Figure 5G, right panel**), and CO (**Figure 6D, right panel**) were seen only in S14D mice. In addition, S14D and WT mice at 10m had similar body weights but a notable sex difference (**Figure 7**).

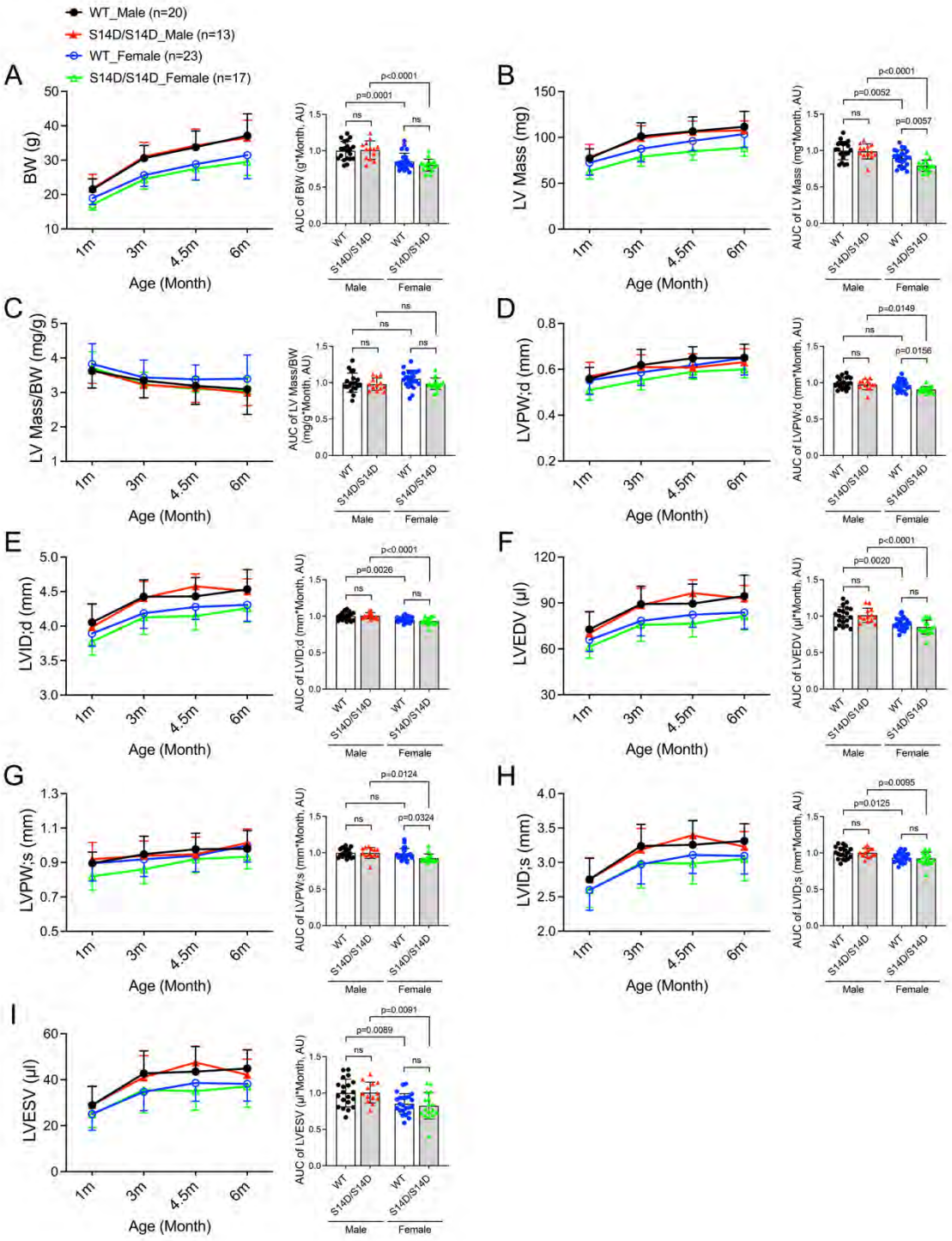

Figure 5. Body weight and cardiac morphometric characteristics of WT and S14D mice.

A ~ I, Littermate mice of indicated genotypes were subjected to serial echocardiography at 1m, 3m, 4.5m, and 6m. LV morphological parameters derived from the echocardiography are presented. The stacked line chart of each panel summarizes the time course of changes in the indicated parameter. The detailed values of echocardiographic parameters are listed and statistical significance between genotypes or sexes at the same time point are indicated in **Table 8 ~ 11**. The bar graph with scattered dots of each panel presents the AUC of the indicated parameter versus time obtained with the trapezoidal rule. Each dot represents an individual mouse; mean±SD; repeated three-way ANOVA followed by Tukey's test for the time-course curves, and two-way ANOVA followed by Tukey's test for the bar graphs.

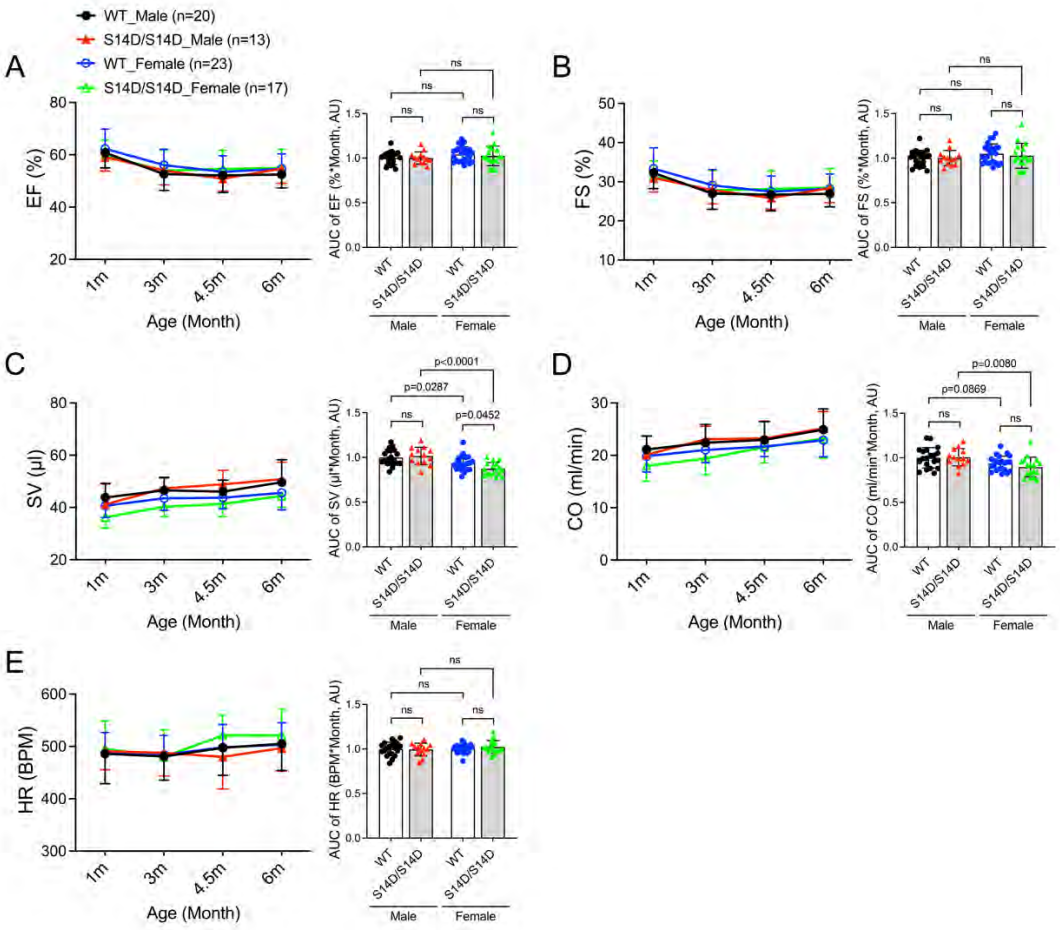

Figure 6. **Cardiac functional characteristics of WT and S14D mice.**

A ~ **E**, LV echocardiographic functional parameters from the same cohort of mice used for Figure 4 are presented. The stacked line chart of each panel summarizes the time course of changes in the indicated parameter. The detailed values of echocardiographic parameters are listed and statistical significance between genotypes or sexes at the same time point are indicated in **Table 8** ~ **11**. The bar graph with scattered dots of each panel presents the AUC of the indicated parameter versus time obtained with the trapezoidal rule. Each dot represents an individual mouse; mean±SD; repeated three-way ANOVA followed by Tukey's test for the time-course curves, and two-way ANOVA followed by Tukey's test for AUC.

Table 7. Echocardiographic parameters from WT and S14D mice at 1m

	WT		S14D/S14D	
	Male	Female	Male	Female
N	20	23	13	17
BW (g)	21.5±3.0	18.9±1.8	21.8±4.1	17.1±1.6*
LV mass (mg)	77.3±10.3	72.5±13.5	78.6±13.9	63.2±8.5
LV mass/BW (mg/g)	3.63±0.50	3.82±0.59	3.65±0.38	3.71±0.47
HR (bpm)	486±57	487±40	491±36	496±53
EF (%)	60.78±5.81	62.30±7.50	59.08±5.31	59.66±6.01
FS (%)	32.24±3.99	33.35±5.29	30.98±3.64	31.29±4.07
SV (μl)	43.8±5.4	40.7±4.5	41.2±7.8	36.3±4.1
CO (ml/min)	21.2±2.6	19.8±3.0	20.1±3.6	18.0±2.9
LVPW;d (mm)	0.56±0.05	0.55±0.06	0.57±0.06	0.51±0.04
LVPW;s (mm)	0.90±0.07	0.90±0.10	0.92±0.10	0.82±0.08
LVID;d (mm)	4.05±0.26	3.89±0.19	3.99±0.34	3.77±0.20
LVID;s (mm)	2.75±0.31	2.60±0.30	2.76±0.31	2.60±0.25
LVEDV (μl)	72.7±11.5	65.8±7.5	70.1±14.3	61.2±7.3
LVESV (μl)	28.9±8.2	25.1±7.1	29.0±8.3	24.9±5.7

Mean±SD; repeated three-way ANOVA followed by Tukey's test; *$p<0.05$ vs. male mice with same genotype.

Table 8. Echocardiographic parameters from WT and S14D mice at 3m

	WT		S14D/S14D	
	Male	Female	Male	Female
N	20	23	13	17
BW (g)	30.6±3.7	25.6±3.3**	31.0±4.2	24.5±2.9*
LV mass (mg)	101.4±14.5	87.5±14.1	99.3±13.6	78.9±10.1**
LV mass/BW (mg/g)	3.34±0.49	3.44±0.50	3.22±0.38	3.23±0.35
HR (bpm)	481±45	484±37	488±44	480±52
EF (%)	52.60±6.22	56.06±6.03	54.03±5.56	53.98±7.80
FS (%)	26.98±4.02	29.10±4.02	27.86±3.53	27.79±5.08
SV (μl)	46.6±5.0	43.5±4.6	47.3±4.0	40.3±3.9*
CO (ml/min)	22.4±3.5	21.0±2.5	23.0±2.5	19.4±3.1**
LVPW;d (mm)	0.62±0.07	0.59±0.06	0.61±0.05	0.55±0.04
LVPW;s (mm)	0.95±0.10	0.92±0.10	0.94±0.09	0.86±0.08
LVID;d (mm)	4.43±0.24	4.18±0.22	4.41±0.24	4.13±0.25
LVID;s (mm)	3.24±0.32	2.97±0.29	3.19±0.31	2.99±0.36
LVEDV (μl)	89.3±11.6	78.2±9.8	88.4±11.2	75.8±10.8
LVESV (μl)	42.7±9.8	34.7±8.2	41.1±9.3	35.5±9.9

Mean±SD; repeated three-way ANOVA followed by Tukey's test; *$p<0.05$, **$p<0.01$ vs. male mice with same genotype.

Table 9. Echocardiographic parameters from WT and S14D mice at 4.5m

	WT		S14D/S14D	
	Male	Female	Male	Female
N	20	23	13	17
BW (g)	33.8±4.7	28.8±4.5	34.2±4.8	27.5±3.3*
LV mass (mg)	106.6±15.7	96.2±10.6	106.2±11.6	84.9±9.4**
LV mass/BW (mg/g)	3.19±0.54	3.38±0.42	3.14±0.43	3.11±0.35
HR (bpm)	497±53	498±44	480±62	521±39
EF (%)	52.10±6.49	53.46±6.14	50.81±4.75	54.57±7.21
FS (%)	26.68±4.13	27.46±4.01	25.86±2.93	28.15±4.61
SV (μl)	46.1±4.4	43.7±4.3	48.9±5.4	41.4±4.9
CO (ml/min)	23.0±3.49	21.7±1.93	23.2±3.3	21.6±3.0
LVPW;d (mm)	0.65±0.05	0.62±0.05	0.61±0.06	0.59±0.03
LVPW;s (mm)	0.98±0.09	0.94±0.09	0.95±0.10	0.92±0.08
LVID;d (mm)	4.43±0.27	4.28±0.18	4.58±0.18	4.14±0.20**
LVID;s (mm)	3.26±0.35	3.11±0.27	3.39±0.21	2.98±0.30*
LVEDV (μl)	89.6±12.7	82.3±8.3	96.4±8.8	76.4±8.7**
LVESV (μl)	43.5±10.9	38.6±8.0	47.5±7.1	35.0±8.4**

Mean±SD; repeated three-way ANOVA followed by Tukey's test; *$p<0.05$, **$p<0.01$ vs. male mice with same genotype.

Table 10. Echocardiographic parameters from WT and S14D mice at 6m

	WT		S14D/S14D	
	Male	Female	Male	Female
N	20	23	13	17
BW (g)	37.1±6.4	31.5±6.8	36.5±5.1	29.5±4.0
LV mass (mg)	111.7±16.6	103.7±14.6	107.9±10.0	88.8±9.5**,#
LV mass/BW (mg/g)	3.09±0.73	3.40±0.69	2.99±0.36	3.05±0.40
HR (bpm)	505±51	503±42	497±44	521±50
EF (%)	52.49±5.16	54.67±5.70	54.73±5.56	54.99±7.24
FS (%)	26.93±3.36	28.24±3.73	28.38±3.71	28.50±4.85
SV (μl)	49.7±8.6	45.6±5.6	50.8±6.5	44.4±4.4
CO (ml/min)	24.9±4.0	22.9±3.2	25.1±3.3	23.2±3.7
LVPW;d (mm)	0.65±0.06	0.65±0.08	0.63±0.06	0.60±0.04
LVPW;s (mm)	0.98±0.11	1.00±0.10	1.01±0.08	0.93±0.07
LVID;d (mm)	4.53±0.29	4.31±0.24	4.51±0.18	4.26±0.20
LVID;s (mm)	3.31±0.25	3.09±0.26	3.23±0.22	3.05±0.32
LVEDV (μl)	94.6±13.6	83.8±10.8	92.9±8.5	81.5±9.1
LVESV (μl)	44.9±8.1	38.2±7.5	42.1±6.9	37.1±9.0

Mean±SD; repeated three-way ANOVA followed by Tukey's test; *$p<0.05$, **$p<0.01$ vs. male mice with same genotype; $^{\#}p<0.05$, $^{\#\#}p<0.01$ vs. WT mice of same sex.

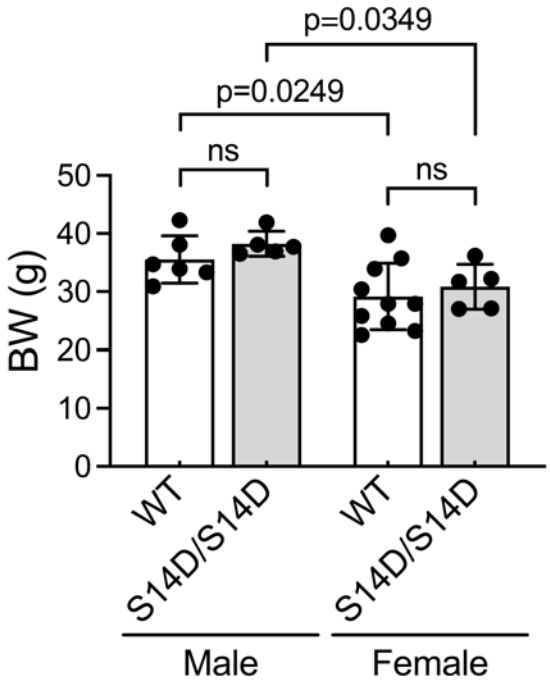

Figure 7. **Body weight of WT and S14D mice.**

Body weight of mice with indicated genotypes at 10m. Each dot represents an individual mouse; mean±SD; two-way ANOVA followed by Tukey's test.

1.2.2. Survival watch for WT and S14D mice

Despite the smaller posterior wall thickness and lower SV observed in S14D female mice than WT females, S14D knock-in appeared not to exert detrimental impact on mouse growth or LV function. We further tracked the survival rate of a cohort of homozygous S14D mice (13 males and 17 females) and their WT littermates (19 males and 20 females) over 273 days. By the time of the last observation, none of them had died or shown gross abnormalities.

These findings demonstrate that genetic mimicry of pS14-Rpn6 by S14D knock-in has little impact on LV functioning for at least the first 6 months or gross phenotypes and mortality for at least the first 10 months. Therefore, our S14A and S14D mice are desirable tools for determining the (patho)physiological significance of pS14-Rpn6.

PART II. Establishing pS14-RPN6 as the Mediating Mechanism for 26S Proteasome Activation by cAMP/PKA

PKA has been shown to activate the proteasomes and enhance the capacity of the cell to degrade short-lived proteins including various pathogenic aggregation-prone proteins by directly phosphorylating Rpn6 at Ser14 in cultured cells.[123,125] Our group also has reported that cAMP elevation increases pS14-Rpn6 in a PKA-dependent manner and improves UPS proteolytic function in cultured cardiomyocytes.[128] Despite compelling *in vitro* evidence, the physiological and pathophysiological significance of pS14-Rpn6 in mediating the activation of 26S proteasomes by cAMP/PKA have never been genetically tested in animals. Our newly created S14A and S14D knock-in mice enable us to fill these critical gaps.

2.1. pS14-Rpn6 and proteasome activation by cAMP/PKA are lost in cultured cells from S14A mice

To determine the role of pS14-Rpn6 in the proteasome activation by cAMP/PKA, we first created MEF cell lines from WT and homozygous S14A mice and tested their responses to the augmentation of cAMP/PKA signaling by forskolin (an adenylate cyclase activator) or piclamilast (a PDE4 inhibitor). WT MEFs treated with vehicle control displayed a detectable level of pS14-Rpn6; both forskolin and piclamilast induced significant increases in pS14-Rpn6 (**Figure 8A, 8B**), with total levels of Rpn6 remaining unchanged (**Figure 8A, 8C**). As a result, the ratio of pS14-Rpn6 to Rpn6 was increased significantly by both treatments (**Figure 8D**). However, pS14-Rpn6 was completely lost in S14A MEFs regardless of the treatments, although similar levels of increases in the phosphorylated forms of other PKA substrates by either treatment were detected in WT and S14A MEFs (**Figure 9**). The 26S proteasome chymotrypsin-like peptidase activity was

discernibly lower in S14A MEFs than in WT MEFs under basal condition ($p<0.005$). Treatment with forskolin or both piclamilast and forskolin led to significant increases in the 26S proteasome peptidase activities in WT MEFs, but such effect was completely lost in S14A MEFs (**Figure 10A, 10B**). In addition, the increase in the 26S proteasome peptidase activity by forskolin in WT MEFs was abolished by co-treatment with a PKA inhibitor H89 (**Figure 10B**).

We also tested the impact of augmentation of cAMP/PKA on proteasome activities in cultured AMCMs. The basal 26S proteasome chymotrypsin-like activity was not significantly lower in S14A AMCMs compared with WT AMCMs ($p=0.505$). Upon forskolin treatment, the proteasome peptidase activity was dramatically elevated in WT AMCMs, which was abolished by H89. In S14A AMCMs, the responses to the treatments were completely lost (**Figure 10C**).

These data validate in cell cultures that pS14-Rpn6 is required for PKA-induced activation of 26S proteasomes.

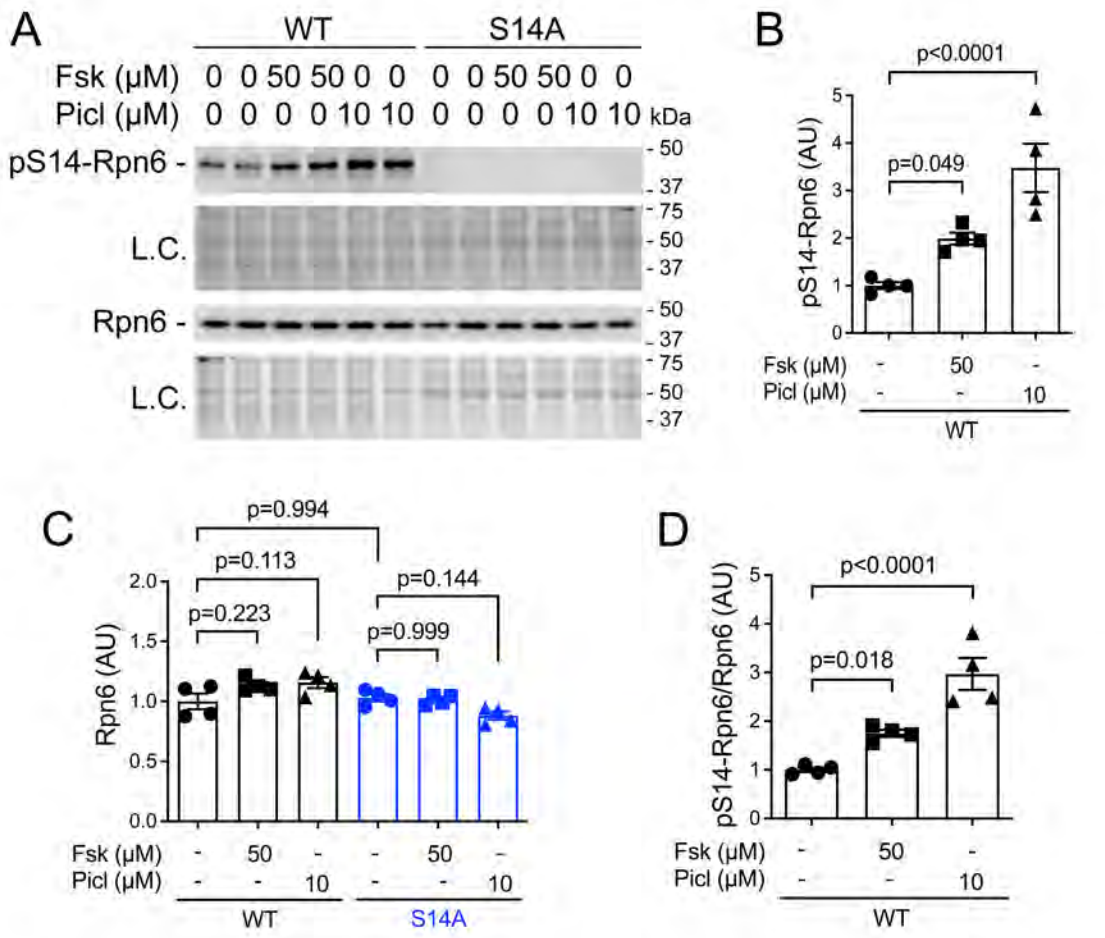

Figure 8. pS14-Rpn6 is lost in cultured cells from S14A mice.

WT and homozygous S14A MEFs in cultures were treated with forskolin (Fsk), piclamilast (Picl), or vehicle control (0.1% DMSO) at the indicated concentration and harvested 3 hours after treatments for crude protein extraction and assays. **A** ~ **D**, Representative images (A) and pooled densitometry data (B, C, D) of Western blots for pS14-Rpn6 (A and B), total Rpn6 (A and C), and ratio of pS14-Rpn6 to Rpn6 (D). L.C., loading control; the in-lane total protein signal from the stain-free image was used to normalize the loading; the same for other figures. Each lane or dot represents a biological repeat; mean±SEM; two-way ANOVA followed by Tukey's test.

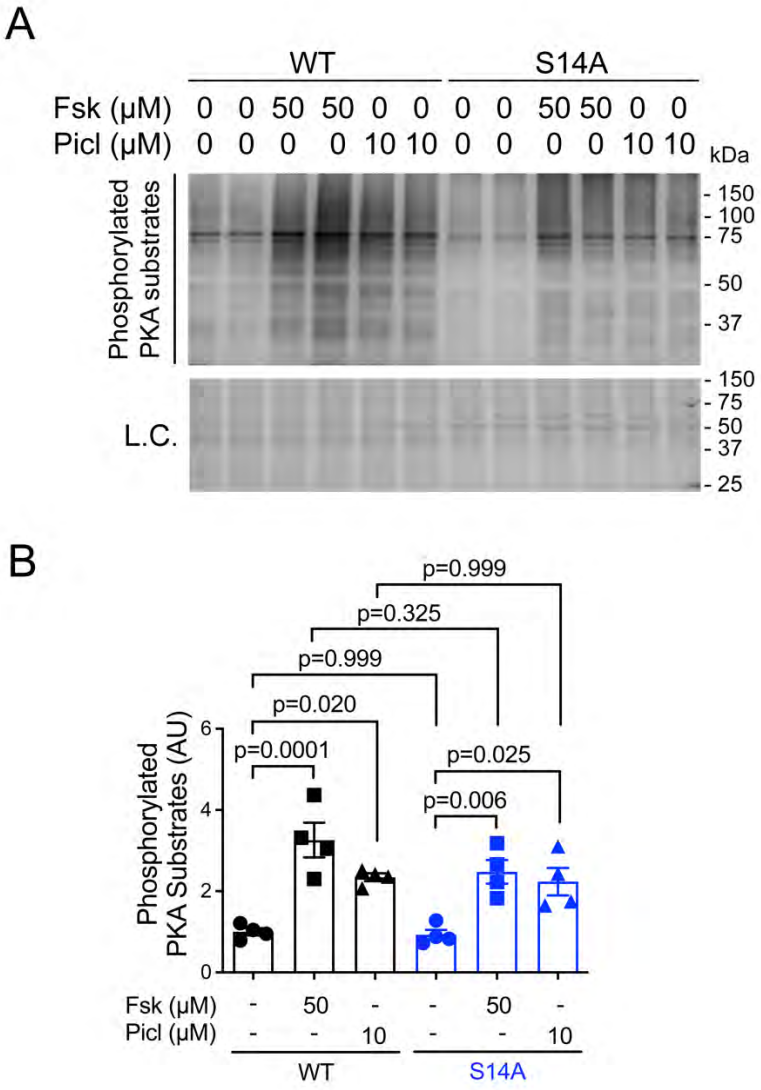

Figure 9. Changes in total phosphorylated PKA substrates in cultured MEFs induced by cAMP/PKA augmentation.

MEFs isolated from WT and homozygous S14A mice were cultured and treated the same way as described in **Figure 8** for crude protein extraction and assays. Shown are representative images (A) and pooled densitometry data (B) of Western blot for total phosphorylated PKA substrates. Each lane or dot represents a biological repeat; mean±SEM; two-way ANOVA followed by Tukey's test.

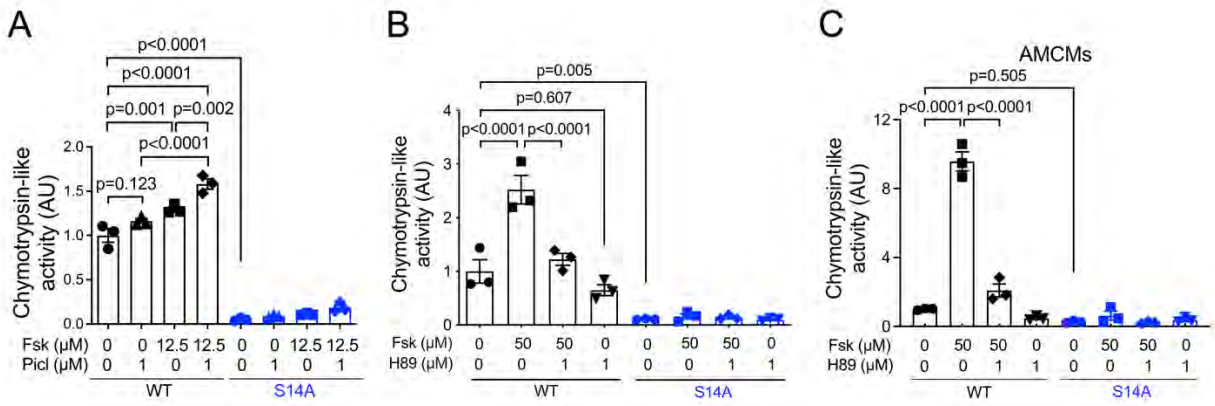

Figure 10. Proteasome activation by cAMP/PKA is lost in cells from S14A mice.

A, 26S proteasome chymotrypsin-like activity assays using crude protein extracts of MEFs from WT or homozygous S14A mice that were cultured and treated with forskolin, piclamilast, or vehicle control at the indicated concentration for 3 hours. **B**, 26S proteasome chymotrypsin-like activity assays using crude protein extracts of MEFs from WT or homozygous S14A mice that were cultured and treated with forskolin, H89, both, or vehicle control for 3 hours. **C**, 26S proteasome chymotrypsin-like activity assays using crude protein extracts of AMCMs from WT or homozygous S14A mice that were cultured and treated with forskolin, H89, both, or vehicle control for 6 hours. Each dot represents a biological repeat; mean±SEM; two-way ANOVA followed by Tukey's test.

2.2. Myocardial pS14-Rpn6 and proteasome activation by cAMP/PKA are lost in S14A mice

We then tested the impact of S14A on cAMP/PKA-induced proteasome activation in mice. As expected, pS14-Rpn6 was not detected in S14A mouse myocardium regardless of forskolin treatment (**Figure 11A, 12A**). By contrast, myocardial pS14-Rpn6 in WT mice treated with forskolin (5 mg/kg) was 2.5 folds of that in WT mice treated with vehicle control and this increase was abolished by pre-treatment of PKA inhibitor H89 (**Figure 11A, 11B**). Myocardial 26S proteasome chymotrypsin-like activities in WT mice treated with forskolin were approximately 3 folds of that in the vehicle control treated WT mice, but this increase was prevented by pre-treatment of H89 (**Figure 11C**). Forskolin increased myocardial pS14-Rpn6 in WT mice in a dose dependent manner but did not affect the total levels of Rpn6 in either WT or S14A mice (**Figure 12A-12D**). Treatment with forskolin at either 5 mg/kg or 10 mg/kg caused no changes in the proteasome peptidase activities in S14A mice (**Figure 11C**), although they induced comparable levels of phosphorylation of other PKA substrates as in WT mice (**Figure 12E, 12F**), indicative of the requirement of pS14-Rpn6 for PKA to activate 26S proteasomes.

The results provide unequivocally the first *in vivo* demonstration that pS14-RPN6 is required for the activation of 26S proteasomes by cAMP/PKA.

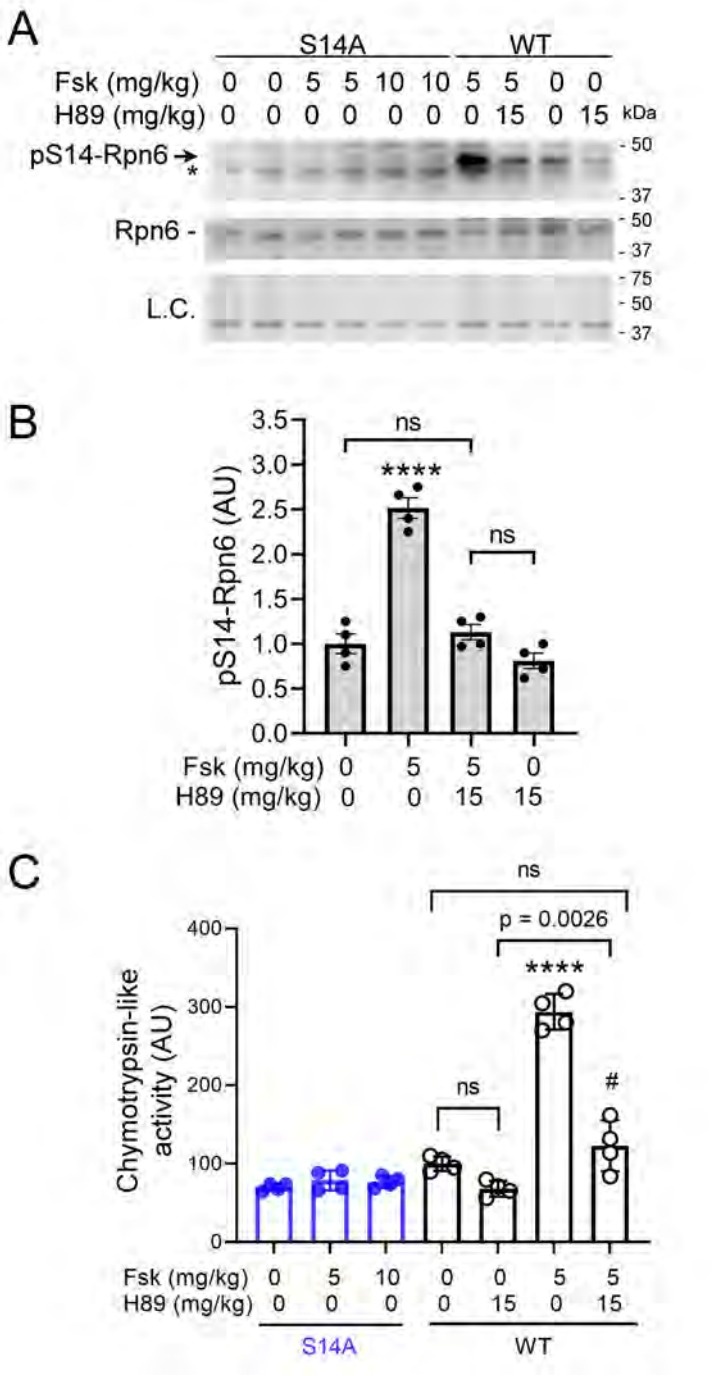

Figure 11. Myocardial pS14-Rpn6 and proteasome activation by cAMP/PKA are lost in S14A mice.

Adult WT and homozygous S14A mice were injected (i.p.) with forskolin, H89, or both and sacrificed 6 hours later to harvest tissues. In the Fsk+H89 group, H89 was injected 15 minutes before forskolin treatment. Total proteins from ventricular myocardium were analyzed. **A** and **B**, Western blot analyses for pS14-Rpn6 (*denotes a nonspecific band) and Rpn6. Shown are representative images from WT and S14A mice (A) and pooled densitometry data from WT mice (B). **C**, Changes in 26S proteasome chymotrypsin-like peptidase activities. Each lane or dot represents an individual mouse (male to female 1:1); mean±SEM; two-way ANOVA followed by Tukey's test. **** $p<0.0001$ vs. all other groups; # $p<0.05$ vs. all S14A groups.

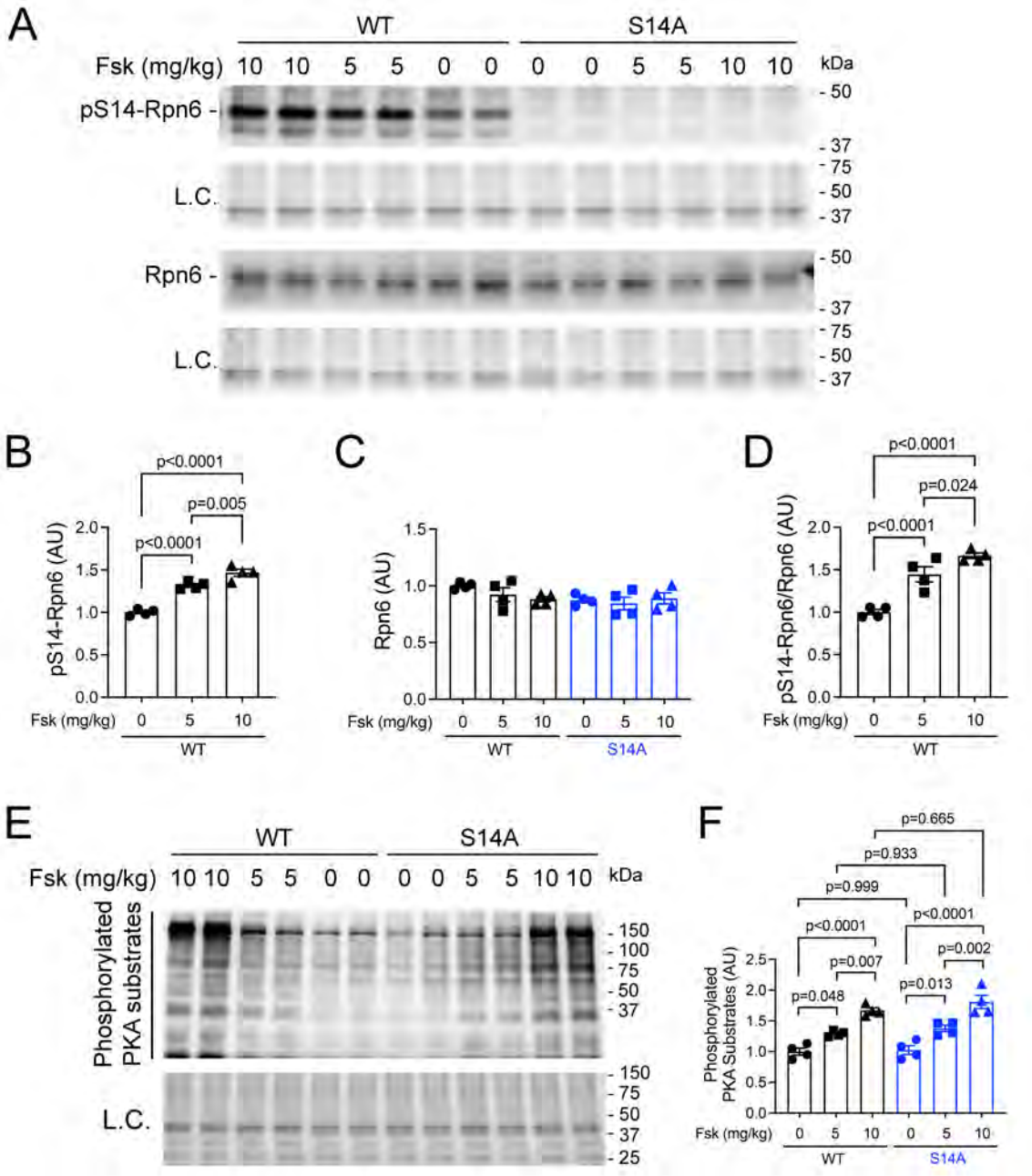

Figure 12. Effects of forskolin on myocardial protein levels of pS14-Rpn6, Rpn6, and total phosphorylated PKA substrates in WT and S14A mice.

Adult WT and homozygous S14A mice were injected (i.p.) with 5 mg/kg or 10 mg/kg forskolin (Fsk) and sacrificed 6 hours later to harvest tissues. Total proteins from ventricular myocardium

were analyzed. **A** ~ **D**, Representative images of Western blot analyses for the indicated proteins (A) and pooled densitometry data for pS14-Rpn6 (B), total Rpn6 (C), and the ratio of pS14-Rpn6 to Rpn6 (D). **E** and **F**, Representative images (E) and pooled densitometry data (F) of Western blot analysis for total phosphorylated PKA substrates. Each lane or dot represents an individual mouse (male to female 1:1); mean±SEM; two-way ANOVA followed by Tukey's test.

2.3. S14A does not appear to alter basal myocardial UPS functioning

Given that S14A blocks PKA-mediated proteasome activation, we determined whether UPS proteolytic function is altered by the S14A knock-in through crossbreeding transgenic GFPdgn, a surrogate UPS substrate, into S14A mice. GFPdgn protein is a green fluorescence protein (GFP) modified by carboxyl fusion of degron CL1 and has been well-established to inversely reflect UPS functional status.[176] We did not observe significant differences in myocardial GFPdgn protein levels among GFPdgn control, S14A/+::GFPdgn, and S14A/S14A::GFPdgn mice at 6~8 weeks of age (**Figure 13**), indicating that S14A does not discernibly alter basal myocardial UPS performance at least at the young age. This is consistent with that myocardial proteasome peptidase activities did not differ significantly between S14A and WT mice at baseline (**Figure 11C**).

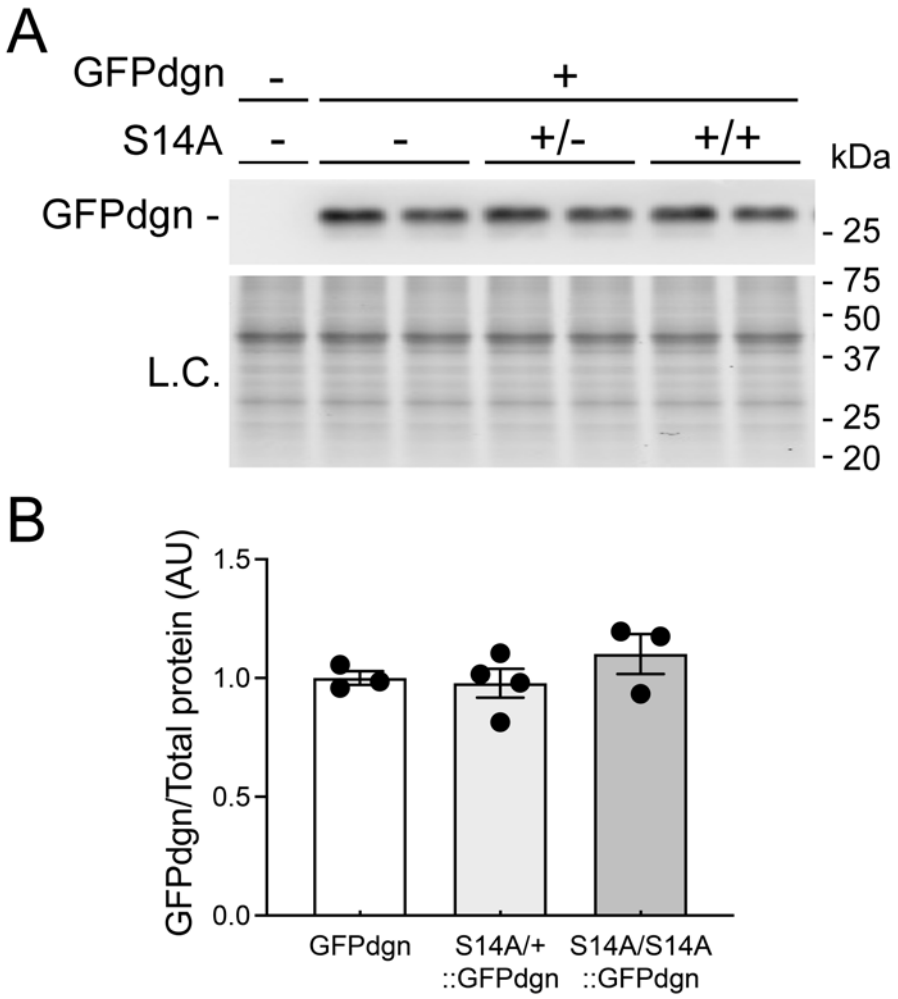

Figure 13. Effect of S14A on mouse myocardial UPS performance.

Tg GFPdgn was cross-bred into S14A mice and sex-matched mice of the resultant genotypes were sacrificed at 6-8 weeks of age to harvest tissues. Shown are representative images (A) and pooled densitometry data (B) of Western blot for GFPdgn. Each lane or dot represents an individual mouse; mean±SEM; one-way ANOVA followed by Tukey's test.

2.4. S14D enhances myocardial UPS performance

We next tested the effect of genetic mimicry of pS14-Rpn6 on the UPS-mediated proteolysis, by crossbreeding tg GFPdgn into S14D mice and examining the steady state protein levels of the surrogate UPS substrate, GFPdgn, in ventricular myocardium. We found that myocardial GFPdgn proteins were significantly lower in heterozygous and homozygous S14D-coupled GFPdgn mice, compared with GFPdgn control mice (**Figure 14A, 14B**), The reduction of GFPdgn protein levels was evident primarily in the cardiomyocyte compartment as revealed by GFPdgn direct fluorescence confocal microscopy (**Figure 14C**). Changes in the abundance of GFPdgn proteins can result from alterations in either protein synthesis or degradation. Hence, we next assessed GFPdgn mRNA levels in total RNA extracted from ventricular myocardium by real-time qPCR. Myocardial GFPdgn mRNA levels were comparable among the three groups (**Figure 14D**), indicating that S14D decreases myocardial GFPdgn proteins via a post-transcriptional mechanism. These data demonstrate that S14D alone can enhance cardiac UPS proteolytic function.

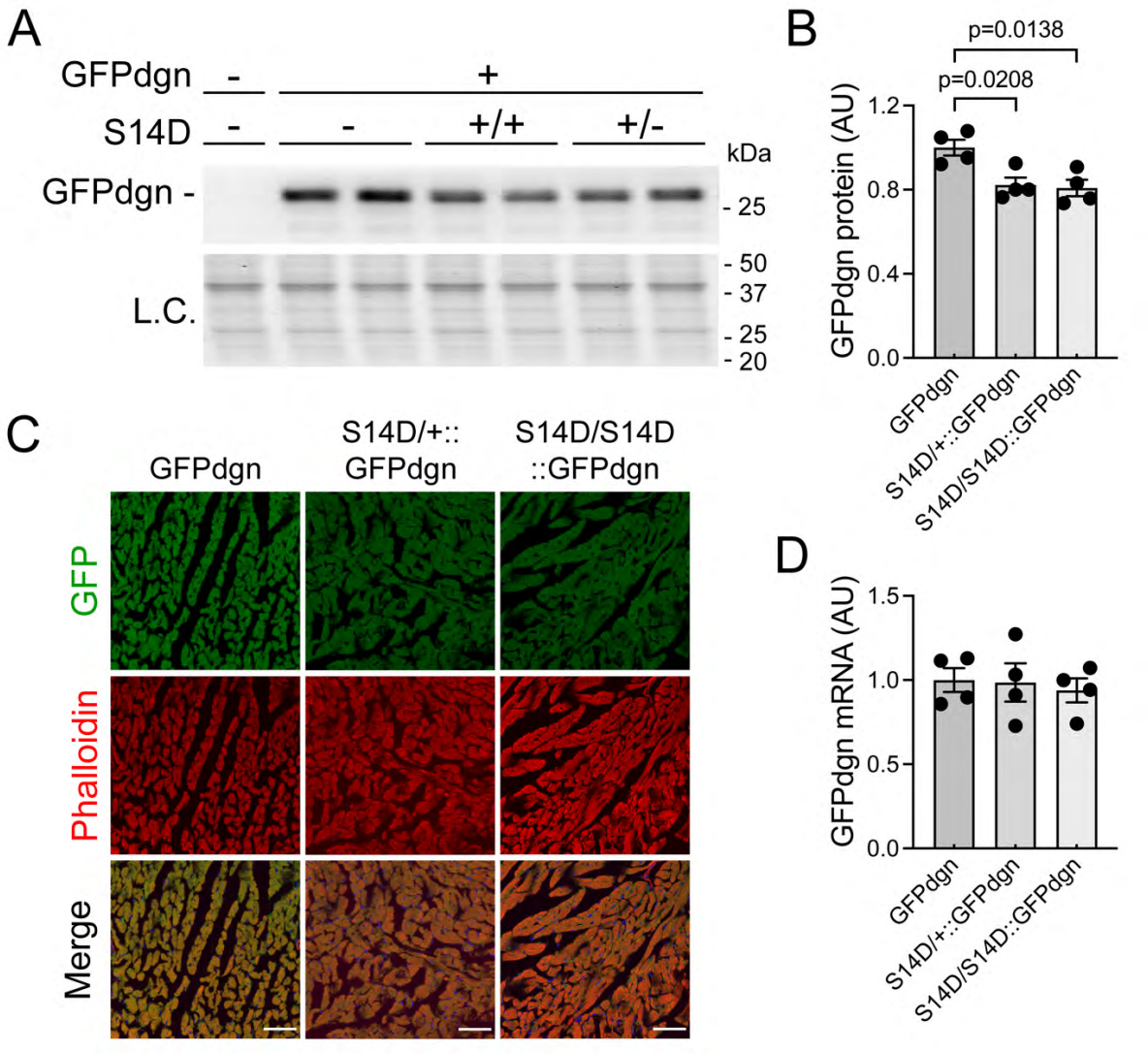

Figure 14. Effect of S14D on mouse myocardial UPS performance.

Tg GFPdgn was cross-bred into S14D mice and the resultant mice were sacrificed at 8 weeks of age. Ventricular myocardium was sampled for protein and RNA extraction or processed for immunofluorescence confocal microscopy. **A** and **B**, Representative images (A) and pooled densitometry data (B) of Western blot for GFPdgn. **C**, Representative confocal micrographs of GFPdgn from direct GFP fluorescence from the indicated groups. Alexa Fluor 568-conjugated Phalloidin was used to stain F-actin to identify cardiomyocytes. Scale bar=50 μm. **D**,

Myocardial GFPdgn mRNA levels were compared with real-time qPCR analyses. Each lane or dot represents an individual mouse (male to female 1:1); mean±SEM; one-way ANOVA followed by Tukey's test.

2.5. Basal 26S proteasome activities are greater in the cardiomyocytes and myocardium from adult S14D mice

We have shown that phosphorylation of Ser14-Rpn6 by PKA increases the proteasome activity and S14D can improve the UPS performance. Earlier study also reported that the proteasome activity was enhanced in the non-cardiac cells transfected with S14D plasmids.[123] Hence, we next sought to determine whether the complete replacement of endogenous Rpn6 with S14D would directly affect 26S proteasome activities. In cultured adult cardiomyocytes, the basal proteasome chymotrypsin-like activity was significantly higher in S14D AMCMs (p=0.014) compared with WT AMCMs (**Figure 15A**). The elevation in proteasome peptidase activity by forskolin disappeared due to S14D mutation, further supporting the requirement of pS14-Rpn6 for cAMP/PKA-mediated proteasome activation (**Figure 15A**).

In addition, we found that myocardial chymotrypsin-like, trypsin-like and caspase-like 26S proteasome activities were all increased by ~75%, ~50% and ~40% respectively in homozygous S14D mice (p=0.005, 0.018 and 0.024, respectively), and increased by ~40%, ~40% and ~25% respectively in heterozygous S14D mice (p=0.116, 0.041 and 0.127) compared with that in WT mice (**Figure 15B**), indicating that S14D is capable of increasing all three types of proteasome peptidase activities at baseline in mice.

These results establish compellingly that S14D is enough to increase myocardial proteasome activities and enhance cardiac UPS performance. Since we have demonstrated that pS14-Rpn6 is required for PKA-induced proteasome activation (**Figure 8-12**), these findings from S14D cells and mice provide unequivocal evidence that pS14-Rpn6 is responsible for proteasome activation by cAMP/PKA.

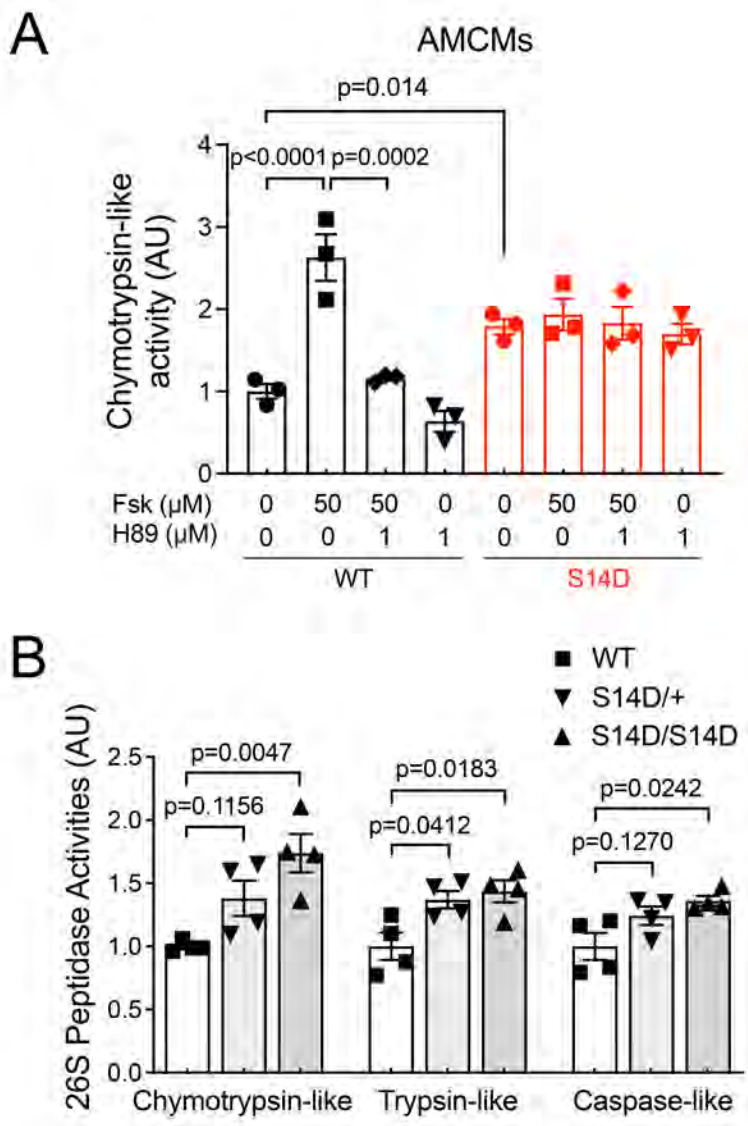

Figure 15. Effect of S14D on mouse cardiomyocyte and myocardial 26S proteasome peptidase activities.

A, 26S proteasome chymotrypsin-like activity assays using crude protein extracts of AMCMs from WT or homozygous S14D mice that were cultured and treated with forskolin, H89, both, or vehicle control for 6 hours. Each dot represents a biological repeat; mean±SEM; two-way ANOVA followed by Tukey's test. **B**, Myocardial 26S proteasome peptidase assays. Crude protein extracts from ventricular myocardium of adult mice of the indicated genotypes were

used. Each dot represents an individual mouse (male to female 1:1); mean±SEM; one-way ANOVA followed by Tukey's test.

PART III. The Pathogenic Significance of pS14-RPN6 Dysregulation in Cardiac Proteinopathy

The findings detailed above have established the responsibility of pS14-RPN6 for the activation of 26S proteasomes by PKA, while its pathophysiological significance remains undefined. Since PFI is a major pathogenic factor cardiac proteinopathy,[77,107,108] we sought to investigate the myocardial status and the role of pS14-RPN6 in the progression of cardiac proteinopathy. The R120G mice are a well-established model of cardiac proteinopathy, which start to develop concentric cardiac hypertrophy at 3m and progress to heart failure by 6m.[107] Therefore, the R120G mice serve as an excellent disease model to evaluate the pathogenesis and disease progression of cardiac IPTS. Hence, in this section, we have evaluated: (1) the basal role of pS14-Rpn6 in the pathogenesis of CryAB^{R120G}-based proteinopathy; (2) the effects of increasing pS14-Rpn6 on the proteasomal degradation of misfolded proteins and disease progression in R120G mice.

3.1. Changes in myocardial pS14-Rpn6 during the progression of CryAB^{R120G}-based cardiac proteinopathy

To determine basal role of pS14-Rpn6 in CryAB^{R120G}-based cardiac proteinopathy, we crossbred S14A into R120G mice and examined the basal status of myocardial pS14-Rpn6 in WT, R120G, and homozygous S14A-coupled R120G mice at different stages of cardiomyopathy. To our surprise, pS14-Rpn6 was markedly decreased in R120G mice compared with WT mice at both 3m and 6m (**Figure 16A-16C**). Homozygous S14A mice were used as a negative control to help accurately identify pS14-Rpn6. At both ages, Rpn6 protein levels were comparable between R120G and S14A-coupled R120G mice, but both were significantly greater than that in WT mice

(**Figure 16A, 16B, 16D**). As a result, the ratios of pS14-Rpn6 to Rpn6 were markedly lower in R120G mice than that in WT mice (**Figure 16E**), which indicate that basal levels of pS14-Rpn6 are significantly decreased in R120G mice during the disease progression. Interestingly, total phosphorylated PKA substrates were decreased at 3m but increased at 6m in R120G mice compared with littermate non-tg controls (**Figure 17**), indicating that the decrease in the pS14-Rpn6 in R120G mice at 6m, at least, is selective. These results imply that pS14-Rpn6 is not part of the natural compensatory response but rather contributes to insufficiency.

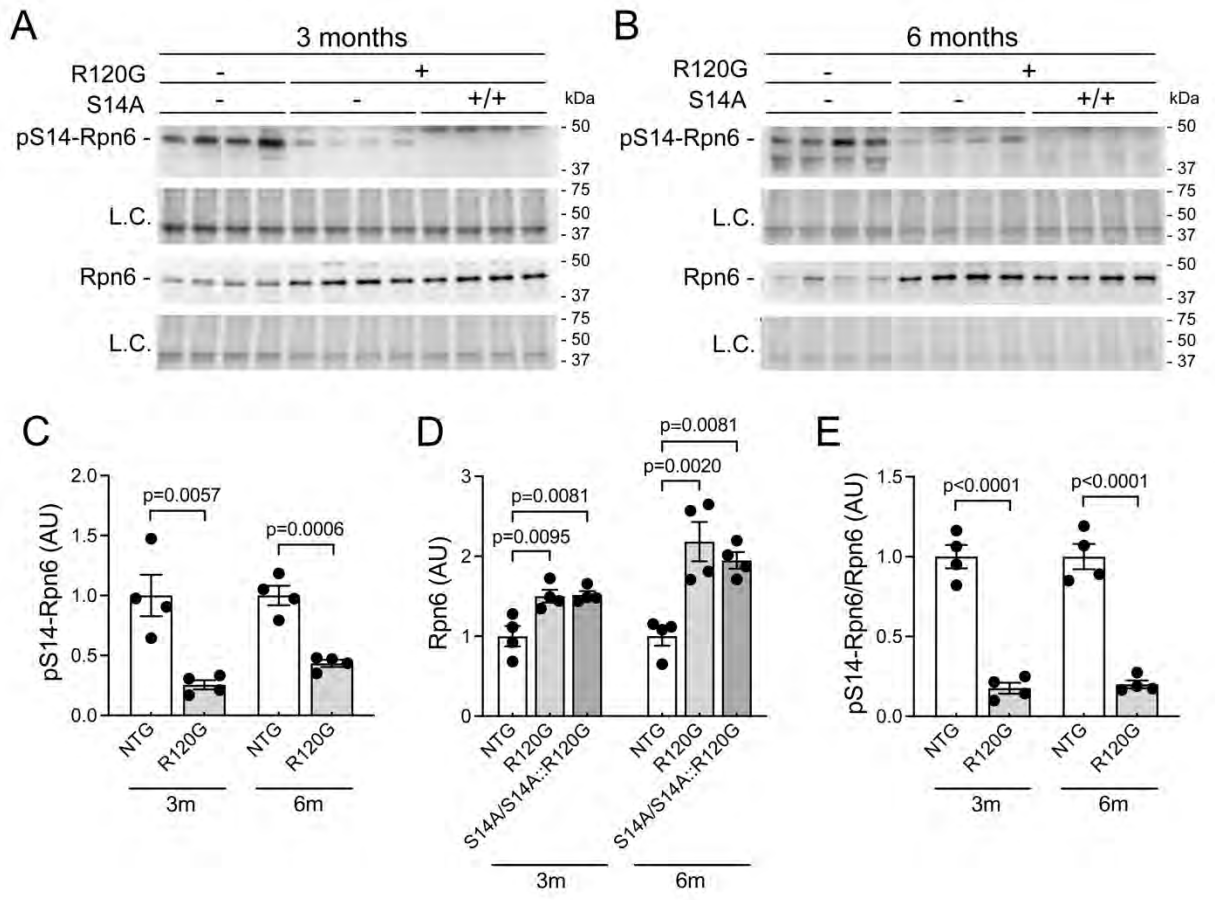

Figure 16. Changes in myocardial total and Ser14-phosphorylated Rpn6 in R120G mice. S14A was cross-bred into R120G mice. Adult WT, R120G, and homozygous S14A-coupled R120G mice were sacrificed at 3m or 6m. Crude protein extracts from ventricular myocardium were used. Shown are representative images (A, B) and pooled densitometry data (C ~ E) of Western blots for pS14-Rpn6 and Rpn6. Homozygous S14A mice were used as the negative control for accurate identification of the pS14-Rpn6 band. Each lane or dot represents an individual mouse (male to female 1:1); mean±SEM; unpaired Student's *t* test for (C, E) and one-way ANOVA followed by Tukey's test for (D).

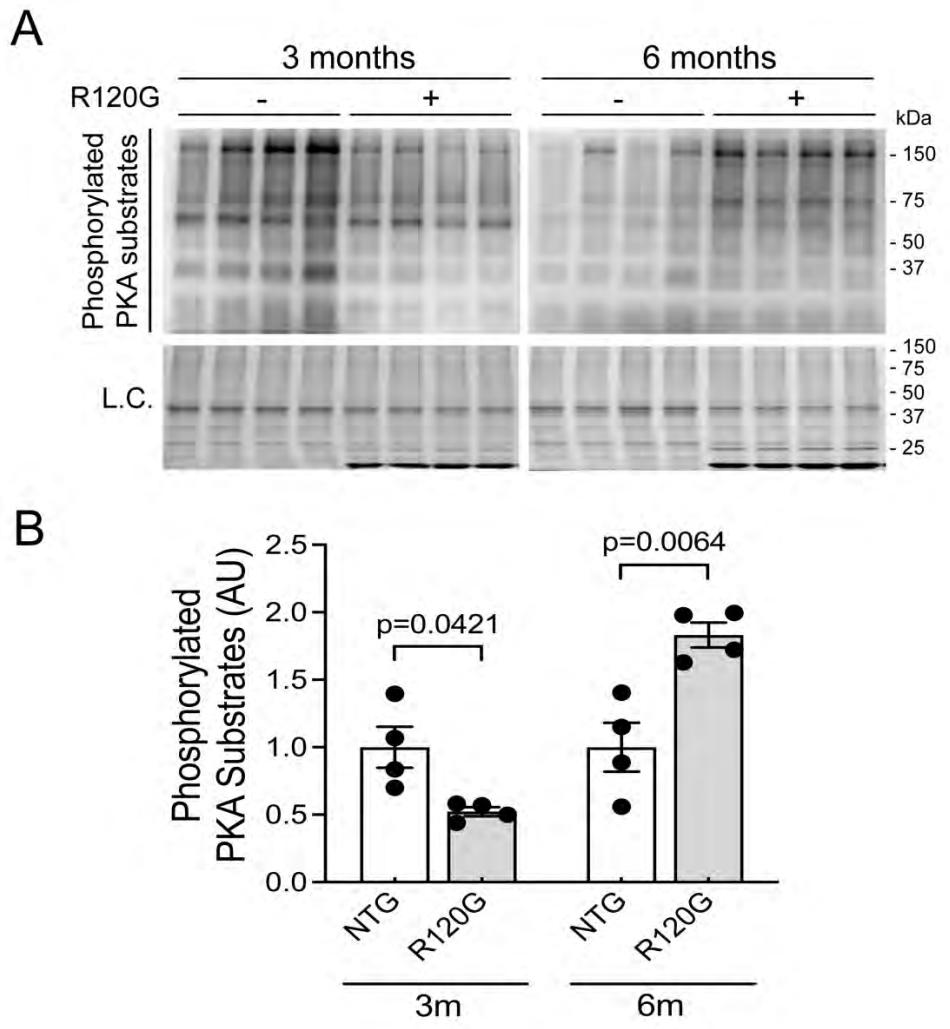

Figure 17. Changes in myocardial total phosphorylated PKA substrates in R120G mice.

WT, R120G, and homozygous S14A-coupled R120G mice were sacrificed at 3m or 6m of age. Crude protein extracts from ventricular myocardium were used. Shown are representative images (A) and pooled densitometry data (B) of Western blots for total phosphorylated PKA substrates. Each lane or dot represents an individual mouse (male to female 1:1); mean±SEM; unpaired Student's *t* test.

3.2. The effects of genetic blockade of pS14-Rpn6 on cardiac proteinopathy

3.2.1. The effects of S14A on the disease progression of R120G mice

We performed serial echocardiography on the mice resulted from crossbreeding of S14A and R120G mice. Consistent with dramatically decreased pS14-Rpn6, the echocardiographic measurements revealed that neither heterozygous nor homozygous S14A exerted discernible effects on cardiac morphometry or function of the R120G mice (**Figure 18**). Therefore, S14A-coupled R120G mice displayed a lifespan comparable to that of R120G control mice, which is true in both males and females (**Figure 19**).

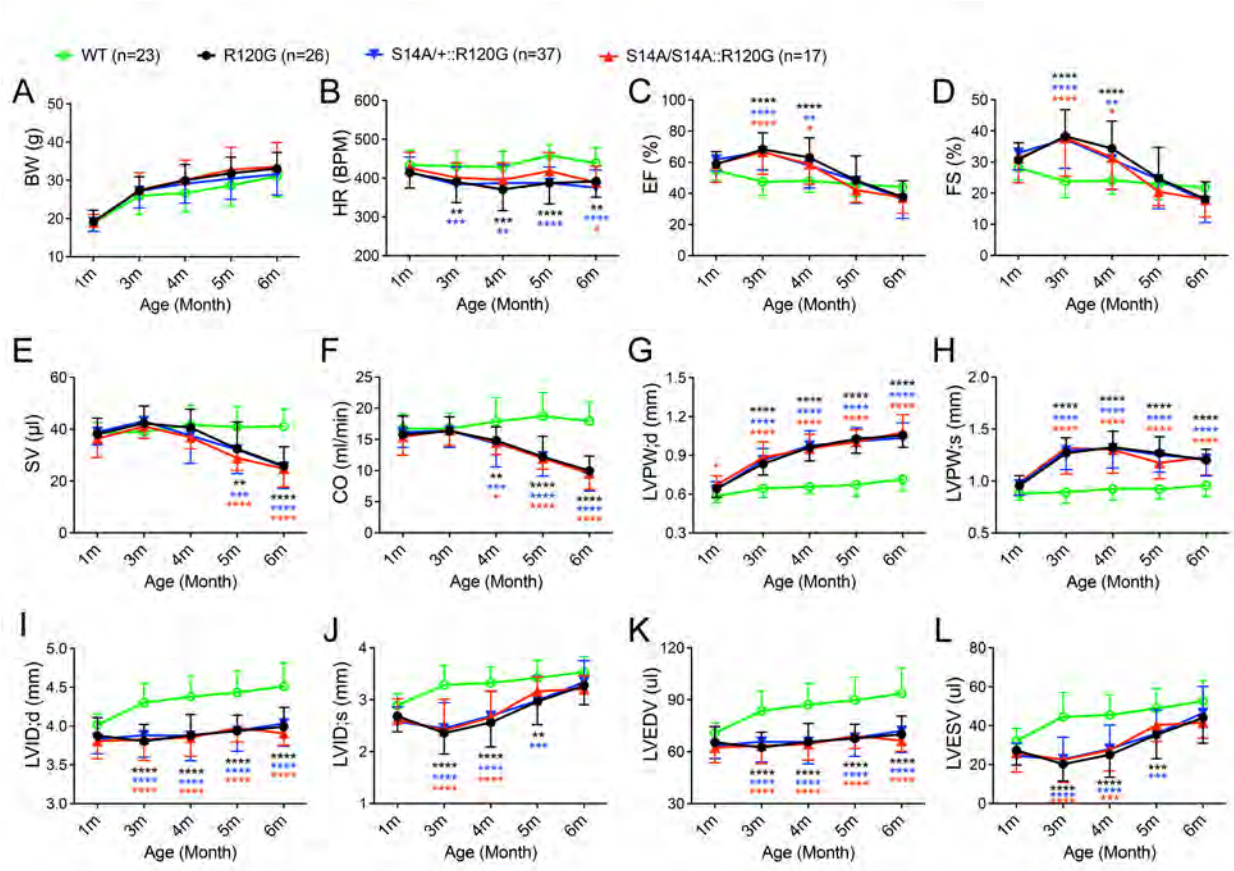

Figure 18. S14A did not exacerbate the progression of R120G-induced cardiac proteinopathy.

Littermate mice of indicated genotypes were subjected to serial echocardiography at 1, 3, 4, 5, and 6 months. The stacked line chart of each panel summarizes the time course of changes in the indicated LV parameters derived from the serial echocardiography. Mean±SD; two-way repeated measures ANOVA followed by Tukey's test; no significant differences in any parameters among R120G, S14A/+::R120G, and S14A/S14A::R120G groups; * in black denotes R120G vs. WT group; * in blue denotes S14A/+::R120G vs. WT group; * in red denotes S14A/S14A::R120G vs. WT group; *p<0.05, **p<0.01, ***p<0.001, ****p<0.0001.

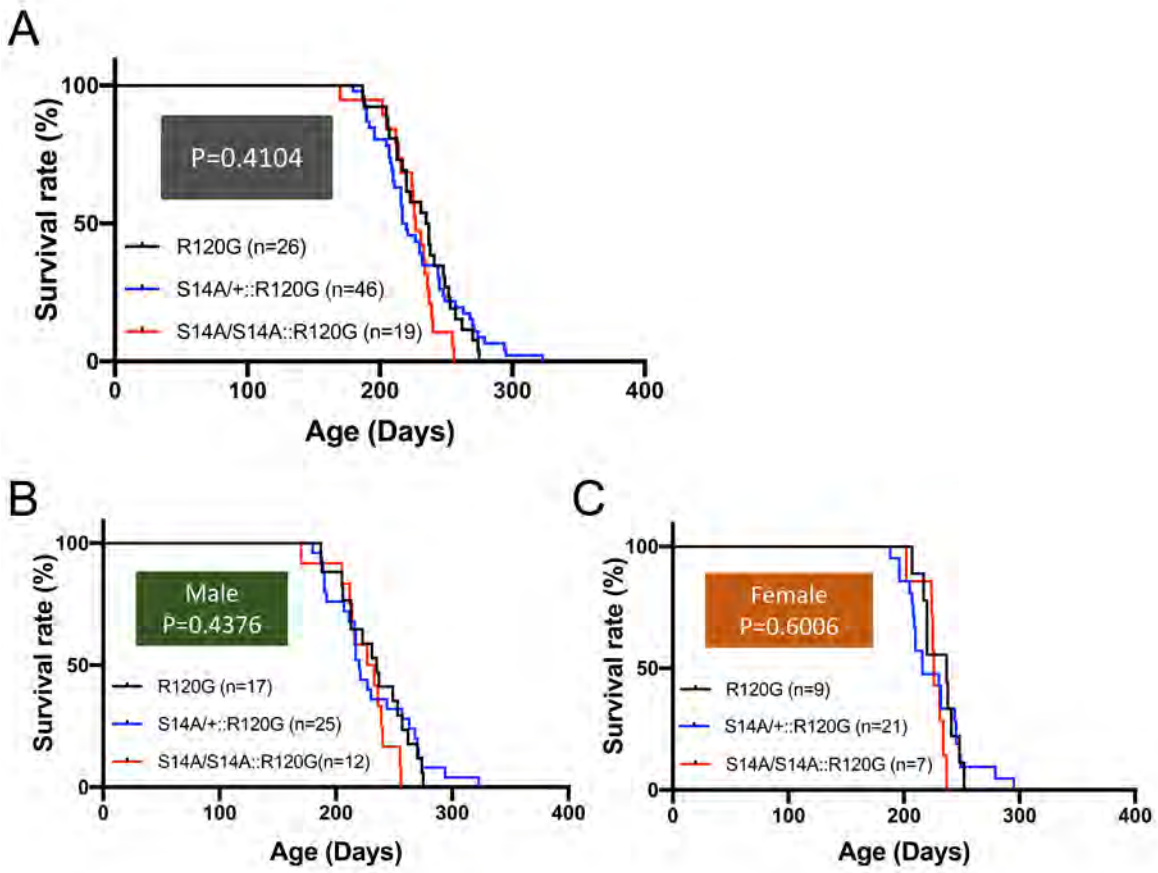

Figure 19. **Kaplan-Meier survival analysis for R120G and S14A-coupled R120G mice.** Shown are Kaplan-Meier survival curves for combined sex (A), male (B), and female (C). When males and females are combined, the median life spans of R120G, S14A/+::R120G, and S14A/S14A::R120G mice are 236, 218.5 and 227 days, respectively; for males, the median life spans are 235, 220 and 230 days, respectively; for females, the median life spans are 237, 216 and 226 days, respectively. Log-rank test.

3.2.2. The effects of S14A on the levels of myocardial pathogenic protein and ubiquitin conjugates in R120G mice

Even though blockade of pS14-Rpn6 did not exert discernible effects on cardiac dysfunction or the survival rate of R120G mice, it could cause changes at the molecular level. Specifically, we intended to determine whether blocking pS14-Rpn6 influences the proteasomal degradation of misfolded proteins.

As shown in **Figure 20**, the accumulation of myocardial CryAB proteins in R120G mice was not affected by S14A at either 3m or 6m. Aberrant protein aggregation induced by overexpression of $CryAB^{R120G}$ impairs UPS proteolytic function in the heart, resulting in elevated levels of ubiquitin conjugates.[77] Consistent with the comparable levels of misfolded protein, S14A did not further increase the accumulation of total or K48-linked ubiquitin conjugates in R120G mice.

These data together with echocardiographic measurements suggest that myocardial pS14-Rpn6 in the R120G mice is so diminished that loss of the residual pS14-Rpn6 does not discernibly alter their proteinopathy progression or UPS-mediated misfolded degradation.

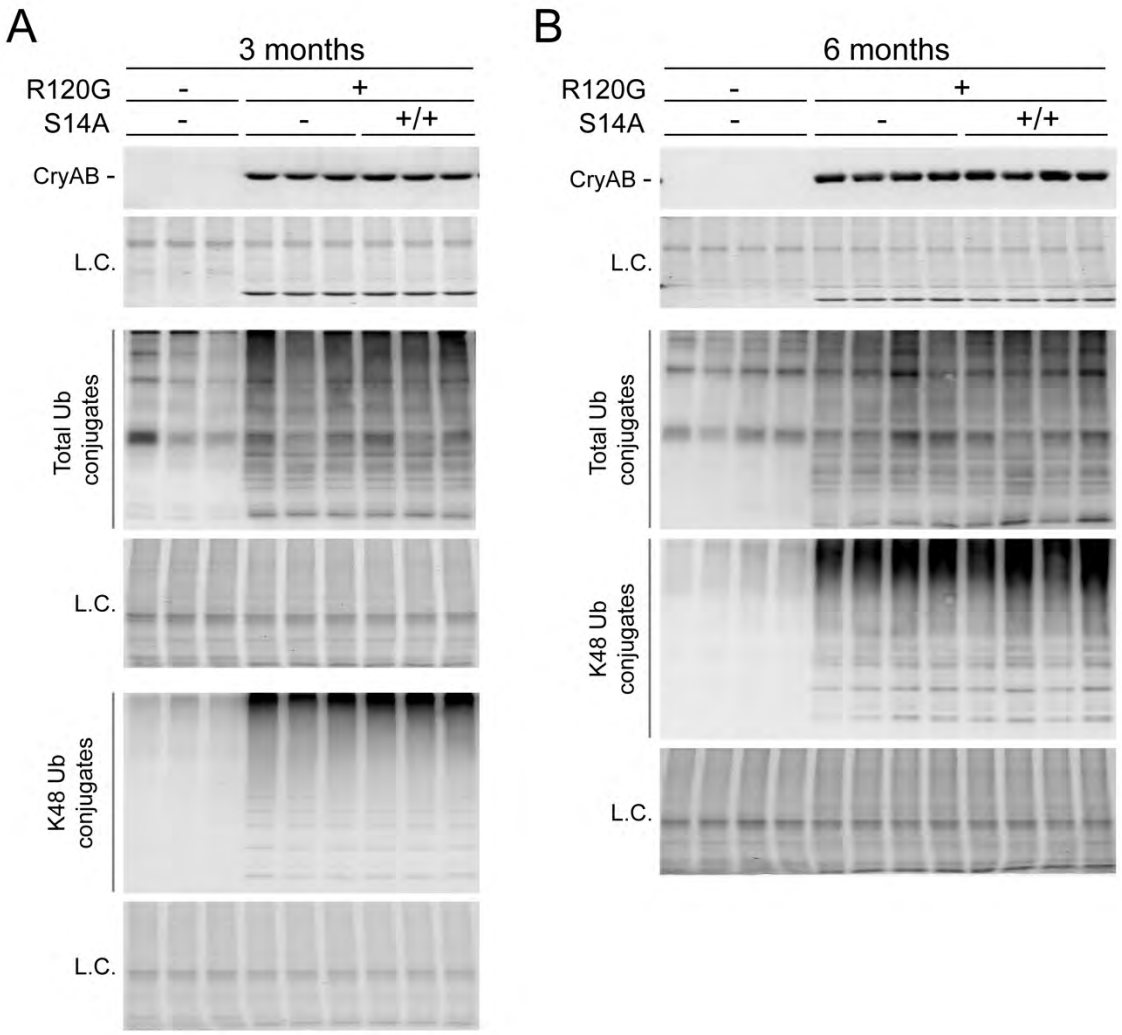

Figure 20. S14A did not alter the levels of myocardial misfolded proteins or ubiquitin conjugates in R120G mice.

Adult WT, R120G, and homozygous S14A-coupled R120G mice were sacrificed at 3m or 6m. Crude protein extracts from ventricular myocardium were used. Shown are representative images of Western blots for CryAB, and total and K48-linked ubiquitin conjugates at 3m (A) and 6m (B). Each lane represents an individual mouse.

3.2.3. The effect of S14A on proteasome assembly

Although genetic blockade of pS14-Rpn6 appears to exert little, if any, impact on UPS proteolytic function and cardiac disease progression in R120G mice, we were still curious about if it would have any effects on proteasome assembly both at baseline and in $CryAB^{R120G}$-based proteinopathy. Using native gel electrophoresis followed by immunoblotting for a representative 20S subunit (β5) or of 19S subunit (Rpt2), we found that S14A and WT mice displayed comparable levels of assembled 30S (double-capped; 19S-20S-19S), 26S (single-capped; 19S-20S), 20S, and 19S proteasomes at both 3m and 6m (**Figure 21**). Compared with WT mice, R120G mice displayed modest, not significant though, increases in 30S proteasomes at both 3m and 6m and in 26S proteasomes at 6m. When coupled with R120G mice, S14A did not seem to affect the levels of 26S and 20S proteasomes at either age, either. Interestingly, compared with R120G mice, S14A-coupled R120G mice displayed markedly attenuated myocardial 19S proteasomes, which seemed to be associated with a modest increase in 30S proteasomes at 3m (**Figure 21**), suggesting that more 19S proteasomes seem to be assembled into the 30S proteasomes to compensate for the loss of pS14-Rpn6, which might explain the findings that complete blockade of pS14-Rpn6 showed no impact on the UPS-mediated removal of misfolded protein or cardiac dysfunction of R120G mice.

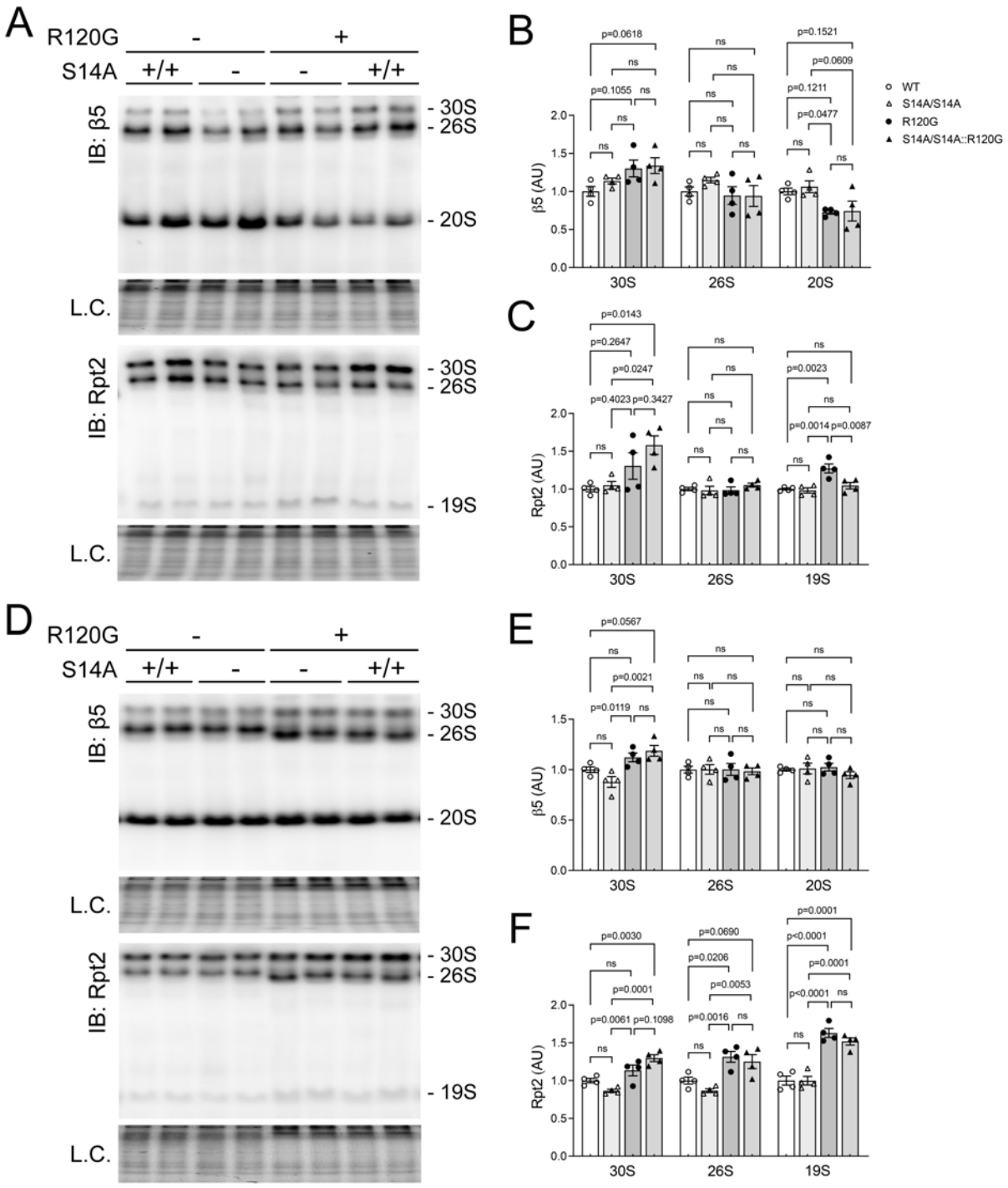

Figure 21. **Effect of S14A on proteasome assembly.**

Crude native protein extracts from ventricular myocardium of WT, S14A/S14A, R120G, and S14A/S14A::R120G littermate mice were fractionated with native gel electrophoresis followed

by immunoblot. **A** ~ **C**, Representative images (A) and pooled densitometry data of immunoblots for β5 (B) and Rpt2 (C) in mice at 3m. **D** ~ **F**, Representative images (D) and pooled densitometry data of immunoblots for β5 (E) and Rpt2 (F) in mice at 6m. IB, immunoblot; Each lane or dot represents an individual mouse (male to female 1:1); mean±SEM; two-way ANOVA followed by Tukey's test.

3.3. The effect of genetic mimicry of pS14-Rpn6 on cardiac proteotoxicity

The discoveries described above indicate that pS14-Rpn6 is selectively diminished during the progression of CryAB^{R120G}-induced cardiac proteinopathy, which may contribute to the insufficiency of misfolded protein elimination in R120G mice. To further determine the pathogenic role of the pS14-Rpn6 impairment, we decided to test the effects of increasing pS14-Rpn6 on R120G mice. We have demonstrated that genetic mimicry of pS14-Rpn6 suffices to increase 26S proteasome activities and enhance UPS-mediated proteolysis. Hence, in this section, we intended to determine whether genetic mimicry of pS14-Rpn6 can reduce aberrant protein aggregation, attenuate cardiac proteotoxicity, and slow down the disease progression in the R120G mice.

3.3.1. S14D increases myocardial proteasome activities and decreases the steady-state levels of misfolded proteins in R120G mice

We first tested whether S14D could enhance proteasome functioning and promote the removal of pathogenic CryAB^{R120G} proteins in R120G mouse hearts. By crossbreeding S14D into R120G mice, we first examined myocardial proteasome peptidase activities in the resultant WT, S14D/S14D, R120G, and S14D/S14D::R120G littermates. R120G mice at 1m displayed significantly higher chymotrypsin-like and caspase-like proteasome activities and a modest but not statistically significant higher trypsin-like activity than WT mice, consistent with a prior report.[186] Importantly, S14D further increased proteasomal chymotrypsin-like, trypsin-like and caspase-like peptidase activities in R120G mice by ~30%, ~40% and ~30%, respectively (**Figure 22A**). Consistently, all three types of proteasomal peptidase activities were significantly elevated in R120G myocardium compared with WT mice and further increased in S14D-coupled R120G mice

at 3m (**Figure 22B**). These data indicate that genetic mimicry of pS14-Rpn6 constitutively increases myocardial proteasome activities in mice both at baseline and during proteotoxic stress.

By 6m, R120G mice have developed heart failure, which inevitably leads to various secondary cellular dysfunctions that could affect proteasome peptidase activities. As such, measuring the latter may not accurately reflect the direct effect of S14D on the proteasome. Thus, we elected to examine the accumulation of misfolded protein aggregates and ubiquitinated proteins. The steady-state levels of myocardial CryAB protein were markedly lower in S14D/S14D::R120G mice compared with R120G control mice at 6m (**Figure 23A, 23B**), without discernible differences in $CryAB^{R120G}$ mRNA levels (p=0.7734, **Figure 23C**). Misfolded proteins undergo aberrant aggregation, forming intermediate oligomers that are highly toxic to the cells. A recently developed method distinguished the degradation of misfolding-prone proteins from other cellular mechanisms regulating protein levels.[184] Total protein lysate was further fractionated into NP-40 soluble (NS, supernatant) and NP-40 insoluble (NI, pellet) portions. The NI pellets were suspended and dissolved in an SDS-containing buffer. NI fractions of misfolding-prone proteins were eliminated rapidly, which can be reversed by proteasome inhibition, indicating that they are readily degraded by the proteasome.[184] Therefore, the changes in the steady-state level of misfolding-prone protein in the NS and NI fractions can inversely reflect proteasome proteolytic activities. Thus, we examined CryAB abundance in NS and NI (misfolded CryAB oligomers) fractions of myocardial proteins, and found that the protein levels of CryAB in both NS and NI fractions of S14D/S14D::R120G mice were markedly lower than those of the littermate R120G control mice (**Figure 23D-23F**), indicating that degradation of misfolded CryAB by the proteasome in R120G hearts is significantly improved by S14D. S14D/S14D mice showed comparable levels of total and K48-linked ubiquitin conjugates compared with WT mice (**Figure 24**). Both myocardial total and

K48-linked ubiquitin conjugates were significantly increased in R120G mice at 6m, and the increase was effectively attenuated when R120G was coupled with S14D (**Figure 24**).

Taken together, these findings compellingly support the conclusion that genetic mimicry of pS14-Rpn6 increases proteasome proteolytic activity, thereby facilitates the removal of misfolded proteins, and reduces aberrant protein aggregation in the heart, a key pathological process in disease with IPTS.

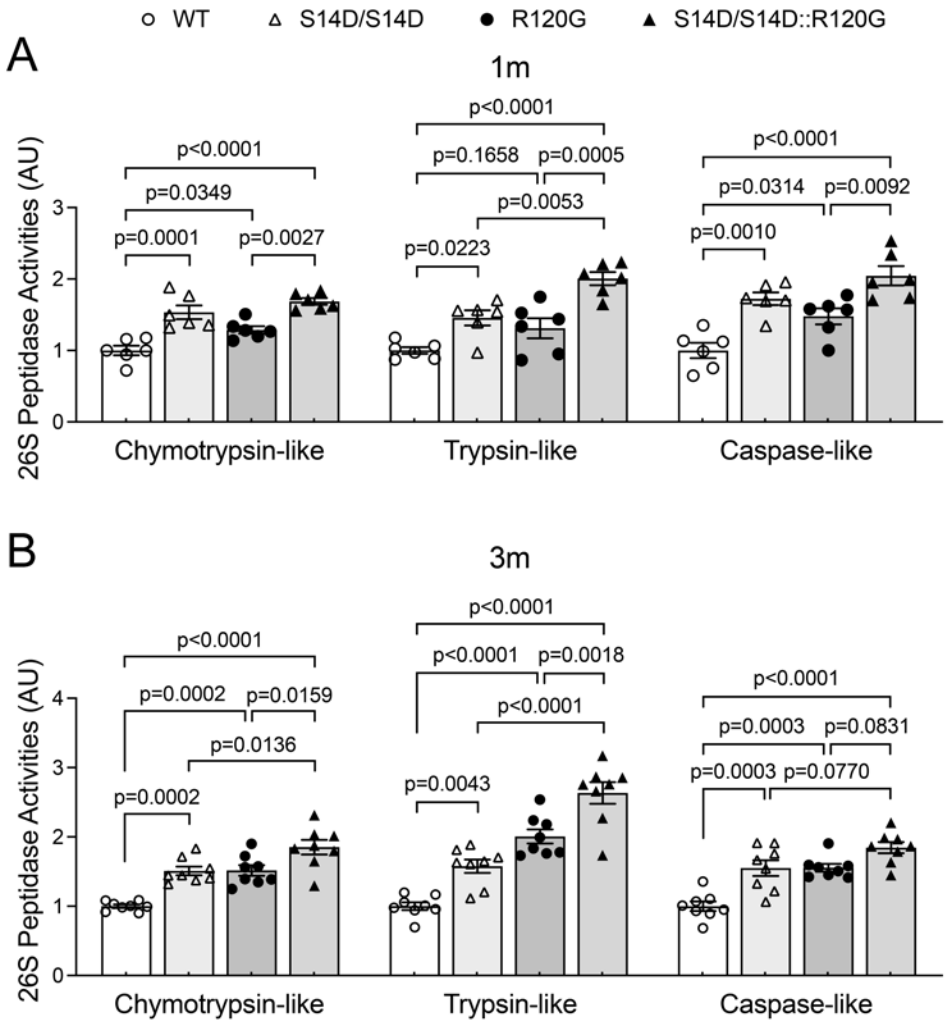

Figure 22. Effect of S14D on myocardial 26S proteasome activities in R120G mice.

S14D was cross bred into R120G mice. **A** and **B**, 26S proteasome peptidase activity assays at 1m (A) and 3m (B). Crude protein extracts from ventricular myocardium of WT, homozygous S14D, R120G, and S14D/S14D::R120G littermate mice were used. Each dot represents an individual mouse (male to female 1:1); mean±SEM; two-way ANOVA followed by Tukey's test.

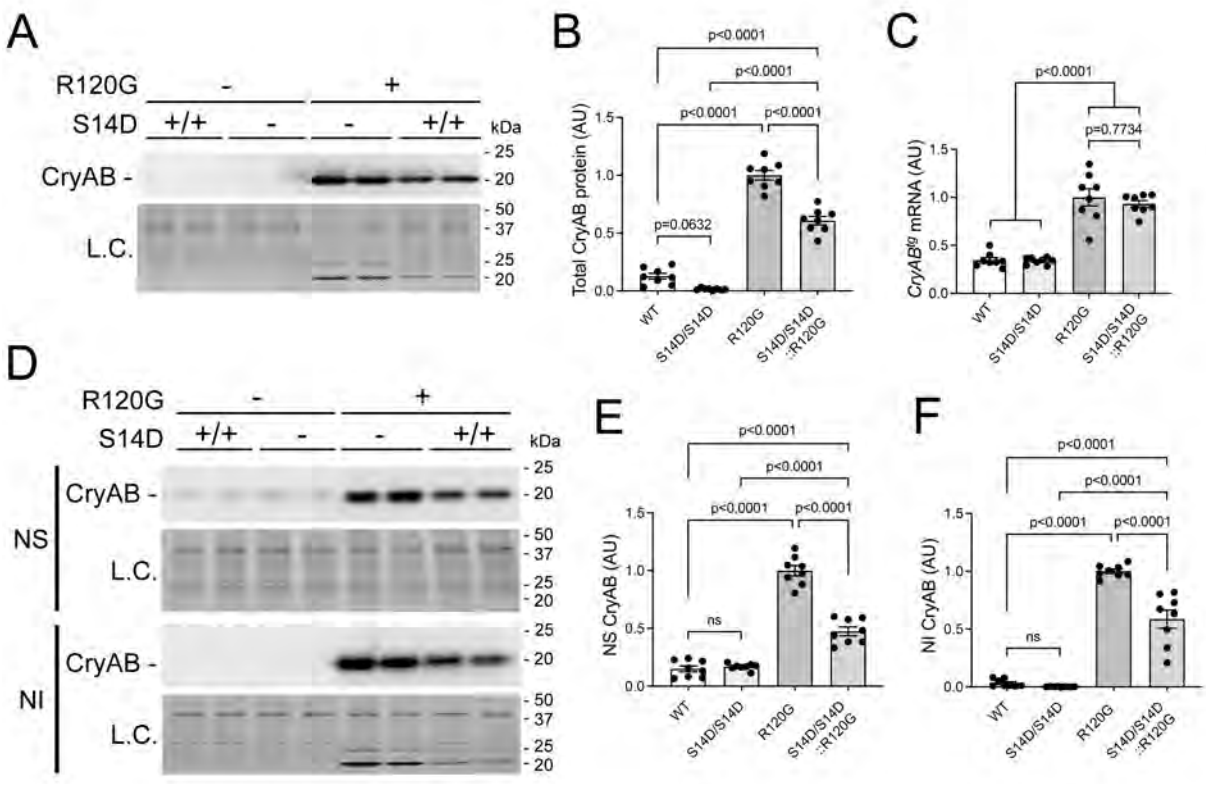

Figure 23. Effect of S14D on the abundance of CryAB proteins in R120G mouse hearts. Littermate WT, S14D/S14D, R120G, and S14D/S14D::R120G mice were sacrificed at 6m. Proteins and RNAs from ventricular myocardium were analyzed. **A** and **B**, Representative images (A) and pooled densitometry data (B) of Western blots for CryAB in the total protein. **C**, Tg CryAB mRNA levels were assessed using real-time qPCR. **D** ~ **F**, Representative images (D) and pooled densitometry data of Western blots for CryAB in the NS (E) and NI (F) protein fractions. Each lane or dot represents an individual mouse (male to female 1:1); mean±SEM; two-way ANOVA followed by Tukey's test.

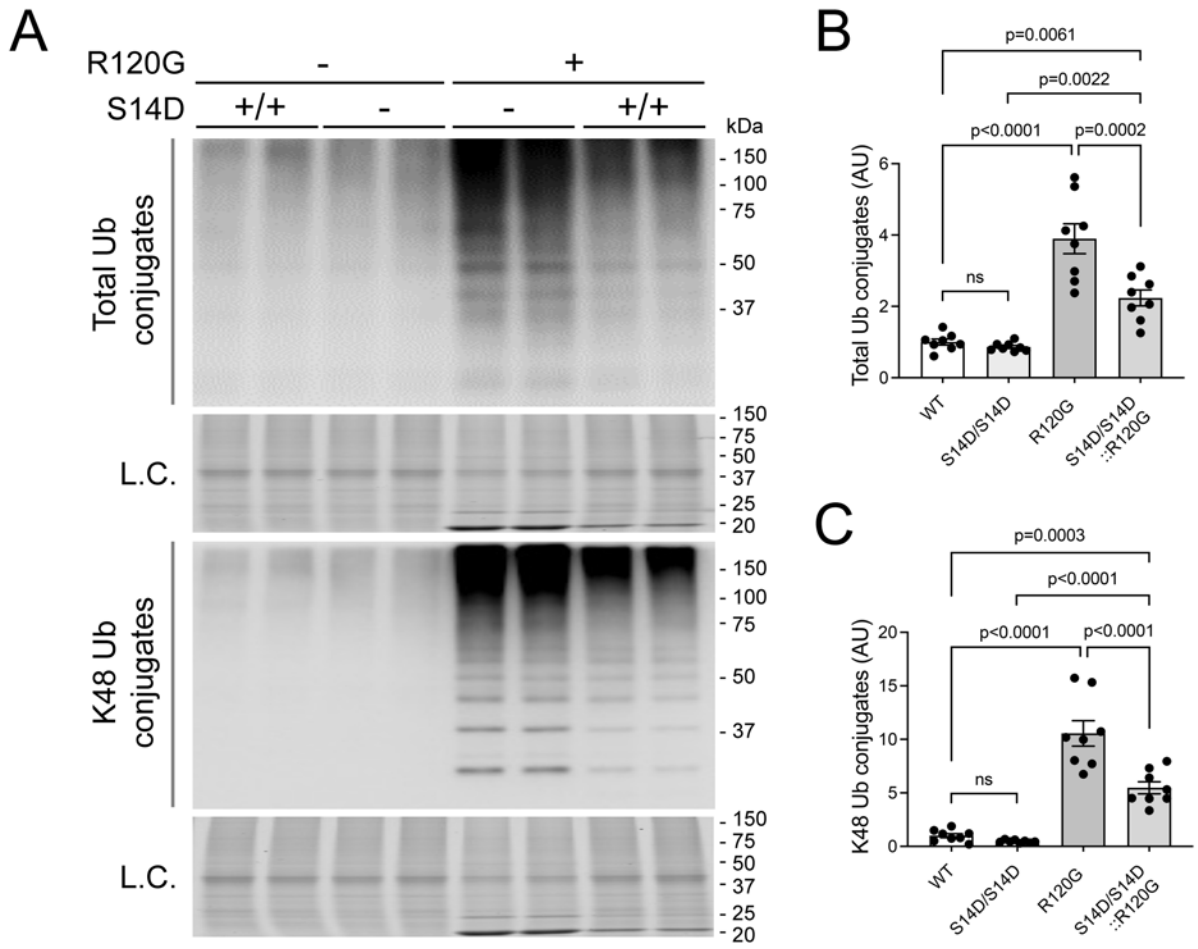

Figure 24. Effect of S14D on the levels of ubiquitin conjugates in R120G mouse hearts. Littermate WT, S14D/S14D, R120G, and S14D/S14D::R120G mice were sacrificed at 6m. Proteins from ventricular myocardium were analyzed. **A** ~ **C**, Representative images (A) and pooled densitometry data of Western blots for total (B) and K48-linked (C) ubiquitin conjugates. Each lane or dot represents an individual mouse (male to female 1:1); mean±SEM; two-way ANOVA followed by Tukey's test.

3.3.2. Amelioration of CryAB^{R120G}-induced cardiac pathology by S14D

We next examined aberrant CryAB-positive protein aggregates using immunofluorescence confocal microscopy. At 6m, aberrant CryAB-positive protein aggregates were not detected in WT mouse hearts but were readily detectable in the cardiomyocytes of R120G hearts. More importantly, the CryAB aggregates were clearly less abundant in S14D/S14D::R120G mice compared with their littermate R120G control mice (**Figure 25**). Consistently, R120G mice developed pronounced cardiac hypertrophy at 6m, as indicated by a higher ventricular weight-to-body weight ratio (VW/BW), compared with that of WT mice (**Figure 26**). This increase in VW/BW ratios was significantly attenuated in the S14D/S14D::R120G group (**Figure 26**). At the molecular level, cardiac pathology is commonly accompanied by reactivation of the fetal gene program. Ventricular mRNA levels of atrial natriuretic factor (*Nppa*), brain natriuretic peptide (*Nppb*) and β-myosin heavy chain (*Myh7*) were markedly upregulated and, reciprocally, α-myosin heavy chain (*Myh6*) was downregulated in R120G mice; more importantly, these changes were significantly blunted in the S14D/S14D::R120G mice (**Figure 27**). Notably, S14D/S14D mice displayed comparable ventricular weights and mRNA levels of the examined fetal genes compared with WT mice (**Figure 26, 27**). These results indicate that genetic mimicry of pS14-Rpn6 is benign and ameliorates cardiac pathology in proteinopathy animals.

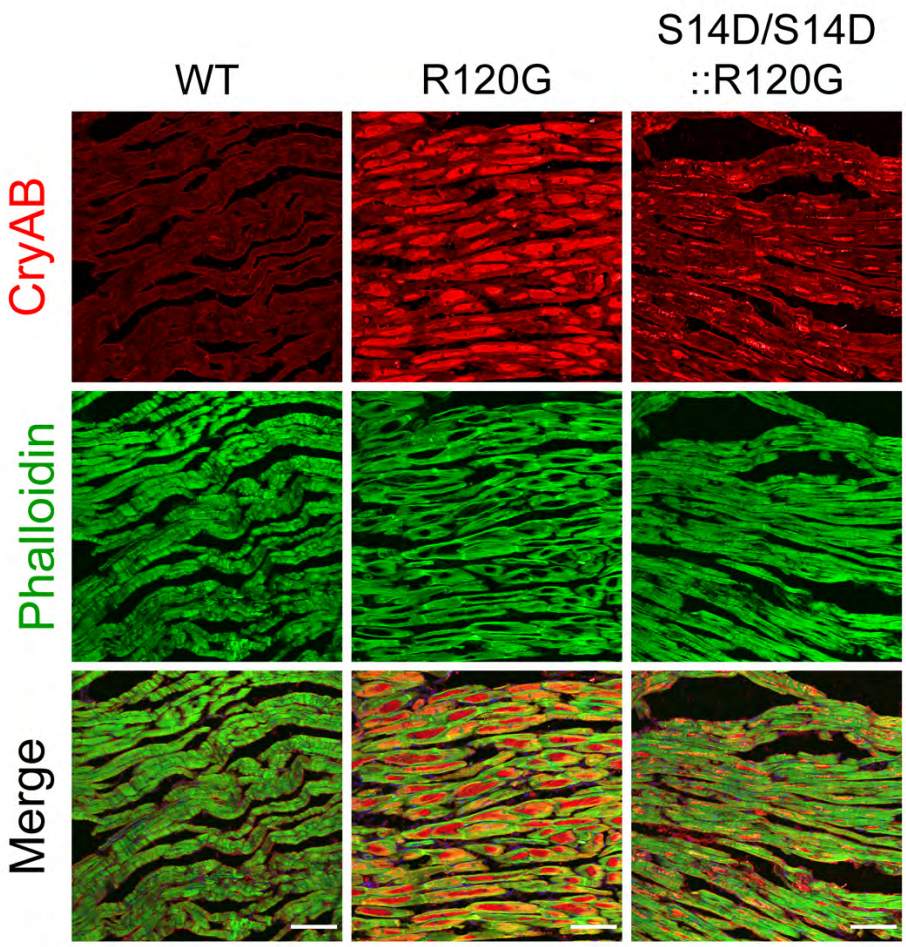

Figure 25. Immunofluorescence confocal micrographs for aberrant CryAB aggregates. Representative confocal micrographs of WT, R120G, and homozygous S14D-couple R120G mouse ventricular myocardium immunofluorescence stained for CryAB (red) at 6m. Alexa Fluor 488-conjugated Phalloidin was used to stain F-actin to identify cardiomyocytes. Scale bar=100 μm.

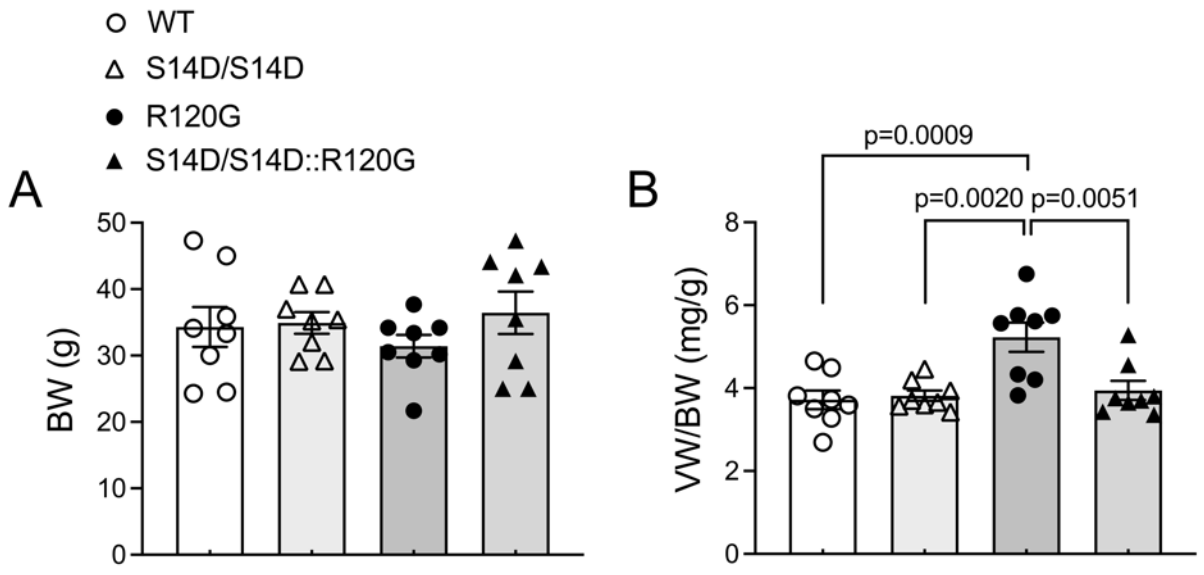

Figure 26. S14D attenuates R120G-induced ventricular hypertrophy.

A, Body weight with indicated genotypes at 6m. **B**, Body weight-normalized ventricular weights of mice with indicated genotypes at 6m. Each dot represents an individual mouse (male to female 1:1); mean±SEM; two-way ANOVA followed by Tukey's test.

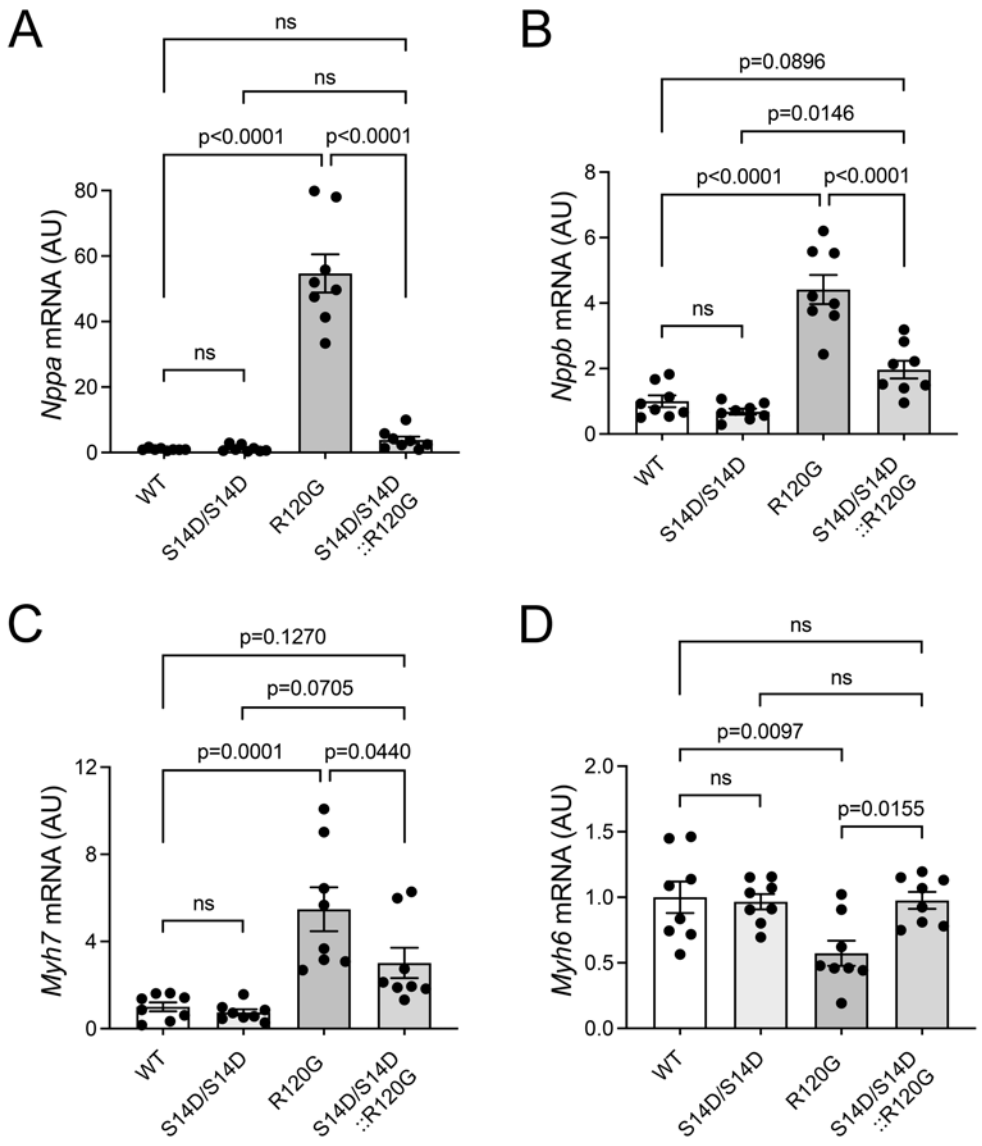

Figure 27. Effect of S14D on R120G-induced cardiac fetal gene reactivation.

A ~ **D**, Comparison of mRNA levels of the indicated genes. Total RNAs extracted from ventricular myocardium were used for real-time qPCR analyses for atrial natriuretic peptide (*Nppa*; A), brain natriuretic peptide (*Nppb*; B), β-myosin heavy chain (*Myh7*; C), and α-myosin heavy chain (*Myh6*; D). Each dot represents an individual mouse (male to female 1:1); mean±SEM; two-way ANOVA followed by Tukey's test.

3.3.3. S14D attenuates CryAB^{R120G}-induced cardiac malfunction

The results described above establish that S14D suffices to facilitate proteasomal degradation of misfolded proteins and thereby attenuate cardiac proteotoxic stress. This prompted us to further determine the impact on cardiac function. We performed serial echocardiography on WT, S14D/S14D, R120G, and S14D/S14D-coupled R120G mice at 1m, 3m, 4.5m, and 6m. All the mice of the same sex had comparable body weights at least during the 6m of observation (**Figure 28A**). Compared with WT mice, R120G mice started displaying a significantly smaller LVID;d and LVEDV, and greater LVPW;d, EF and FS, albeit unchanged SV, at 3m (**Table 11**), indicative of a compensatory stage. Starting at 3m, R120G mice had discernibly lower heart rate, consistent with prior reports,[107,128] and thereby lower CO than WT mice (**Table 11-13**). With the disease progression, the systolic function of R120G mice became compromised, as indicated by the progressive decreases in EF, FS, SV and CO at 4.5m and 6m. These echocardiographic abnormalities were substantially attenuated in the S14D/S14D::R120G groups (**Figure 28C-28F, Table 12, 13**). S14D was also trending to, not significantly though, restore the heart rate of R120G mice (**Figure 28G**). At 6m, S14D/S14D::R120G mice exhibited better systolic parameters, as indicated by greater LVPW;s, shorter LVID;s and smaller LVESV (**Table 13**). These protective effects by S14D knock-in were observed in both female and male mice. These data show that genetic mimicry of pS14-Rpn6 effectively improves cardiac function and attenuates CryAB^{R120G}-induced cardiomyopathy.

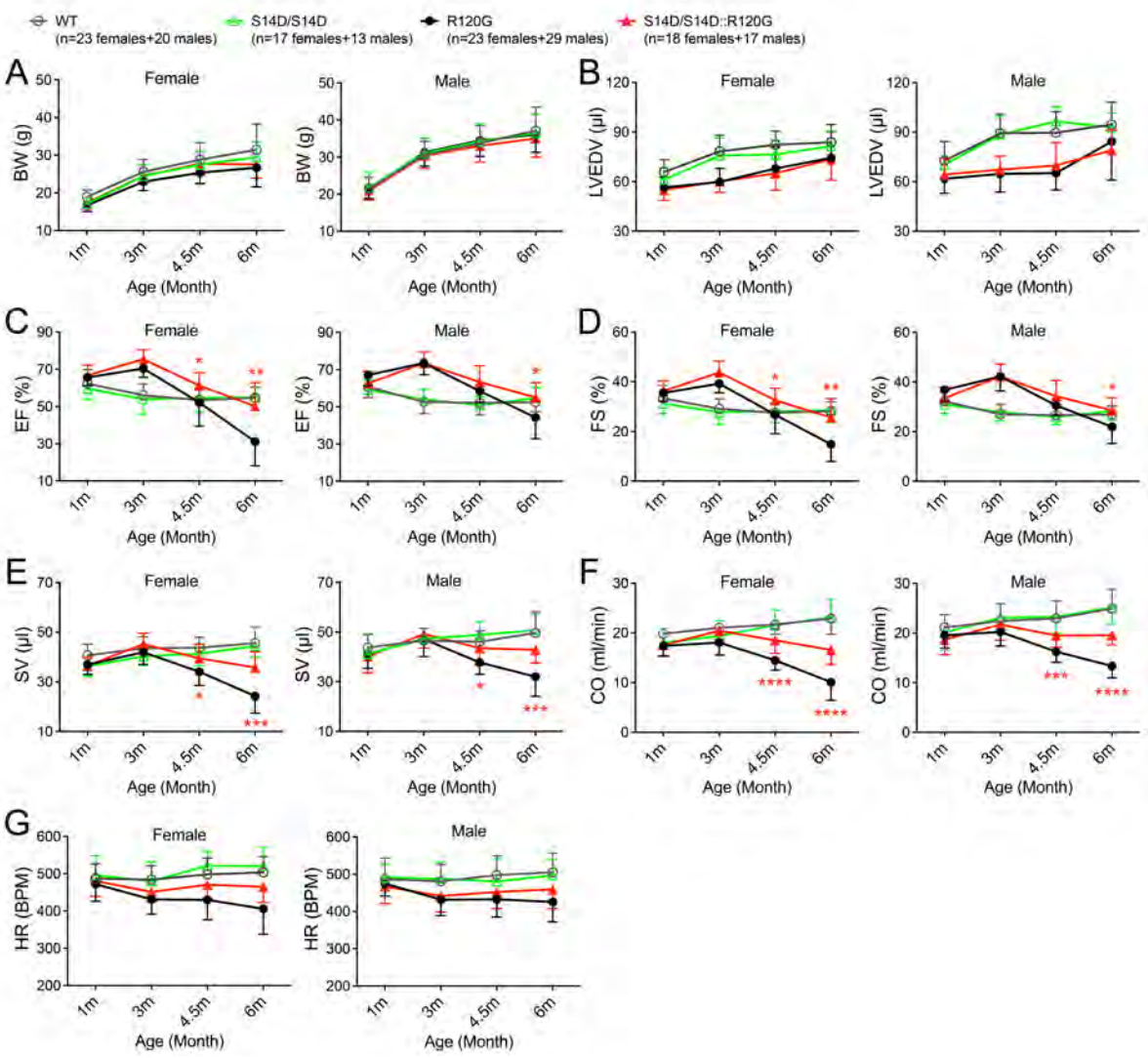

Figure 28. S14D ameliorates R120G-induced cardiac malfunction.

Littermate mice of indicated genotypes were subjected to serial echocardiography at 1, 3, 4.5, and 6 months. **A**, Time course of changes in body weight of females (left panel) and males (right panel). **B** ~ **G**, Time course of changes in LV parameters derived from the serial echocardiography of female (left panels) and male (right panels) littermate mice. Mean±SD; two-way repeated measures ANOVA followed by Tukey's test; *p<0.05, **p<0.01, ***p<0.001, ****p<0.0001 S14D/S14D::R120G vs. R120G groups.

Table 11. Echocardiographic parameters from WT, S14D/S14D, R120G, and S14D/S14D::R120G mice at 3m

	WT		S14D/S14D		R120G		S14D/S14D::R120G	
	Female	Male	Female	Male	Female	Male	Female	Male
N	23	20	17	13	23	29	18	17
BW (g)	25.6±3.3	30.6±3.7	24.5±2.9	31.0±4.2	23.0±2.4	31.3±3.7	24.5±1.8	30.3±3.4
HR (bpm)	484±37	481±45	480±52	488±44	431±40 ***	432±43 **	451±25 *	442±43
EF (%)	56.07±6.03	52.60±6.22	53.98±7.80	54.03±5.56	70.40±4.72 ****	73.53±6.33 ****	75.46±4.99 ****	73.53±5.98 ****
FS (%)	29.10±4.02	26.98±4.02	27.79±5.08	27.86±3.53	39.30±3.73 ****	42.30±5.90 ****	43.75±4.51 ****	42.23±5.03 ****
SV (µl)	43.5±4.6	46.6±5.0	40.3±3.9	47.4±4.0	41.9±4.9	47.2±7.1	45.2±4.4	49.2±5.7
CO (ml/min)	21.0±2.5	22.4±3.5	19.4±3.1	23.1±2.5	18.1±2.5 **	20.3±2.9 **	20.4±2.5	21.7±3.1
LVPW;d (mm)	0.59±0.06	0.62±0.07	0.55±0.04	0.61±0.05	0.79±0.08 ****	0.86±0.08 ****	0.81±0.02 ****	0.81±0.10 ****
LVPW;s (mm)	0.92±0.10	0.95±0.10	0.86±0.08	0.94±0.09	1.25±0.10 ****	1.36±0.13 ****	1.31±0.13 ****	1.35±0.16 ****
LVID;d (mm)	4.19±0.22	4.43±0.24	4.13±0.25	4.41±0.24	3.74±0.21 ****	3.86±0.29 ****	3.75±0.17 ****	3.93±0.21 ****
LVID;s (mm)	2.97±0.29	3.24±0.32	2.99±0.36	3.19±0.31	2.27±0.23 ****	2.23±0.34 ****	2.11±0.23 ****	2.27±0.28 ****
LVEDV (µl)	78.3±9.8	89.3±11.6	75.8±10.8	88.4±11.2	59.8±8.1 ****	64.7±11.0 ****	60.1±6.7 ****	67.3±8.2 ****
LVESV (µl)	34.7±8.2	42.8±9.8	35.5±9.9	41.1±9.3	17.9±4.7 ****	17.5±5.6 ****	14.9±4.2 ****	18.0±5.4 ****

Mean±SD; two-way repeated measures ANOVA followed by Tukey's test; *p<0.05, **p<0.01, ***p<0.001, ****p<0.0001 vs. WT mice.

Table 12. Echocardiographic parameters from WT, S14D/S14D, R120G, and S14D/S14D::R120G mice at 4.5m

	WT		S14D/S14D		R120G		S14D/S14D::R120G	
	Female	Male	Female	Male	Female	Male	Female	Male
N	23	20	17	13	23	29	18	17
BW (g)	28.8±4.5	33.8±4.7	27.5±3.3	34.2±4.8	25.3±2.7	34.5±4.3	27.8±2.9	33.1±4.4
HR (bpm)	498±44	497±53	521±39	480±62	430±53 ***	433±48 **	470±39 #	452±45 #
EF (%)	53.46±6.14	52.10±6.49	54.57±7.21	50.81±4.75	53.14±12.68	58.45±5.94 *	61.27±6.98 **,#	63.33±8.70 **
FS (%)	27.46±4.01	26.68±4.13	28.15±4.61	25.86±2.93	26.80±7.68	30.52±3.97	32.56±4.86 *,#	34.27±6.38 **
SV (µl)	43.7±4.3	46.1±4.4	41.4±4.9	48.9±5.4	34.1±5.5 ****	37.8±4.8 ****	39.5±5.8 #	43.5±6.7 #
CO (ml/min)	21.7±1.9	23.0±3.5	21.6±3.0	23.2±3.3	14.5±2.0 ****	16.3±2.2 ****	18.5±2.6 **,####	19.5±2.4 *,###
LVPW;d (mm)	0.62±0.05	0.65±0.05	0.59±0.03	0.61±0.06	0.93±0.10 ****	0.95±0.12 ****	0.90±0.10 ****	0.90±0.14 ****
LVPW;s (mm)	0.94±0.09	0.98±0.09	0.92±0.08	0.95±0.10	1.22±0.16 ****	1.28±0.14 ****	1.28±0.10 ****	1.33±0.18 ****
LVID;d (mm)	4.28±0.18	4.43±0.27	4.14±0.20	4.58±0.18	3.93±0.33 ***	3.87±0.26 ****	3.87±0.26 ****	3.98±0.32 ***
LVID;s (mm)	3.11±0.27	3.26±0.35	2.98±0.30	3.39±0.21	2.90±0.52	2.70±0.30 ***	2.61±0.32 ****	2.63±0.41 ***
LVEDV (µl)	82.3±8.3	89.6±12.7	76.4±8.7	96.4±8.8	67.9±13.1 ****	65.2±10.3 ****	65.0±10.2 ****	69.8±13.9 **
LVESV (µl)	38.6±8.0	43.5±10.9	35.0±8.4	47.5±7.1	33.8±14.5	27.4±7.5 ****	25.5±7.3 ****	26.3±10.1 ***

Mean±SD; two-way repeated measures ANOVA followed by Tukey's test; *p<0.05, **p<0.01, ***p<0.001, ****p<0.0001 vs. WT mice; #p<0.05, ##p<0.01, ###p<0.001, ####p<0.0001 S14D/S14D::R120G vs. R120G mice.

Table 13. Echocardiographic parameters from WT, S14D/S14D, R120G, and S14D/S14D::R120G mice at 6m

	WT		S14D/S14D		R120G		S14D/S14D::R120G	
	Female	Male	Female	Male	Female	Male	Female	Male
N	23	20	17	13	16	23	15	15
BW (g)	31.5±6.8	37.1±6.4	29.5±4.0	36.5±5.1	26.7±5.2	36.0±4.8	27.6±3.6	35.1±5.1
HR (bpm)	503±42	505±51	521±50	497±44	406±68 ***	425±53 ***	465±42	459±51
EF (%)	54.67±5.70	52.49±5.16	54.99±7.24	54.73±5.56	31.15±12.98 ****	44.27±11.42 *	50.20±12.61 ##	55.12±7.88 #
FS (%)	28.24±3.73	26.93±3.36	28.50±4.85	28.38±3.71	14.84±6.85 ****	21.98±6.77 *	25.63±7.61 ##	28.57±5.07 #
SV (µl)	45.6±6.6	49.7±8.6	44.4±4.4	50.8±6.5	24.3±6.9 ****	32.0±7.9 ****	35.8±6.3 ***,###	42.9±5.3 ###
CO (ml/min)	22.9±3.2	24.9±4.0	23.2±3.7	25.2±3.3	10.1±3.6 ****	13.4±2.4 ****	15.6±2.9 ****,####	19.5±2.0 ***,####
LVPW;d (mm)	0.65±0.08	0.65±0.06	0.60±0.04	0.63±0.06	0.99±0.20 ****	1.05±0.11 ****	0.99±0.08 ****	1.00±0.12 ****
LVPW;s (mm)	1.00±0.10	0.98±0.11	0.93±0.07	1.01±0.08	1.15±0.21	1.25±0.15 ****	1.28±0.10 ****	1.33±0.13 ****
LVID;d (mm)	4.31±0.24	4.53±0.29	4.26±0.20	4.51±0.18	4.08±0.36	4.29±0.49 *	4.07±0.31	4.20±0.28 *
LVID;s (mm)	3.09±0.26	3.31±0.25	3.05±0.32	3.23±0.22	3.49±0.66 *	3.30±0.48	3.05±0.50	3.01±0.38
LVEDV (µl)	83.8±10.8	94.6±13.6	81.5±9.1	92.9±8.5	74.4±15.9	84.2±23.3	73.6±12.8	79.0±12.2 *
LVESV (µl)	38.2±7.5	44.9±8.1	37.1±9.0	42.1±6.9	54.0±26.0 *	46.3±14.8	37.8±14.5	36.1±11.0

Mean±SD; two-way repeated measures ANOVA followed by Tukey's test; *p<0.05, **p<0.01, ***p<0.001, ****p<0.0001 vs. WT mice; #p<0.05, ##p<0.01, ###p<0.001, ####p<0.0001 S14D/S14D::R120G vs. R120G mice.

3.3.4. S14D delays premature death of R120G mice

Consistent with the cardiac function data, the Kaplan-Meier survival analysis of the same cohort revealed that both S14D/+::R120G and S14D/S14D::R120G groups showed significantly longer lifespans than the littermate R120G control group (S14D/+::R120G vs. R120G: $p<0.001$; S14D/S14D::R120G vs. R120G: $p<0.001$, **Figure 29A**). Notably, this was true when males (S14D/+::R120G vs. R120G: $p=0.007$; S14D/S14D::R120G vs. R120G: $p<0.001$, **Figure 29B**) and females (S14D/+::R120G vs. R120G: $p=0.010$; S14D/S14D::R120G vs. R120G: $p=0.003$, **Figure 29C**) are analyzed separately.

Taken together, genetic mimicry of pS14-Rpn6 protects against cardiac proteotoxicity, thereby attenuates $CryAB^{R120G}$-induced cardiac malfunction and lifespan shortening.

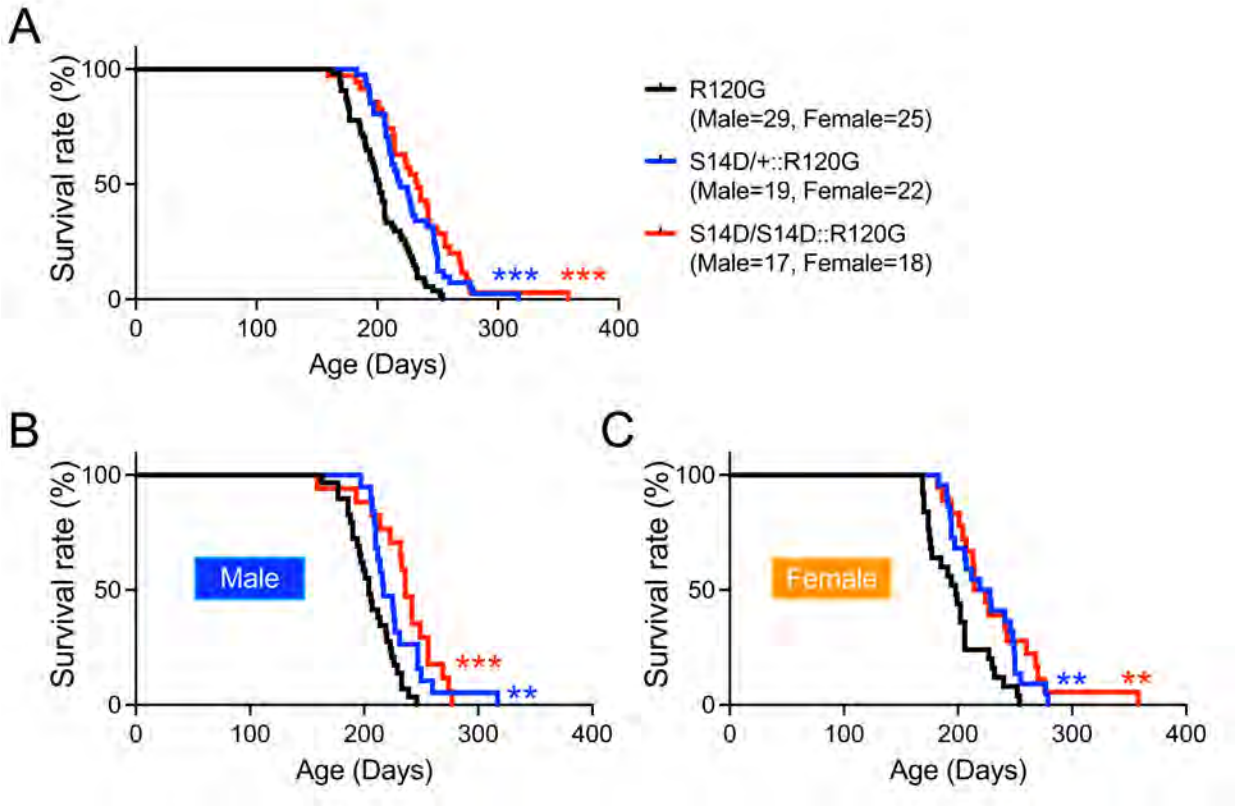

Figure 29. S14D ameliorates R120G-induced lifespan shortening.

A ~ **C**, Kaplan-Meier survival analysis for combined sex (A), male (B), and female (C). When males and females are combined, the median life spans of R120G, S14D/+::R120G, and S14D/S14D::R120G mice are 201.5, 219 and 233 days, respectively; for males, the median life spans are 204, 217 and 236 days, respectively; for females, the median life spans are 198, 223.5 and 219 days, respectively. * in red denotes S14D/S14D::R120G vs. R120G groups; * in blue denotes S14D/+::R120G vs. R120G groups; **p<0.01, ***p<0.001 determined by log-rank test.

3.3.5. The effect of S14D on proteasome assembly

Consistent with the observations from **Figure 21**, compared with WT mice, R120G mice displayed increased myocardial 30S proteasomes at both 3m and 6m and increased 26S proteasomes at 6m, which is likely a compensatory response to misfolded protein overload. Interestingly, rather than mimicking promoted proteasome assembly by PKA, S14D mice appeared to show decreased levels of assembled 30S and 26S proteasomes at 3m at baseline while the decreases were not detected at 6m. When coupled with R120G, S14D did not show discernible effects on the proteasome assembly at 3m, but the increases of assembled 30S, 26S, 20S and 19S in R120G at 6m were all attenuated by S14D (**Figure 30)**.

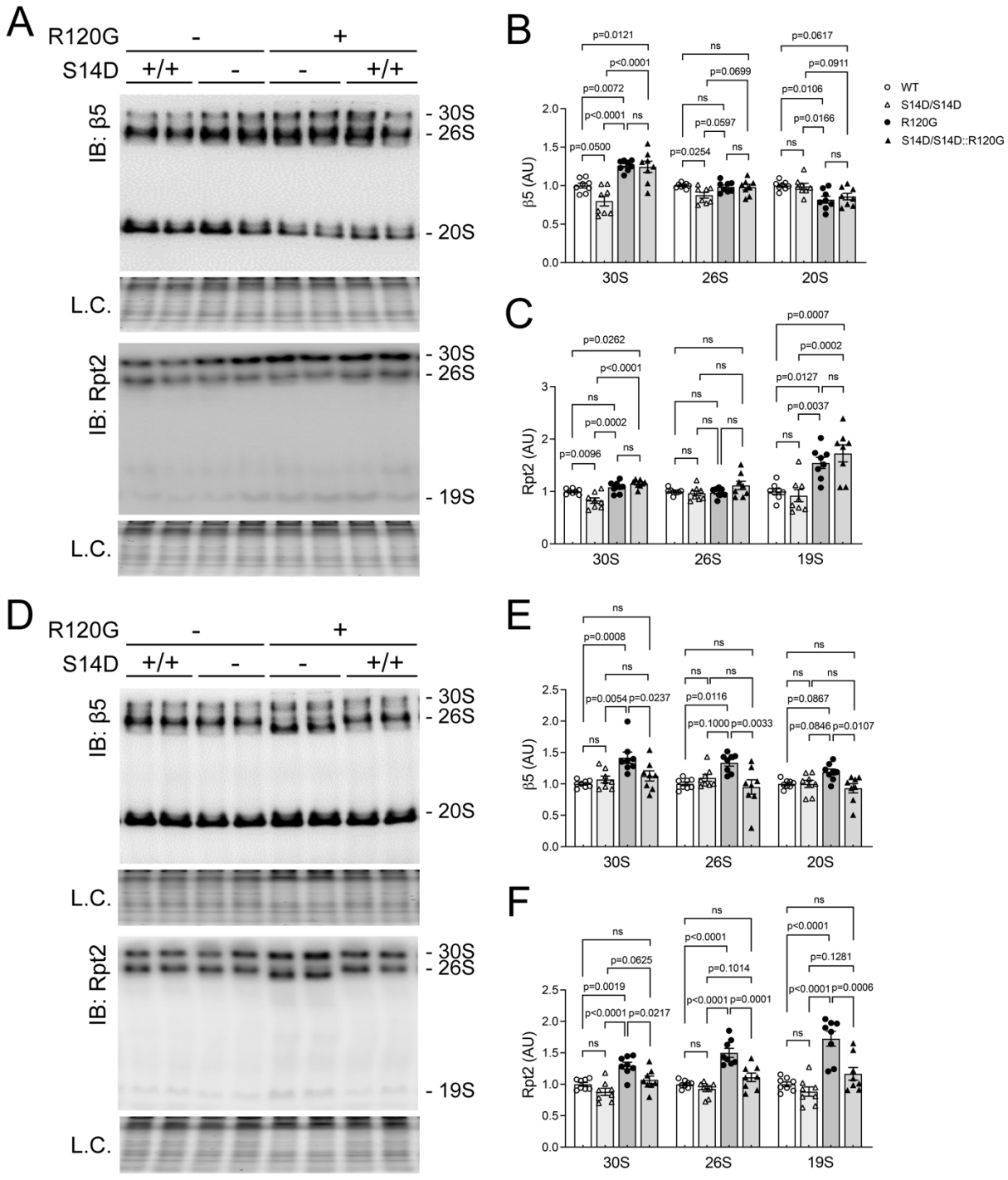

Figure 30. Effect of S14D on proteasome assembly.

Crude native protein extracts from ventricular myocardium of WT, S14D/S14D, R120G, and S14D/S14D::R120G littermate mice were fractionated with native gel electrophoresis followed by immunoblotting. **A** ~ **C**, Representative images (A) and pooled densitometry data of immunoblots for β5 (B) and Rpt2 (C) in mice at 3m. **D** ~ **F**, Representative images (D) and pooled densitometry data of immunoblots for β5 (E) and Rpt2 (F) in mice at 6m. Each lane or dot represents an individual mouse (male to female 1:1); mean±SEM; two-way ANOVA followed by Tukey's test.

3.4. cAMP augmentation increased proteasome-mediated degradation of misfolded proteins in cultured cardiomyocytes

To test whether the effects observed in the S14D mice are cardiomyocyte-autonomous, we next used cardiomyocyte cultures to examine the effect of cAMP/PKA activation on proteasomal degradation of $CryAB^{R120G}$. Our lab has successfully established an adenovirus harboring the expression cassette of HA-tagged $CryAB^{R120G}$ to distinguish the mutant CryAB from endogenous CryAB.[187,188] Ad-HA-$CryAB^{R120G}$ was overexpressed in cultured NRCMs via adenoviral gene delivery. NRCMs treated with forskolin exhibited a modest but statistically significant decrease in $CryAB^{R120G}$ protein levels than vehicle treated NRCMs ($p=0.0253$). This reduction is reversed in the presence of a proteasome inhibitor bortezomib (BZM), suggesting that the lower $CryAB^{R120G}$ protein level is caused by increased proteasome-mediated degradation (**Figure 31A, 31B**). We next measured the proteasome flux by quantifying the difference of $CryAB^{R120G}$ protein levels in the presence or absence of proteasome inhibition. Forskolin treated NRCMs displayed a dramatically higher proteasome flux of the $CryAB^{R120G}$ proteins than the vehicle treated cells ($p<0.0001$, **Figure 31C**), indicating that cAMP augmentation by forskolin effectively increases proteasome-mediated degradation of misfolded proteins in the cultured cardiomyocytes. This conclusion is also supported by the forskolin-induced decreases in $CryAB^{R120G}$ protein levels in the NP-40 insoluble protein fractions (**Figure 32**).

Consistent with *in vivo* data, by overexpressing Ad-HA-$CryAB^{R120G}$ proteins in NMCMs isolated from WT and homozygous S14D mice, we observed significantly lower $CryAB^{R120G}$ protein levels in S14D/S14D cardiomyocytes than in WT cardiomyocytes ($p=0.0028$, **Figure 33).**

These results confirm that both cAMP augmentation and S14D knock-in promote proteasome-mediated degradation of misfolded proteins in cardiomyocytes.

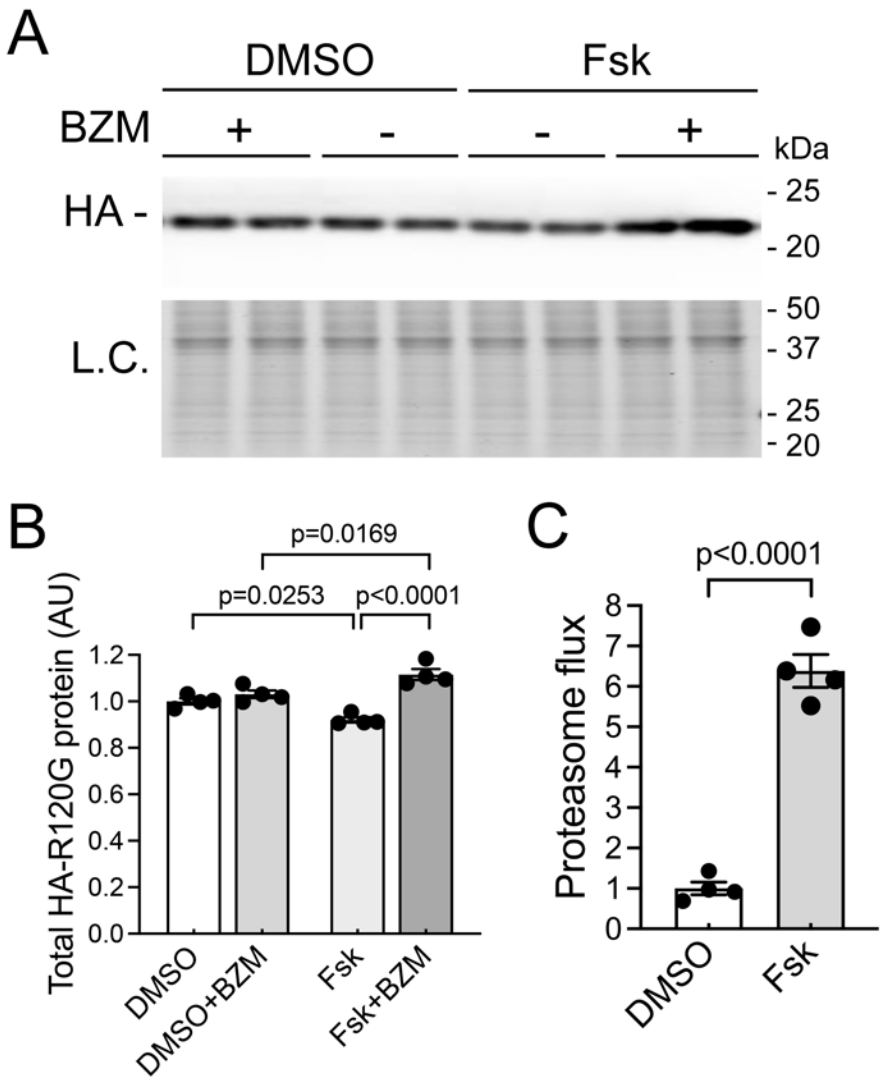

Figure 31. cAMP augmentation increased proteasome-mediated degradation of CryAB^{R120G} in cultured cardiomyocytes.

Cultured NRCMs were infected with recombinant adenovirus expressing Ad-HA-CryAB^{R120G} in serum-free media for 6 hours followed by 48-hour culture in DMEM containing 2% serum before treatment with forskolin (1 μM) or vehicle control (0.1% DMSO) for 4 hours. The proteasome inhibitor bortezomib (BZM, 50 nM) or volume corrected DMSO were applied to the cultured cells 2 hours after the initiation of Fsk treatment. **A** and **B**, Representative images (A) and pooled

densitometry data (B) of Western blot for HA-tagged CryAB^{R120G}. **C**, Proteasome flux. The proteasome flux was measured by quantifying the difference of CryAB^{R120G} protein levels in the presence or absence of proteasome inhibition. Each lane or dot represents a biological repeat; Mean±SEM; two-way ANOVA followed by Tukey's test for (B) and unpaired Student's *t* test for (C).

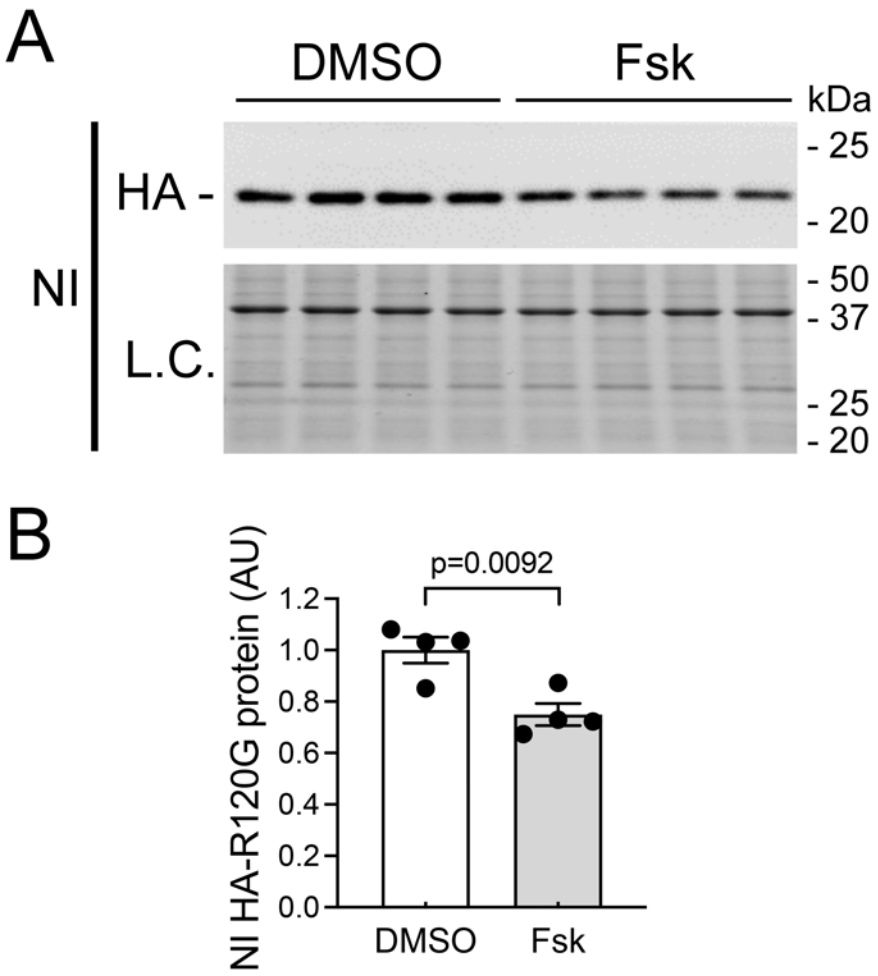

Figure 32. cAMP augmentation decreased intermediate CryAB^{R120G} oligomers in cultured cardiomyocytes.

Cultured NRCMs were infected with recombinant adenovirus expressing Ad-HA-CryAB^{R120G} in serum-free media for 6 hours followed by 48-hour culture in DMEM containing 2% serum before treatment with forskolin (1 μM) or vehicle control (0.1% DMSO) for 4 hours. **A** and **B**, Representative images (A) and pooled densitometry data of Western blot for HA-tagged CryAB^{R120G} in NP-40-insolulble (NI; B) protein fractions. Each lane or dot represents a biological repeat; Mean±SEM; unpaired Student's *t* test.

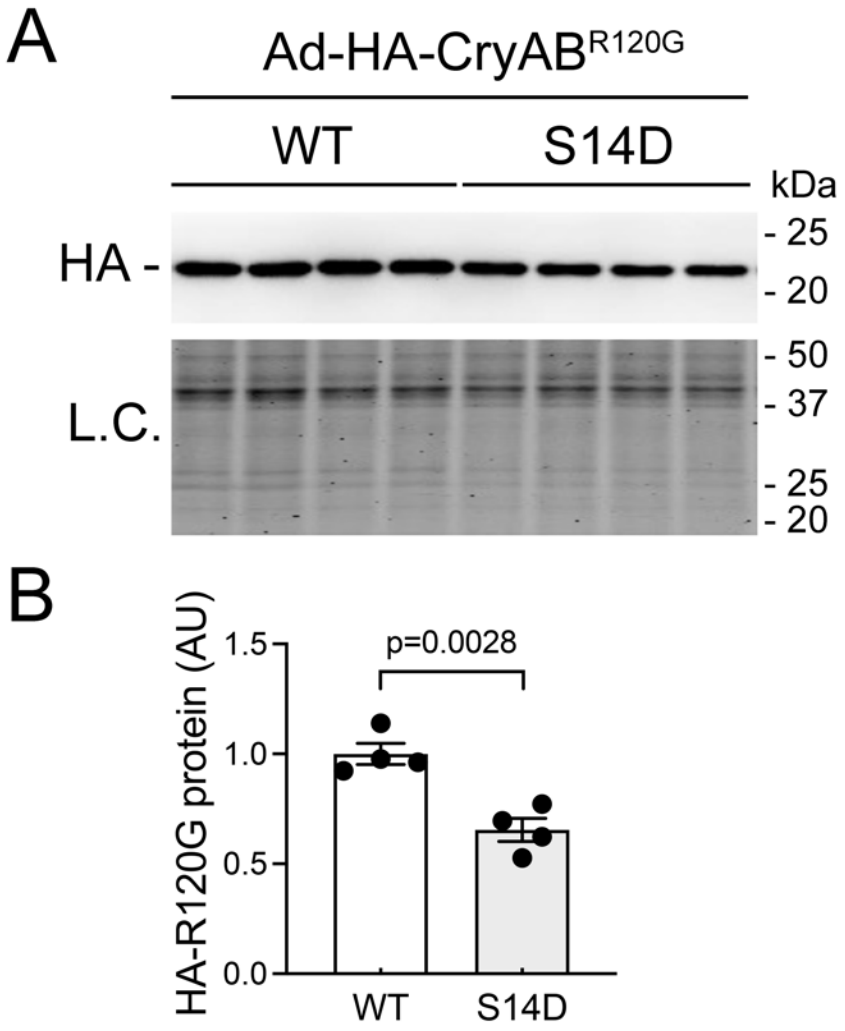

Figure 33. S14D decreased the steady-state protein levels of CryAB^{R120G} in cultured cardiomyocytes.

A and **B,** Representative images (A) and pooled densitometry data (B) of Western blot for HA-tagged CryAB^{R120G} in cultured NMCMs were infected with Ad-HA-CryAB^{R120G} in serum-free media for 6 hours followed by 48-hour culture in DMEM containing 2% serum before harvest. Whole cell lysates were used for Western blots for HA-tagged CryAB^{R120G}. Each lane or dot represents a biological repeat; mean±SEM; unpaired Student's *t* test.

DISCUSSION

PFI is implicated in the progression from a large subset of heart diseases, including those with IPTS, to heart failure.[84,108,132] There are currently no effective therapies targeting cardiac IPTS.[76] Hence, a better understanding on proteasome phospho-regulation is undoubtedly of high significance to guide the development of new therapeutic strategies. Previously, Goldberg's group demonstrated exclusively in cultured cells that cAMP/PKA activates 26S proteasomes by directly phosphorylating RPN6 at Ser14.[123,125] As illustrated in **Figure 34**, taking advantage of our newly created S14A and S14D mice, the present study has established for the first time in animals that pS14-RPN6 is responsible for the activation of 26S proteasomes by PKA. More importantly, here we have discovered a selective downregulation of myocardial pS14-Rpn6 during cardiac IPTS and further demonstrated that enhancing 26S proteasomes via genetic mimicry of pS14-Rpn6 protects against cardiac IPTS induced by $CryAB^{R120G}$ in animals and thereby effectively curtails cardiac malfunction and disease progression. These new findings establish a novel concept that selective impairment of the proteasome activation by PKA is a key pathogenic factor for cardiac proteinopathy and its targeting can conceivably be exploited to develop new strategies for treating heart disease with IPTS. This is highly significant because a large subset of cardiovascular disease possesses cardiac IPTS.[76]

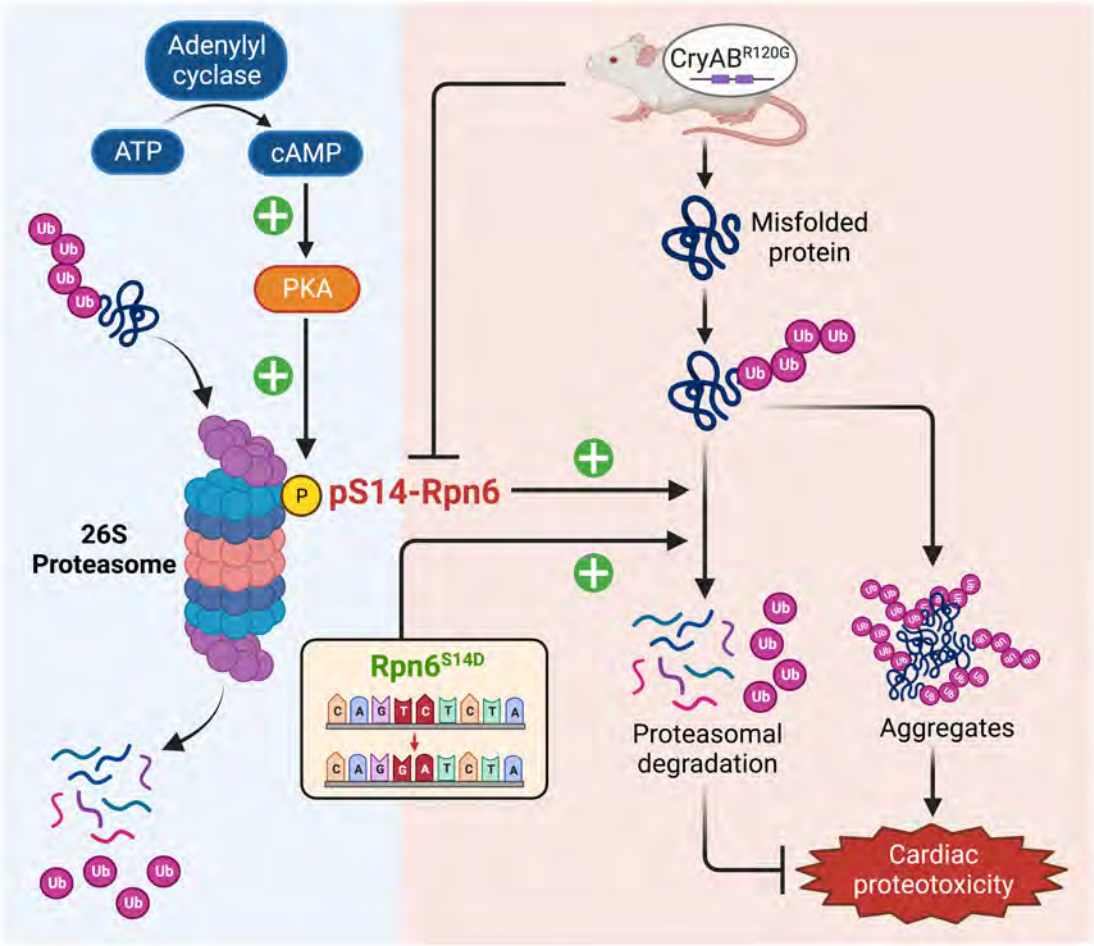

Figure 34. A schematic illustration of the main findings of this study.

1. The activation of 26S proteasomes by cAMP/PKA is mediated solely by pS14-RPN6

PKA has been long implicated in proteasome phosphoregulation.[119,120] A recent study showed that Ser14-RPN6 was selectively phosphorylated by cAMP/PKA and this phosphorylation was solely responsible for cAMP/PKA-mediated 26S proteasome activation in cultured non-cardiac cells.[123] We have subsequently demonstrated that cAMP augmentation markedly increased pS14-Rpn6 in cultured cardiomyocytes in a PKA-dependent manner, which was associated with

expedited degradation of a surrogate UPS substrate.[128] However, the physiological relevance of pS14-Rpn6 has not been established in animals. Here, our experiments in cell cultures and in mice unequivocally establish that Ser14 of Rpn6 is the primary, if not the only, phosphosite responsible for the activation of 26S proteasomes by cAMP/PKA. First, with S14A mice, our findings provide compelling support that pS14-Rpn6 is required for PKA to activate the proteasome. Augmentation of cAMP with an adenylate cyclase activator significantly increased myocardial pS14-Rpn6 proteins and 26S proteasome activities in a PKA-dependent manner in WT mice, but such effects were completely lost in S14A mice (**Figure 11, 12**). Similar findings were observed in cultured MEFs and AMCMs derived from S14A mice (**Figure 8-10**). Second, myocardium and cardiomyocytes from S14D mice displayed significantly higher proteasome peptidase activities than WT controls (**Figure 15**); and S14D enhanced cardiac UPS proteolytic function (**Figure 14**), together proving that pS14-Rpn6 is sufficient to activate the proteasome. Along with related prior reports,[123,125] the data of the present study suggest that other proteasome phosphosites identified as targets of PKA via *in vitro* assays are unlikely physiologically relevant. Therefore, our newly created knock-in (S14A and S14D) mice confer valuable *in vivo* tools to define the (patho)physiological significance of proteasome activation by cAMP/PKA, adding a new dimension to the (patho)physiology of cAMP/PKA signaling.

2. Basal pS14-Rpn6 appears to be dispensable in mice

We observed that under basal conditions, the proteasome activities of S14A MEFs were discernibly lower than that of WT MEFs (**Figure 10A, 10B**), which is consistent with the prior study, in which 26S proteasomes purified from Rpn6-S14A mutant-expressed 293A cells exhibited decreased capacities to hydrolyze proteasome substrates and ATP and reduced clearance of

aggregation-prone proteins than those purified from Rpn6-WT expressed cells.[123] Interestingly, although pS14-Rpn6 and proteasome activation by PKA were completely lost in adult S14A cardiomyocytes and mouse hearts, their proteasome activities at baseline seem unchanged compared with WT controls (**Figure 10C, 11)**. The discrepancy might rise from the different natures of cell types: 293A cells and MEFs are embryonic cells with high capacity of differentiation, whereas cardiomyocytes are terminally differentiated. Oxidative and misfolded proteins produced during differentiation are preferably degraded by the UPS and the elimination of unwanted proteins occurs during normal embryonic development. 26S proteasome activities are considerably elevated during embryogenesis to rid the embryonic cells of protein damage and maintain proteostasis.[189,190] Therefore, the significant differences of proteasome activities between WT and S14A cells observed from the present and previous studies suggest that pS14-Rpn6 may play a role in the proteasome regulation during cell differentiation. In consistence with the comparable proteasome activities, we did not observe S14A-exerted alterations of cardiac UPS proteolytic function (**Figure 13**), or any discernible differences in cardiac phenotypes (**Figure 2, 3**), suggesting that myocardial pS14-Rpn6 may be dispensable under basal condition. The observed results can be potentially explained by: (1) the basal phosphorylation state of myocardial Ser14-Rpn6 is very low in healthy mice under normal physiological conditions, but it will be more phosphorylated to activate the proteasomes upon the stimulation of cAMP/PKA; (2) the 26S proteasome is vigorously regulated by a sophisticated network to maintain intracellular protein homeostasis and loss of endogenous pS14-Rpn6 may be compensated by other proteasome regulatory pathways.

3. A selective impairment of pS14-RPN6 is pathogenic in cardiac IPTS

DRCs are the cardiac aspect of desmin-related myopathies (DRMs) that are pathologically featured by intra-sarcoplasmic desmin-positive aberrant protein aggregates.[104,105] DRMs arise from mutations in a number of genes, such as desmin,[191] plectin,[192] and CryAB.[179] DRC is the main cause of death in human DRM and exemplifies the pathophysiological significance of IPTS and aberrant protein aggregation in cardiac muscle. The $CryAB^{R120G}$-based DRC mouse model used in the present study recapitulates most aspects of human DRC, including intra-sarcoplasmic aberrant protein aggregation, cardiac hypertrophy, a restrictive cardiomyopathy stage followed by eventually a dilated cardiomyopathy/congestive heart failure stage, and shortened lifespan;[107,108,193] thus the R120G mice are widely used as an animal model to study cardiac IPTS.[128,194,195] PFI is a major pathogenic factor in heart diseases with IPTS, which was best demonstrated by that cardiomyocyte-restricted enhancement of proteasome function markedly decreased aberrant protein aggregation, attenuated cardiac malfunction, and delayed premature death of the R120G mice.[108] R120G mice display elevated myocardial proteasome peptidase activities to compensate for the overload of misfolded proteins (**Figure 22**), consistent with a prior report.[77] However, to our surprise, pS14-Rpn6 is not part of the natural compensatory response but rather selectively impaired pS14-Rpn6 contributes to the insufficiency. This is reflected by marked decrease of myocardial pS14-Rpn6 in R120G mice at both early (3m) and late (6m) stages of disease progression (**Figure 16**). Interestingly, the downregulation of pS14-Rpn6 at 3m was associated with an overall decrease in phosphorylated PKA substrates but, at 6m, it was dissociated with the significant increases of other phosphorylated PKA substrates (**Figure 17**), indicating that the decreased pS14-Rpn6 is due to a selective or compartmentalized defect in PKA-mediated

phosphorylation of Ser14-RPN6. It will be very interesting and important to delineate the mechanism underlying the decrease of pS14-Rpn6 in cardiac IPTS.

Moreover, we have established the defect in Ser14-RPN6 phosphorylation in the response to IPTS as a major pathogenic factor in cardiac proteotoxicity, and our data provide compelling genetic evidence that enhancement of 26S proteasome functioning by pS14-Rpn6 protects the heart against proteotoxic stress. Upon the adaptive elevations of proteasome activities induced by $CryAB^{R120G}$, S14D further increased myocardial 26S proteasome peptidase activities (**Figure 22**), which conceivably increases the UPS capacity to degrade misfolded proteins. As a result, the steady-state misfolded CryAB was remarkably reduced (**Figure 23A, 23B**). When UPS function becomes inadequate or impaired, misfolded proteins undergo aberrant aggregation with forming intermediate oligomers that is believed highly toxic to the cells.[196] Here we also show that both total and NP-40-insoluble CryAB (misfolded oligomers) in R120G hearts were markedly decreased by S14D (**Figure 23**). An increase in total ubiquitinated proteins in the cell can be caused by increased ubiquitination or inadequate proteasomal degradation and is indicative of defective proteostasis. Consistent with prior reports,[108,132] significant increases in myocardial total and K48-linked ubiquitinated proteins, indicative of PFI, were observed in R120G mice, but such increases were substantially attenuated by S14D (**Figure 24**), demonstrating that genetic mimicry of pS14-Rpn6 effectively facilitates the degradation of ubiquitinated proteins and thereby improves proteostasis. Consistently, aberrant CryAB protein aggregates in R120G mice were markedly decreased as well (**Figure 25**). At the same time point, the cardiac hypertrophy of R120G mice as indicated by increased VW/BW ratios, was attenuated by S14D, which is further supported by blunted reactivation of representative fetal genes (**Figure 26, 27**), indicating that S14D-induced improved removal of pathogenic proteins significantly attenuates cardiac pathology. Functionally,

S14D significantly delayed cardiac malfunction, evident by attenuation of the decreases in LV EF, FS, SV, and CO, and eventually delayed premature death (**Figure 28, 29**). These findings unequivocally demonstrate that genetic mimicry of proteasome activation by PKA protects against cardiac proteotoxicity.

4. pS14-RPN6 does not appear to increase myocardial proteasome assembly

The opposing nature between elevated proteasome peptidase activities and decreased pS14-Rpn6 in the R120G mice also suggests that mechanisms other than pS14-Rpn6 are utilized naturally by cardiomyocytes to increase proteasomal capacity in response to IPTS. Indeed, we detected significant increases in myocardial Rpn6 (**Figure 16**) and in assembled proteasomes (**Figures 21, 30**), indicative of increased proteasome assembly, in R120G mice. Others also reported that increased RPN6 is responsible for increased proteasome activities and resistance to IPTS in *C*. elegans.[197]

Earlier reports suggest that activation of cAMP/PKA enhances proteasome assembly,[127] more evidently increases 30S proteasomes.[123] However, the role of pS14-RPN6 in proteasome assembly has not been examined. The S14A and S14D mouse models enable us for the first time to fill this critical gap. S14A did not alter myocardial abundance of 30S or 26S proteasomes at baseline or in the early or late stages of R120G-induced cardiomyopathy, suggesting that pS14-RPN6 does not play an important role in the myocardial proteasome assembly under physiological condition or in the context of R120G-induced IPTS (**Figure 21**). The reason for this might have something to do with the fact that basal myocardial pS14-Rpn6 is low and it is further decreased in R120G mice. Notably, we observed decreased 19S proteasomes in S14A-coupled R120G mice, compared with R120G control mice at 3m. This probably results from a compensatory increase in the

incorporation of the 19S into the 30S proteasomes in the S14A-coupled R120G hearts. Even though it is significantly lower than that in WT mice, pS14-Rpn6 is present in the heart of R120G mice at a modest level (**Figure 16**), its loss might have triggered a compensatory increase in 30S proteasome assembly. Indeed, a seemingly greater level of 30S proteasomes was evident in the S14A-coupled R120G group compared with the R120G alone group although the difference did not achieve statistical significance yet likely due to a larger variation (**Figure 21A, 21C**). Such compensatory response was not evident at 6m probably due to impaired proteasome assembly with the disease progression (**Figure 21D-21F**). On the contrary, pS14-Rpn6 mimicry reduced 30S or 26S proteasomes at 3m. One possible reason could be that proteasome peptidase activities are constitutively increased by S14D, which renders the cell to require fewer proteasomes to fulfill the needs of basal protein degradation. In R120G mice, S14D did not show discernible effects on the proteasome assembly at 3m, but the increases of the 30S, 26S, 20S and 19S in R120G mice were all attenuated by S14D at 6m (**Figure 30)**. S14D significantly improved the proteasome functional efficiency and, as a result, markedly reduced misfolded protein overload at 6m (**Figure 22-25**). Thus, the compensatory increase of proteasome assembly was attenuated. Taken together, these data also indicate that pS14-Rpn6 may play little, if any, role in the regulation of proteasome assembly at baseline and during the R120G-based IPTS. The protective effect by S14D is predominantly attributable to the improved efficiency of proteasome-mediated degradation. These new findings also demonstrate that pS14-RPN6 can be additive to or potentially synergistic with increased proteasome assembly in augmenting proteasomal capacity to handle IPTS.

5. Augmentation of pS14-RPN6 as a potentially new strategy to treat heart disease

The present study, to our best knowledge, provides the first genetic evidence that PKA-induced proteasome activation protects against proteinopathy in animals, indicating that pS14-RPN6 should be explored as a potentially new strategy to treat heart disease with IPTS.

Despite great advances achieved from numerous preclinical studies over the past decades in the understanding of PKA in the heart, the precise roles of PKA in cardiac pathogenesis and therapeutics remain to be fully understood. A recent study from our group demonstrates that PDE1 inhibition, which activates both PKA and PKG, protects against proteinopathy-based heart failure likely by facilitating proteasome-mediated degradation of misfolded proteins. R120G mice treated with either a PDE1 inhibitor IC86430 or a PDE4 inhibitor piclamilast exhibited significantly increased pS14-Rpn6.[128] Similarly, genetic or pharmacological PDE10A inhibition, which also increases both cAMP and cGMP, was reported to attenuate Ang-II-induced cardiomyocyte hypertrophy *in vitro* and restrain pressure overload-induced cardiac remodeling and dysfunction *in vivo*.[198] Earlier PDE2 inhibition was also shown to protect hearts from pathological remodeling via a localized cAMP/PKA signaling pathway.[199] Cardiac hypertrophy is the most common adaptive response of the heart during virtually all heart diseases inherited or acquired, in which increased protein synthesis is inevitable, resulting in increased production of misfolded proteins.[84] Therefore, it is highly possible that pS14-Rpn6 mediates, at least in part, the attenuation of cardiac hypertrophy exerted by the inhibition of PDE1, PDE2, or PDE10A.

However, controversy exists about the role of PKA in cardiac pathogenesis. Most reports support the involvement of PKA in the development of cardiomyopathy and PKA inhibition as a potential therapeutic target to treat heart disease. For example, activation of cAMP/PKA signaling during the myocardial ischemia contributes to I/R injury;[200] activation of PKA constitutively[201] or

by chronic sympathetic stimulation[202,203] induces maladaptive cardiac hypertrophy and ultimately heart failure; beta blockers are one of the most widely prescribed classes of drug that improve LV function and reverse remodeling in human heart failure.[204] The present study has demonstrated compellingly that cAMP/PKA protects against cardiac proteotoxicity through improving PQC. Therefore, precisely targeting pS14-Rpn6 would potentially serve as an effective therapeutic strategy to treat heart disease with IPTS, while bypassing possible adverse effects of global PKA activation. Currently, this does not seem to be practical, but a good understanding of the cAMP/PKA signaling at the proteasome nanodomain should facilitate the search for a pharmacological approach to selectively augment cAMP/PKA signaling to the proteasome. An adjunct treatment to minimize undesired effects of PKA activation, such as recently proposed duo-activation of PKA and PKG,[76] could be an immediately translatable solution.

CONCLUSIONS

The discoveries from the present study overall support our hypothesis that Ser14-RPN6 phosphorylation mediates the activation of proteasomes by PKA and reduces proteotoxicity in animals.

We created the S14A and S14D mice for genetic blockade and mimicry of pS14-Rpn6, respectively. Heterozygous and Homozygous S14A and S14D mice are viable and fertile and do not display discernible gross abnormalities compared with their littermate controls during the first 12 months of age, the longest time observed in full cohorts so far. Monthly M-mode echocardiography did not reveal significant difference in LVEDV, EF, FS, CO, LV mass index (LV Mass/body weight), or body weight between WT and littermate S14A or S14D mice in either male or female cohorts during the first 7 months (S14A) or 6 months (S14D) of age, the oldest cohorts analyzed so far. The heart weight of S14A or S14D mice is comparable to that of their WT littermates. The baseline characterizations validate our S14A and S14D mice as valuable tools for the investigations into the physiological significance of pS14-RPN6 in intact animals.

In both cultured mouse cells and myocardium, cAMP augmentation-induced elevation of proteasome peptidase activity was eliminated by the genetic blockade of pS14-Rpn6, demonstrating that pS14-Rpn6 is required for cAMP/PKA to activate the proteasome. Conversely, genetic mimicry of pS14-Rpn6 was sufficient to increase basal proteasome activities in cardiomyocytes and in the mouse heart, and improve myocardial UPS performance. These findings unequivocally demonstrate pS14-RPN6 as the primary, if not the only, mechanism responsible for the activation of 26S proteasomes by cAMP/PKA.

pS14-Rpn6 appears to be dispensable for basal myocardial 26S proteasome activity or assembly, evident by comparable 26S proteasome activities and 30S, 26S, 20S and 19S

proteasome assembly in S14A mice compared with WT mice. However, rather than a compensatory increase, pS14-Rpn6 was markedly diminished during the progression of CryAB^{R120G}-induced cardiac proteinopathy. Genetic mimicry of pS14-Rpn6 further increased myocardial proteasome peptidase activities in R120G mice, leading to reductions of misfolded CryAB accumulation and aggregation and of ubiquitin conjugates. As a result, CryAB^{R120G}-induced cardiac pathology and cardiac malfunction were remarkably attenuated and the premature death of R120G mice was significantly delayed by the genetic mimicry of pS14-Rpn6. These results together compellingly demonstrate that a selective defect in pS14-Rpn6 in response to IPTS is a major pathogenic factor in CryAB^{R120G}-induced cardiac proteinopathy and that increasing pS14-Rpn6 protects the heart against proteotoxicity.

Our data gathered from the genetic mimicry of pS14-RPN6 suggest that pS14-RPN6 can enhance cardiac proteasome peptidase activities and UPS proteolytic function through a mechanism independent of increasing proteasome assembly. This is because myocardial abundance of assembled proteasomes in the S14D mice was not increased either at baseline or when coupled with CryAB^{R120G}-induced cardiac proteinopathy.

These novel findings from the present study establishes in animals that pS14-Rpn6 is responsible for the activation of 26S proteasomes by PKA and reduced pS14-Rpn6 is a key pathogenic factor in cardiac proteinopathy, thereby identifies a new therapeutic target to reduce cardiac proteotoxicity.

LIMITATIONS

We have evaluated the baseline characteristics of S14A and S14D mice by serial echocardiography for 7m and 6m, respectively, and gravimetric measurement of the heart weight at 10m. Since they were created by germline mutations, our S14A and S14D mice could be invaluable for the investigation of pS14-RPN6 in all organs/systems and a broader range of conditions and diseases. It will be important to extend the evaluation period and incorporate assessments of the physiological functions of other organ systems in order to obtain a more robust understanding of the physiological relevance of pS14-RPN6 and to enhance the interpretation and generalizability of the experimental findings.

There is no doubt that pS14-Rpn6 is blocked in the S14A mutant. However, the degree and fidelity of phosphorylation mimicry for the commonly used S14D mutant to mimic pS14-Rpn6 are uncertain. Thus, caution must be taken during the interpretation of the data, especially some of the negative data, derived from the use of the S14D.

To investigate the pathophysiological significance of pS14-Rpn6 in animals with cardiac IPTS, we utilized only the R120G mice, a classic model of DRC. Therefore, our discoveries may be limited to DRC rather than being universally applicable across all IPTS situations.

FUTURE STUDIES

The present study has provided compelling evidence proving the hypothesis that Ser14-RPN6 phosphorylation mediates the activation of proteasomes by PKA and reduces proteotoxicity in animals, by genetically blocking or mimicking pS14-Rpn6. Directly targeting pS14-Rpn6 to treat heart disease with IPTS may be challenging currently. Recently proposed duo-activation of PKA and PKG has shown protective effect in a PKA-dependent manner.[76] A pharmacological approach that selectively boosts cAMP/PKA signaling, such as a PDE4 inhibitor, could be deployed to establish the translational significance of the observed impacts of pS14-Rpn6.

In addition to priming the proteasome, PKA activation has also been associated with enhanced proteasome assembly or decreased proteasome disembly,[123,127] but the underlying mechanism is unknown. Our data suggest that pS14-RPN6 is unlikely involved in the direct regulation of cardiac proteasome assembly either under normal physiological condition or in response to a cardiac IPTS condition, which implies that the activation of PKA may engage other mechanism than pS14-RPN6 to increase the abundance of assembled proteasomes in the cell. Therefore, it will be interesting and important to elucidate the precise mechanism by which PKA enhances proteasome assembly, as such information will contribute to the understanding of proteasome regulation and the evaluation of PKA-based therapeutic strategies.

This study has established that a seemingly selective impairment in pS14-Rpn6 acts as a major pathogenic factor contributing to PFI in CryAB^{R120G}-based proteinopathy. It will be important to explore the mechanism underlying this defect. Such investigations are expected to guide the search for a precise pharmacological approach to the decreased pS14-RPN6 in cardiac diseases with IPTS.

In addition, defects in UPS including PFI have been implicated in various other human diseases, including neurodegenerative disorders (Alzheimer's disease,[85,205] Parkinson's disease[206]),

age-associated disorders,[207] and chronic liver diseases.[208,209] Other studies demonstrated that pharmacological augmentation of cAMP prevents tau-driven proteasome impairment and cognitive dysfunction,[126] and 1′-acetoxychavicol acetate protects age-related impairments in learning and memory via cAMP/PKA-dependent proteasome activation.[210] It will be very interesting to employ our S14A and S14D models to investigate the role of pS14-RPN6 in the genesis and the cAMP-augmentation treatment of these diseases.

APPENDIX I

Genotyping Rnp6^{S14A} and Rpn6^{S14D} Mice using the Tetra-Primer Amplification Refractory Mutation System (ARMS)-PCR

I. Primers

1. Outer primers for Rpn6/Psmd11 fragment
    - Forward (TetraArmsPSMD11F):

      5'-GAGATGGCGATGGGGGAGCTCGTTTGTC-3'
    - Reverse (TetraArmsPSMD11R):

      5'-CACAGTGAGTCAGCAGCACCATAGCCGGC-3'
2. Inner primers specific to S14A or S14D

    1) S14A
        - Forward (PSMD11-G allele):

          5'-GGTGGTGGAGTTCCAGAGAGCCCGGG-3'
        - Reverse (PSMD11-T allele):

          5'-GCCTCCCGGTCGGTGCTGAGTAGGGA-3'

    2) S14D
        - Forward (PSMDS14D-TC allele):

          5'-GGTGGTGGAGTTCCAGAGAGCCCGGGA-3'
        - Reverse (PSMDS14D-GA allele):

          5'-GCCTCCCGGTCGGTGCTGAGTAGGGA-3'

II. Procedure

1. Master mix for each PCR reaction

1) S14A

Compound	Amount / 20 µl reaction
10X DreamTaq^{Tm} DNA Polymerase Green Buffer	2 µl
dNTP mix	0.2 mM
TetraArmsPSMD11F	350 nM
TetraArmsPSMD11R	350 nM
PSMD11-G allele	150 nM
PSMD11-T allele	150 nM
DreamTaq^{TM} DNA polymerase	0.5 U
Template DNA	1 µl

2) S14D

Compound	Amount / 20 µl reaction
10X DreamTaq^{Tm} DNA Polymerase Green Buffer	2 µl
dNTP mix	0.2 mM
TetraArmsPSMD11F	200 nM
TetraArmsPSMD11R	200 nM
PSMDS14D-TC allele	200 nM
PSMDS14D-GA allele	200 nM
DreamTaq^{TM} DNA polymerase	0.5 U
Template DNA	1 µl

2. PCR amplifications were performed with the Techne 5PRIMEG/02 Thermal Cycler (United Kingdom) with the following profile:

   a. 94 °C for 3 min

   b. 30 cycles of:

      94 °C for 40 sec

      74.9 °C (for S14A) or 74.7 °C (S14D) for 30 sec

      72 °C 45 sec

c. 72 °C for 10 min

3. The PCR products were electrophoresed in 2% agarose gel and then digitally imaged with the Syngene InGenius LHR2 Gel Imaging System (Frederick, MD). Example images are shown below:

S14A:

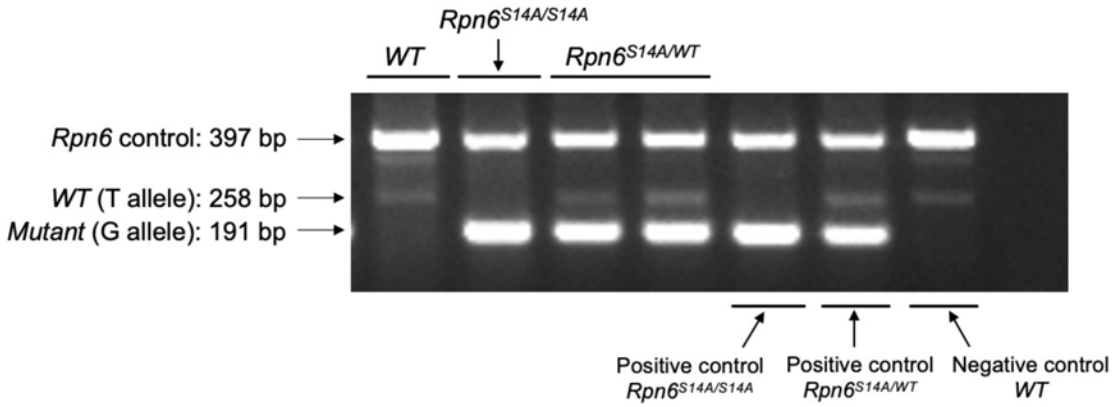

S14D:

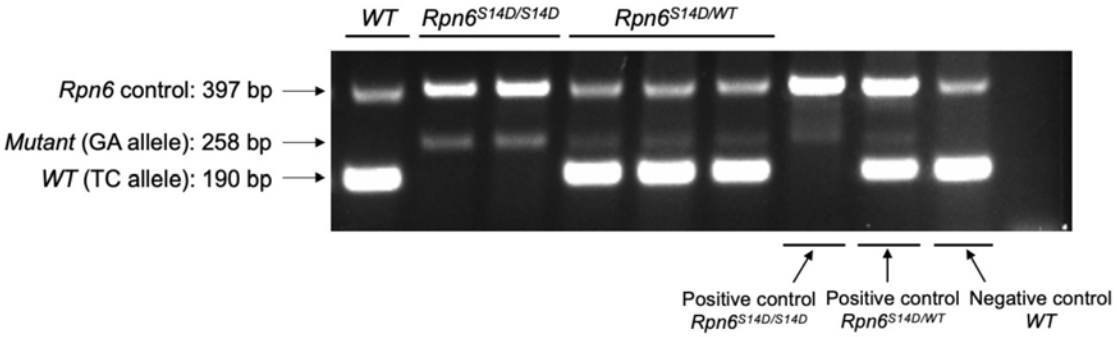

APPENDIX II

Mouse Embryonic Fibroblast (MEF) Isolation, Cell Culture, and Passaging

This protocol for MEF isolation is modified from the protocol created by Xu.[182]

I. Materials

1. 100% Avertin stock solution: 5 g 2,2,2-tribromoethanol + 5 ml *tert*-amyl alcohol

   Dilute the stock solution to 2.5% working solution in sterile PBS.

   Both 100% and 2.5% Avertin can be stored at 4°C for up to 6 months, protected from light.

2. Sterile PBS
3. 0.25% trypsin-EDTA (Cat#25-053-CI, CORNING, Corning, NY)
4. MEF media: filter-sterile, store at 4°C for up to 3 months
   - DMEM (Dulbecco's modified Eagle medium; Cat#SH30243.02, Cytiva, Marlborough, MA)
   - 10% FBS
   - 0.1 mM β-mercaptoethanol
   - 50 U penicillin
   - 50 μg/ml streptomycin

II. Procedure

1. <u>MEF isolation</u>

   1) Sterilize the surgical instruments.

   2) Anesthetize the pregnant mouse on day E14.5 by i.p. injecting 0.5 ml of 2.5% avertin. Euthanize it by cervical dislocation.

   3) Spray the whole mouse body with 70% ethanol.

4) Cut a small incision through the skin at the centric position on the middle back to open the abdominal cavity.
5) Carefully dissect out the entire uterus containing all embryos without interfering other internal organs.
6) Transfer the uterus to a 50 ml tube containing 30 ml sterile PBS. Invert the tube several times to wash the uterus.

The following procedure must be carried out in a laminar flow cabinet.

7) Transfer the washed uterus to a 100 mm dish containing 10 ml PBS.
8) Cut through one side of the uterine wall and expose the embryos.
9) Open the yolk sac and dissect out all fetuses intact. Place them in a new 100 mm dish with 10 ml PBS.
10) Remove the viscera and head. Wash the remaining part of each fetus in PBS to wash out blood as much as possible.
11) Transfer the washed fetuses to a new 60 mm dish containing 2-3 ml ice-cold 0.25% trypsin-EDTA.
12) Tease all fetuses into fine pieces. Transfer all materials to a new 50 ml tube with a 1000 μl pipette. Add 0.25% trypsin-EDTA to bring the total volume to 25 ml (or 3 ml per embryo).
13) Place the tube at 4 °C overnight.
14) One the following day, aspirate half of the trypsin solution away without disturbing the tissue at the bottom of the tube. Incubate the tube in the 37°C water bath for 30 min.

15) After incubation, add 25 ml MEF media to the tube and pipette vigorously. Allow sedimentation of the cell suspension by gravity for ~1 min.

16) Transfer the supernatant cell suspension to a new 50 ml tube.

17) Mix the cell suspension and plate the cells with additional MEF media in T75 culture flasks. Agitate the flasks to ensure even distribution.

18) After overnight Incubation in the 37°C incubator supplied with 5% CO_2, Aspirate the media and wash the cells with sterile PBS twice to remove non-adherent cells.

19) Add 15 ml fresh MEF media to each flask and continue to culture the cells to near confluency. The cells at this stage are designated as Passage 1 MEFs.

20) Change the media every 48 hr.

2. Cell splitting

1) Once the cells reach ~75% confluency, prepare to split the cells:

- 1x T75 flask → 5x T75 flasks
- 0.25% trypsin-EDTA (warmed in 37°C water bath)
- MEF media (warmed in 37°C water bath)
- Sterile PBS (warmed in 37°C water bath)

2) Aspirate the media from the cell flask. Wash the cells with PBS (~10 ml).

3) Apply the 0.25% trypsin-EDTA to the cells with a volume just fully covering the surface.

4) Agitate and swirl the liquid around the flask. Incubate the flask in the 37°C incubator for 5 min.

5) Inspect under a microscope to confirm the detachment of nearly all cells.

6) Add MEF media (2x volume of trypsin-EDTA) to the flask. Pipette the media down the surface several times to wash off all cells.
7) Transfer the cell suspension to an appropriate sized tube.
8) Spin down in the centrifuge for 5 min at 239 x g at 4°C.
9) Carefully discard the supernatant without disturbing the cell pellets.
10) Fully resuspend the cells in appropriate amount of MEF media (~15 ml per T75 flask).
11) Seed the cells into new flasks evenly between flasks and continue to culture the cells to near confluency. The cells at this stage are designated as Passage 2 MEFs.
12) Repeat the splitting procedure to achieve more passages.
13) MEFs after the 6^{th} passages are used for experimentation.

APPENDIX III

Adult Mouse Cardiomyocytes (AMCMs) Isolation and Cell Culture

This protocol for AMCM isolation is modified from the protocol created by Ackers-Johnson et al..[183]

I. Buffers and media constituents

1. EDTA buffer

Compound	Molar mass (g/mol)	Final concentration (mmol/l)	g / L required
NaCl	58..44	130	7.5972
KCl	74.55	5	0.37257
NaH_2PO_4	119.98	0.5	0.05999
HEPES	238.3	10	2.383
Glucose	180.16	10	1.8016
BDM*	101.1	10	1.011
Taurine	125.15	10	1.2515
EDTA	292.24	5	1.4612

*BDM: 2,3-butanedione monoxime
Make in 1 L deionized water (ddH_2O). Adjust to pH 7.8 using NaOH. Sterile filter.

2. Perfusion buffer

Compound	Molar mass (g/mol)	Final concentration (mmol/l)	g / L required
NaCl	58..44	130	7.5972
KCl	74.55	5	0.37257
NaH_2PO_4	119.98	0.5	0.05999
HEPES	238.3	10	2.383
Glucose	180.16	10	1.8016
BDM	101.1	10	1.011
Taurine	125.15	10	1.2515
$MgCl_2$	95.2	1	0.095

Make in 1 L ddH_2O. Adjust to pH 7.8 using NaOH. Sterile filter.

3. Collagenase buffer

Enzyme	Stock concentration (mg/ml)	Final concentration (mg/ml)
Collagenase 2	50	0.5
Collagenase 4	50	0.5
Protease XIV	50	0.05

Make stock buffers, filter sterilized, protect from light, and store in aliquots at -80°C for at least ~4 months:

100x (= 50 mg/ml) collagenase 2 in ddH_2O

100x (= 50 mg/ml) collagenase 4 in ddH_2O

1000x (= 50 mg/ml) protease XIV in ddH_2O

Prepare Collagenase buffer by dilution in Perfusion buffer. Make fresh immediately before cell isolation.

4. Stop buffer

Stop buffer = Perfusion buffer + 5% sterile FBS. Make fresh on the day of isolation.

5. Media constituents

- 100x (= 1 mol/l) BDM stock in ddH_2O, filter sterilized, store in aliquots at -20°C
- 50x (= 5% w/v) BSA stock in PBS, filter sterilized, store in aliquots at 4°C, and keep sterile
- M199 media used here is supplied with l-glutamine already included. Ensure l-glutamine addition if using different suppliers.
- Penicillin/Streptomycin (P/S) antibiotic addition is optional.

6. Plating media

Compound	Stock concentration	Final concentration	ml / 100 ml media
M199		-	93
FBS	100%	5%	5
BDM	1 mol/l (100x)	10 mmol/l	1
P/S	100x	1x	1 (Optional)

Filter sterile, store at 4°C, and keep sterile.

7. Culture media

Compound	Stock concentration	Final concentration	ml / 100 ml media
M199		-	96
BSA	5% (50x)	0.1%	2
ITS*	100x	1x	1
BDM	1 mol/l (100x)	10 mmol/l	1
CD lipid[#]	100x	1x	1
P/S	100x	1x	1 (Optional)

*ITS: Insulin, transferrin, selenium; [#]CD lipid: Chemically defined lipid concentrate
Filter sterile, store at 4°C, and keep sterile. Protect from light.

8. Calcium reintroduction buffers

Solution	ml for Buffer 1	ml for Buffer 2	ml for Buffer 3
Perfusion buffer	15	10	5
Culture Media	5	10	15

For total volume of 20 ml per calcium reintroduction buffer. Make fresh on the day of isolation.

II. Procedure

1. Pre-coating

    1) Make laminin: 15 μg/ml in PBS

    2) Precoat the dishes with laminin for at least 1 hr in the 37°C. Precoated dishes are best prepared fresh but may be sealed and stored at 4°C for up to 4 days.

2. Prepare buffers, media, equipment, and surgical area

    3) Prepare the buffers and media and sterilize them using a 0.2 μm filter under sterile conditions. Media, EDTA and Perfusion buffers are stable for up to 2 weeks at 4°C, protected from light.

    4) Warm the media in the 37°C water bath.

    5) Make Collagenase buffer and warm it in the 37°C incubator immediately before isolation. All other buffers are used at room temperature.

    6) Isolation of one heart requires ~30 ml EDTA buffer, ~15 ml Perfusion buffer, up to 60 ml Collagenase buffer, and 10 ml Stop buffer.

    7) For one heart:

        - 3x 60 mm dishes (one for EDTA buffer, one for Perfusion buffer, one for Collagenase buffer)
        - 5x 10 ml syringes (2x EDTA buffer, 1x Perfusion buffer, 2x Collagenase buffer)
        - 1x needle with a catheter
        - 1x clamp

    8) Sterilize surgical instruments and spray the surgical area with 70% ethanol.

3. Surgical procedure

    9) Anesthetize the mouse with 2% inhaled isoflurane.

    10) Wipe the mouse chest with 70% ethanol. Open the chest and expose the heart.

    11) Cut the descending aorta and inferior vena cava.

    12) Inject 7 ml EDTA buffer into the base of the right ventricle (RV) steadily within ~1 min to flush out blood. Contraction will quickly cease and the heart is visibly lighter in color.

13) Clamp the ascending aorta with a haemostatic clamp.
14) Remove the clamped heart and submerge it in a 60 mm dish with EDTA buffer (~10 ml).
15) Inject 10 ml EDTA buffer through the LV wall 2-3 mm above the apical point within ~6 min, to clear the coronary circulation. Areas of the heart will become pale.
16) Transfer the heart to a 60 mm dish with Perfusion buffer (~10 ml).
17) Inject 3 ml Perfusion buffer into the LV via the same perforation left by the previous injection within ~2 min, to clear EDTA from the heart chambers and circulation.

4. Tissue digestion

18) Digestion must be carried out in a laminar flow cabinet.
19) Transfer the heart to a 60 mm dish containing pre-warmed Collagenase buffer (~10 ml).
20) Inject the LV sequentially through the same point with 2 syringes of Collagenase buffer with a flow rate of ~2 ml/min (can increase as the procedure progresses). Make sure the heart is always submerged.
21) The buffer can re-cycle during the digestion. The volume of Collagenase buffer for complete digestion varies between hearts, normally 25-50 ml.
22) Observe the signs of complete digestion, including a noticeable reduction in resistance to injection pressure, loss of shape and rigidity, holes and/or effluent buffer.
23) The complete digestion process takes ~1.5 hr.
24) After digestion, remove the clamp and atria and connective tissue. Transfer the ventricle to the lid of the same 60 mm dish containing 3 ml unused Collagenase buffer.

25) Gently separate the tissue into pieces (not too small) with forceps. Pipette the ventricle particles with a wide-bore 1000 μl pipette for 2 min.

26) Add 5 ml Stop buffer to the cell-tissue suspension and pipette the suspension for a further 2 min.

27) Inspect under the microscope to confirm yields of rod-shaped cardiomyocytes.

28) Transfer the cell suspension to a new, sterile 50 ml tube, filtered with a 100 μm cell strainer.

29) Add another 5 ml Stop buffer through the filter.

30) Divide the cell suspension into two new, sterile 15ml tubes. Let the cells to settle by gravity for 20 min at room temperature.

5. Cell collection and plating

31) During gravity settling, make Calcium reintroduction buffers 1/2/3, 2 ml each.

32) The pellets contain cardiomyocytes.

33) Add Calcium reintroduction buffers in gradual increment of calcium content to the pellets. Allow gravity settling for 10 min after adding Buffers 1 and 2, and for 20 min (or until visualization of pellets settle down) after Buffer 3.

34) Discard the supernatant. Resuspend the final cell pellets in 1 ml pre-warmed Culture.

35) Add appropriate volume (~2 ml generally) of Plating media according to experiment-desired densities.

36) Aspirate laminin away from the prepared dishes. Wash once with PBS.

37) Plate cells on the coated dishes (2x 35 mm dish per heart generally). Agitate the dishes gently in a side-to-side motion to evenly distribute the cells.

38) Allow adhesion for 3 hr in the 37°C incubator.

39) Wash the cells with Culture media once, and incubate them in Culture media in the 37 incubator for another 48 hr prior to further experiments.

III. Reagent suppliers

Item name	Company	Catalogue number
NaCl	Fisher Chemical	S271-10
KCl	Fisher Chemical	P330-500
NaH_2PO_4	Sigma-Aldrich	S8282
HEPES	Sigma-Aldrich	H3375
Glucose	Sigma-Aldrich	G8270
BDM	Sigma-Aldrich	B0753
Taurine	Sigma-Aldrich	T8691
EDTA	ACROS ORGANICS	118430010
$MgCl_2$	ACROS ORGANICS	7786-30-3
Collagenase 2	Worthington	LS004176
Collagenase 4	Worthington	LS004188
Protease XIV	Sigma-Aldrich	P5147
Laminin	Thermo Scientific	23017-15
M199 Medium	Sigma-Aldrich	M4530
ITS	Sigma-Aldrich	I3146
CD lipid	Thermo Scientific	11905-031
P/S	Thermo Scientific	15070-063

APPENDIX IV

Isolation and Culture of Neonatal Rat/Mouse Cardiomyocytes (NRCMs/NMCMs)

I. Kit used: Cellutron neonatal rat/mouse cardiomyocyte isolation kit (Cat#: nc-6031, Cellutron Life Technology, Baltimore, MD)

II. Prepare the following before the experiment

Pre-warm Surecoat solution Put the stirrer in the 37°C incubator and plug in.	
D1 working solution	5 ml D1 + 45 ml ice-cold ddH_2O
D2 working solution	20 ml D2 + 28 ml ddH_2O + 2 ml enzyme complex (EC)
D3 working solution	15 ml D3 + 15 ml NS media (for 5-15 hearts) 15 ml D3 + 25 ml NS media (for 16-35 hearts)
Precoat the dishes by adding 1 ml Surecoat per 35 mm dish	

III. Procedure

1. Sterilize neonatal rats or mice with 70% ethanol. Quickly remove the hearts of the rat/mouse pups (rats at P2 or mice at P1) and put them into the 100 mm dish that contains 25 ml ice-cold D1. Trim the connective tissue and atria away. Transfer the ventricles to another dish that contains 25 ml ice-cold D1. Rinse the tissue.
2. Transfer the ventricles to a 30 ml beaker with a stir bar. Add digestion buffer D2+EC (6 ml for 5-15 hearts or 7 ml for 16-35 hearts). Set the stirring speed at ~ 150 rpm. Stir the hearts in the 37 °C incubator for 12 min.
3. Pipette the tissue up and down and transfer the supernatant to a new sterile 15 ml round bottom tube and spin at 153 x g at 4 °C for 1 min (for rats) or 2 min (for mice).

4. Carefully discard the supernatant and resuspend the cell pellets in appropriate ml of D3 (generally 3 ml for digestion cycle 1-2, 6 ml for digestion cycle 3-4, and 3 ml for digestion cycle 5-7). Keep the cells at room temperature.
5. Repeat step 2 - 4 until all the tissue is digested (generally 6-8 cycles).
6. Filter the cells with a 100 μm cell strainer.
7. Preplate the cells for 1-2 hr by seeding 3 uncoated 100 mm dishes in the 37°C incubator.
8. Suck away the precoated Surecoat solution in the dishes.
9. Transfer the unattached cells to a new 50 ml tube.
10. Filter the cells again through a 70 μm cell strainer into a new 50 ml tube.
11. Count the cell number using a hemocytometer.
12. Dilute cells at the appropriate densities with DMEM supplemented with 10% FBS and 1x Antibiotic Antimycotic Solution (Cat#30-004-CI, CORNING, Corning, NY). Plate cells on the coated dishes. Swirl the dishes gently to evenly distribute the cells.
13. After 24 hr of plating, change the medium according to experiment needs.

APPENDIX V

Total Protein Preparation from Cultured Cells and Myocardial Tissue for SDS-PAGE

Cultured cell collection

1. Wash the cultured cells twice with cold PBS.
2. For 35 mm cell culture dishes, add 60 µl of 1x Sampling Buffer to the cells and scrape the cells off.

Heart tissue collection

1. Anesthetize the animal with 2% inhaled isoflurane. Open the chest and cut out the heart out. Wash the heart in cold PBS and trim off the atria and connective tissue.
2. Take one-third of the ventricle and snap freeze in liquid nitrogen. Store the sample at -80 °C until further use.
3. For preparation of proteins from either fresh or snap frozen tissue, add 100 µl of 1x Sampling Buffer per 10 mg tissue.

1x Sampling Buffer: stored at room temperature

ddH_2O	28.5 ml
3 M Tris-HCl pH 6.8	0.5 ml
10% SDS	4.5 ml
Glycerol	3 ml

*Add 1x complete Protease and Phosphatase Inhibitor Cocktail (Cat#HB9105, Hello Bio Inc., Princeton, NJ) freshly

Total protein preparation

1. For efficient protein extraction, crush the tissue into powder.

2. Extensively vortex the mixture of sampling buffer and cells; or pulverize the mixture of sampling buffer and tissue with a pellet pestle.
3. Boil the homogenates for 5 min in the 95 °C water bath.
4. Centrifuge at 10,621 x g for 10 min at 4°C. Collect the supernatant.

Protein concentration determination

Bicinchoninic acid (BCA) method: Pierce BCA Protein Assay Kit (Cat#23222 & #23224, ThermoFisher Scientific, Waltham, MA)

1. Dilute each sample in ddH_2O to 1:20.
2. In a 96-well microplate with conical bottom, each well is loaded with 20 µl of a diluted sample. For more accuracy, load each sample in duplicate or triplicate.
3. Run parallel analysis of a series of known concentrations of BSA for the generation of the standard curve.
4. Load 200 µl of the mix solutions of Reagent A and B (50:1 ratio) from the BCA kit in each well.
5. Incubate the samples in the 37 °C incubator for 30 min.
6. Read samples in a Perkin Elmer plate reader (Model VICTOR Nivo™, Waltham, MA) and measure absorbance at 562 nm.
7. Use the absorbance to extrapolate the protein concentration of the sample from the standard curve.

Sample preparation for SDS-PAGE

1. Add 3x Loading Buffer to each aliquot of protein sample.
2. Boil samples in the 95 °C water bath for 5 min. Cool down the samples followed by short centrifugation to get the samples into the bottom of the tube before loading on to the gel.

3x Loading Buffer: stored at room temperature indefinitely.

1 M Tris-HCl pH 6.8	2.4 ml
20% SDS	3 ml
Glycerol	3 ml
Bromophenol blue	0.01%

*Add β-mercaptoethanol at 84:16 fresh

APPENDIX VI

NP-40 Soluble and Insoluble Protein Fractionation

I. Buffers

Lysis Buffer

50 mM	Tris-HCl pH 8.8
100 mM	NaCl
5 mM	$MgCl_2$
0.5% (v/v)	NP-40
* 2 mM	DTT
* 1x	Protease and Phosphatase Inhibitor Cocktail

Pellet Buffer

20 mM	Tris-HCl pH 8.0
15 mM	$MgCl_2$
* 2 mM	DTT
* 1x	Protease and Phosphatase Inhibitor Cocktail

3x SDS Boiling Buffer

6%	SDS
20 mM	Tris-HCl pH 8.0
* 150 mM	DTT

* Add freshly

II. Procedure

1. Make fresh complete buffers.

2. Collect cultured cells or ventricular tissue as described in Appendix V. Lysate tissue/cells in 100 µl ice-cold Lysis Buffer.
3. Homogenize the samples as described in Appendix V. Incubate the samples on ice for 30 min.
4. Centrifuge at 17,000 x g for 15 min at 4 °C.
5. Collect the supernatant. → NP-40 soluble (NS) fraction
6. Rinse the pellets by gently adding ~200 µl ice-cold PBS w/o disturbing pellets (5 times).
7. Remove PBS. Suspend the pellets, containing NP-40 insoluble (NI) fraction, in 100 µl ice-cold Pellet Buffer.
8. Homogenize the samples with a pellet pestle and incubate on ice for 30 min.
9. Add 50 µl (1/3 of total volume) 3x SDS Boiling Buffer into NS and NI tubes.
10. Boil the samples in the 95 °C water bath for 5 min, or until NI pellets are completely dissolved.
11. Determine the protein concentration, using a Reducing Agent-Compatible BCA Protein Assay Kit (Cat#23252, Thermo Fisher Scientific, Waltham, MA).
12. Prepare the samples for SDS-PAGE in the same way for total protein samples.

Reducing Agent-Compatible BCA assay:

1. Mix the Reconstitution Buffer 1:1 with ddH_2O to make Working Reconstitution Buffer.
2. Dissolve the Compatibility Reagent in the Working Reconstitution Buffer. (1 tube of reagent in 100 µl Reconstitution Buffer)
3. Prepare the BCA standard samples and diluted unknown protein samples as described in Appendix V.

4. In a 96-well microplate with round bottom, each well is loaded with 9 µl of a BCA standard sample or a diluted unknown sample mixed with 4 µl of the Compatibility Reagent Solution. For more accuracy, load each sample in duplicate or triplicate.
5. Incubate the microplate in the 37 °C incubator for 15 min.
6. Then load 260 µl of the mix solutions of Reagent A and B (50:1 ratio) from the BCA kit in each well.
7. Incubate the samples in the 37 °C incubator for 30 min. Cool down at room temperature for 5 min.
8. Read samples in a Perkin Elmer plate reader and measure absorbance at 562 nm.
9. Use the absorbance to extrapolate the protein concentration of the sample from the standard curve.

APPENDIX VII

Western Blot Analysis

I. Stock solutions and buffers

1. Gel casting recipe

For 2 resolving gels:

Reagent	8%	10%	12%	14%	16%	18%
ddH_2O	9.4 ml	7.9ml	6.6 ml	5.4 ml	4.2 ml	2.8 ml
1.5 M Tris-HCl pH 8.8	5 ml	5 ml	5 ml	5 ml	5 ml	5 ml
10% SDS	200 µl	200 µl	200 µl	200 µl	200 µl	200 µl
30% Bis Acrylamide	5.4 ml	6.7 ml	8.0 ml	9.4 ml	10.6 ml	12.0 ml
10% APS	100 µl	200 µl	200 µl	100 µl	100 µl	100 µl
TEMED	10 µl	8.5 µl	8.5 µl	10 µl	10 µl	10 µl
2,2,2-Trichloroethanol	100 µl	100 µl	100 µl	100 µl	100 µl	100 µl

For 2 stacking gels:

Reagent	
ddH_2O	5.5 ml
1 M Tris-HCl pH 6.8	1 ml
10% SDS	80 µl
30% Bis Acrylamide	1.3 ml
10% APS	80 µl
TEMED	8.3 µl

2. 10X TBS (Tris-Buffered Saline):

   24 g Tris base

   88 g NaCl

   Adjust pH to 7.6 with HCl, add ddH_2O to bring the final volume to 1 L

3. TBST (per liter):

100 ml 10X TBS

900 ml ddH_2O

2 ml Tween 20 (detergent)

4. 10X Transfer Buffer (per liter)

   30.3 g Tris base

   144 g Glycine

5. 1X Running Buffer

   100 ml 10X Transfer Buffer

   900 ml ddH_2O

   10 ml of 10% SDS

6. 1X Transfer Buffer (Keep chilled)

   100 ml 10X Transfer Buffer

   200 ml Methanol

   700 ml ddH_2O

7. Blocking Buffers

   2% BSA: 2 g BSA in 100 ml TBST, or

   2% ECL™ advanced blocking agents (Cat#RPN418, Cytiva, Marlborough, MA): 2 g agent in 100 ml TBST

II. Western blot procedure

Gel making and running:

1. Set up the casting frame with a short place, spacer plate, and combs to make the appropriate percentage of gel (low percentage for high molecular weight proteins and high percentage of gel for low molecular weight proteins).
2. Load the revolving gel solution in-between the plates up to 3-5 mm below where the tip of comb teeth would be. Allow gel to polymerize at room temperature.
3. Prepare and load the stacking gel solution on top of the revolving gel with an appropriately sized comb between the glass plates.
4. After the gel is settled, remove the gel cassette sandwich from the casting stand and place it in the clamping frame of the running tank, with the short plate facing the inside. Fill the inside of the plates and some outside with 1X Running Buffer.
5. Start to boil the protein samples in the 95 °C water bath for 5 min, and then spin down.
6. Remove combs from the gel. Load the first outside well with the ladders, Precision Plus Protein dual color standards (Cat#1610374, Bio-Rad, Hercules, CA) and load the remaining wells with the protein samples.
7. Plug in the color-coded leads into the power supply and run the gels for the appropriate amount of time at 100 V.

Protein transfer from gel to membrane:

8. Prepare PVDF membrane and filter paper to the size of the gel. Soak the membrane in methanol for 5 min, followed by soaking the membrane, filter paper, and filter pads in the transfer buffer.
9. After gel running is done, remove the gel from the plates by carefully taking off the short plate and cutting along the edges of the gel, and rinsing the gel with water.

10. Stain-free technology was then used to take a protein image of the gel. Activate the gel by exposure to UV light for 45 sec and visualize the total protein loading in the ChemiDoc™ MP imaging system (Bio-Rad, Hercules, CA).
11. Arrange the sandwich from bottom to top; lay the black side, filter-pad, filter paper, gel, membrane, filter-paper, filter-pad, and clear side, and roll out any bubbles with a pipet or a roller over the filter paper.
12. Place the sandwich casting in the transfer cassette with the gel facing black (-) and membrane facing red (+).
13. Slide the cassette into the transfer box, add an ice pack, and put them in an ice-filled tub.
14. Fill the transfer tank with 1X Transfer Buffer. Run at constant 250 mA for 140 minutes or constant 40 mA overnight.
15. Disconnect the leads from the power source and remove the membrane while keeping the membrane protein side up. Alternatively, use the ChemiDoc™ MP imaging system to take stain-free blot images for total protein.

Immunoblotting:

16. Rinse the membrane once in TBS for 5 minutes and twice in TBST for 5 minutes each, followed by blocking with gentle rocking at room temperature in an appropriate blocking buffer for 1 hr.
17. Incubate the membrane with the primary antibody at a proper dilution in the appropriate blocking buffer overnight with gentle rocking.
18. Wash the membrane at least three times in TBST for 5 minutes each.
19. Incubate the membrane with the secondary antibody (1:10,000 dilution in the blocking buffer) at room temperature for 1 hr.

20. Wash the membrane at least three times in TBST for 5 minutes each.
21. Mix solution A and solution B of the ECL chemiluminescent reagents, SuperSignal™ West Pico PLUS Chemiluminescent Substrate (Catalog#34578, ThermoFisher Scientific, Waltham, MA) at 1:1 ratio. Make volume enough to cover the blot.
22. Place the PVDF membrane face up on a clean glass plate inside the ChemiDoc™ MP imaging system and cover it with ECL mixtures. Set up the imaging system appropriately to expose the blot.
23. Utilize Image lab 6.0 to perform densitometry and quantification of the Western blot.

APPENDIX VIII

Proteasome Peptidase Activity Assays

I. Stock solutions:

1. Stock Protein Extraction Buffer (store at 4 °C)

   50 mM Tris-HCl pH 7.5

   250 mM Sucrose

   5 mM $MgCl_2$

   0.5 mM EDTA

   *1 mM DTT

   *0.025% Digitonin

   *1x complete protease and phosphatase inhibitor cocktail

   *Add Fresh before use in collecting samples

2. Stock Proteasome Assay Buffer (store at 4 °C)

   50 mM Tris-HCl pH 7.5

   40 mM KCl

   5 mM $MgCl_2$

   *1 mM DTT

   *0.5 mg/ml BSA

   *Add Fresh

3. Other stock solutions (stored in -20 °C):

   - 1 M DTT in water
   - 5% digitonin in DMSO
   - 500 mM ATP in Tris-HCl pH 8.8

- 50 mg/ml BSA in water
- Stock Solutions of substrates in DMSO

  For chymotrypsin-like activity: 1.8 mM Suc-LLVY-AMC (Cat#10008119, Cayman Chemical, Ann Arbor, MI)

  For caspase-like activity: 4 mM Z-LLE-AMC (Cat#10008117, Cayman Chemical, Ann Arbor, MI)

  For trypsin-like activity: 5 mM z-VGR-AMC (Cat#BML-BW9375, Enzo Life Sciences, Farmingdale, NY)
- Proteasome Inhibitors:

  1 M BZM (Cat#B-1408, LC Laboratories, Woburn, MA)

  1 mM epoxomicin (Cat#A2606, APExBIO, Houston, TX)

II. Protein preparation

1. Make complete protein extraction buffer on ice.
2. Collect cultured cells or ventricular tissue as described in Appendix V, with a replacement of 1x sampling buffer by the complete Protein Extraction Buffer.
3. Homogenization: Extensively vortex the mixture of extraction buffer and cells; or pulverize the mixture of extraction buffer and tissue with a pellet pestle.
4. Centrifuge at 6800 x g for 10 min at 4 °C. Collect the supernatant.
5. Determine the protein concentration with BCA reagents.

III. Procedure for proteasome peptidase activity assays

1. Make complete Proteasome Assay Buffer and place it on ice.

2. Make a master mix containing complete Proteasome Assay Buffer with ATP and/or a proteasome inhibitor at appropriate concentrations:
    - For chymotrypsin-like activity: 0.2 mM ATP; 0.28 μM BZM
    - For caspase-like activity: 0.4 mM ATP; 0.28 μM BZM
    - For trypsin-like activity: 0.4 mM ATP; 5 μM epoxomicin
3. Prepare a black 96-well microplate (Cat#655076, Greiner Bio-One, Germany).
4. Load each well with 5 μg sample from cells (or 10 μg from tissue) adjusted in 200 μl master mix with or without a proteasome inhibitor. Samples are loaded in duplicate.
5. Cover the microplate and incubate it for 30 min at 37°C.
6. Set the plate reader's temperature to 37°C.
7. After incubation, add 2 μl substrate specific for desired peptidase activity type to each well.
8. Read samples in a Perkin Elmer plate reader at desired time points.
    - Excitation wavelength -380 nm
    - Emission wavelength -460 nm
9. Subtract sample readings from the blank reading and normalize to proteasome inhibition to determine relative activity specific to the proteasome.
10. Average the measurements from the duplicate and integrate the activity at all time points to draw a reaction time-course curve. The slope of the log phase of the reaction curve indicates the corresponding proteasome activity.

APPENDIX IX

RNA Isolation, Reverse Transcriptase PCR, and Real-time qPCR

I. Isolation of RNA from myocardial tissue

1. Homogenize tissue samples (perform on ice) in pre-cooled TRI Reagent® (Cat#TR 118, Molecular Research Center Inc., Cincinnati, OH) using a Bullet Blender homogenizer (Cat#NA-BT5E, Stellar Scientific, Baltimore, MD). Use 1 ml of reagent for 50-100 mg of tissue. If RNA isolation is not carried out immediately after tissue collection, store the tissue sample in 1 ml of RNA*later*™ Soln. (Ca#AM7024, Invitrogen, Waltham, MA) at 4 °C for up to a week.
2. Allow complete dissociation of nucleoprotein complexes by storing the homogenate in room temperature for 5 min.
3. Transfer the homogenate into a microcentrifuge tube and add 200 µl pre-cooled chloroform to the homogenate for every 1 ml of TRI reagent that was used in the beginning. Cap the tube tightly and shake vigorously for 15 sec. Stand at room temperature for 5 min, until the supernatant appears clear.
4. Centrifuge at 12,000 x g at 4 °C for 15 min.
5. Prepare new microcentrifuge tubes. Add 400 µl (per 1 ml TRI reagent) pre-cooled isopropanol in each tube.
6. Carefully transfer the clear uppermost aqueous phase into the isopropanol-containing tubes. Rotate to precipitate RNA from the aqueous phase by mixing with isopropanol. Stand for 10 min at room temperature.
7. Centrifuge at 12,000 x g at 4 °C for 10 min.

8. Discard the supernatant and wash the RNA pellet with 1 ml of 75% ethanol [in DEPC-treated water (Cat#BP561-1, Fisher Scientific, Waltham, MA)].
9. Sit for 5 min and centrifuge at 7,500 x g at 4 °C for 5 min.
10. Discard the supernatant and air dry the pellet for 3-5 minutes.
11. Store the RNA pellets in DEPC-treated water at -80 °C until further use.

II. Reverse Transcriptase-PCR (RT-PCR)

1. Determine the RNA concentrations with a NanoDrop 2000 UV Spectrophotometer (Thermo Scientific, Waltham, MA).
2. Dilute RNA samples with DEPC-treated water to make equal concentration of each sample (500-1000 ng RNA per 10 µl sample).
3. A High Capacity cDNA Reverse Transcription Kit (Cat#4368814, Applied Biosystems, Waltham, MA) is used to generate cDNA. Mix and briefly centrifuge each component before use.
4. Make RT-PCR master mix. For each sample, add the following components in each new PCR tubes:

Component	Amount
10x RT Buffer	2 µl
25x DNTP	0.8 µl
10x RT Random Primer	2 µl
Reverse Transcriptase	1 µl
DEPC-treated water	4.2 µl
RNA sample	10 µl

5. Mix gently and collect by brief centrifugation. Incubate in the Techne 5PRIMEG/02 Thermal Cycler using the following program:
    a. 25 °C for 10 min
    b. 37 °C for 120 min
    c. 85 °C for 5 min
6. Collect the mixture by brief centrifugation.
7. The cDNA synthesis reaction can be stored at -80 °C or used for further experiments.

III. Quantitative real-time PCR (qPCR)

1. PowerUp™ SYBR™ Green Master Mix (Cat#A25742, Applied Biosystems, Waltham, MA) is used for qPCR analysis. The entire procedure must be conducted on ice.
2. Thaw the Master Mix, cDNA samples, and primers on ice. Dilute the samples 1:10 in DEPC-treated water.
3. For each sample, mix well the following components in each well of a MicroAmp® Fast 96-Well Reaction Plate (Cat#4346907, Applied biosystems, Waltham, MA):

Component	Amount
SYBR™ Green Master Mix	10 µl
Forward Primer	0.4 µl
Reverse Primer	0.4 µl
DEPC-treated water	7.2 µl
Diluted cDNA sample	2 µl

4. Seal the microplate with an adhesive film.
5. Incubate in the StepOnePlus Real-Time PCR system (Applied Biosystems, Waltham, MA) with the following profile:

a. 50 °C for 2 min

b. 95 °C for 10 min

c. 40 cycles of:

   95 °C for 15 sec

   60 °C for 60 sec

6. All reactions for reference (*GAPDH*) and target genes are in duplicate and the average value was used for subsequent quantification.
7. The $2^{-\Delta\Delta Ct}$ method using *GAPDH* as the normalization gene is used to calculate the relative expression of target genes.

APPENDIX X

Immunofluorescence Staining

Sample Fixation

1. Remove the heart, wash in PBS, and place the tissue in the 4% paraformaldehyde for at least 12 hours.
2. Equilibrate the tissue in a gradual increment of sucrose (by varying mixtures of 10% and 30% sucrose).
3. Embed the heart tissues in the Tissue-Tek O.C.T in a Cryomold. Place the mold on top of the aluminum plate on the dry ice-methanol bath for rapid freezing and wait until the OCT is completely frozen.
4. Cut the frozen tissue block with a -20 °C cryostat. Place the 7-µm thick sections on charged glass slides for further use. Otherwise store the tissue block at -80 °C for future use.

Immunostaining for fixed cryosections

1. Permeabilize the cryosections with 0.1% Triton X-100 in PBS for 15 min at room temperature.
2. Quench the cryosections with 1% glycine in PBS for 1 hr. Wash 3 times with PBS.
3. Block the cryosections with 2% BSA in PBS for 1 hr.
4. Incubate the cryosections with primary antibody at proper dilution in 2% BSA at 4 °C in a moist chamber overnight.
5. Wash at least three times with PBS to remove any unbound primary antibody.
6. Add a secondary antibody (in 2% BSA) and incubate in a moist chamber for 1 hr at room temperature. Then wash at least 3 times in PBS.

7. Mount the cryosections with DAPI. Seal the edges of the coverslip with nail polish and store them in the -20 °C freezer until ready to take the image.

Solutions

1. 4% Paraformaldehyde (PFA)
    1) Heat a volume of ddH_2O approximately 2/3 of the final desired volume to 60 °C.
    2) For 100 ml final volume, weigh 4 g of PFA powder (Cat#41678-0010, Thermo Scientific, Waltham, MA).
    3) Add PFA powder to ddH_2O. Cover and stir with a magnetic stirrer at 60 °C.
    4) Add 1 drop of 2N NaOH (1 drop per 100 ml). Wait until the solution become almost clear. Do not heat the solution above 70 °C, otherwise PFA will break down.
    5) While waiting, make 10X PBS: 0.96 g 1X PBS powder + 10 ml ddH_2O.
    6) Remove from heat and add 10 ml (1/10 of final volume) 10X PBS.
    7) Adjust pH to 7.2 with HCl. Add ddH_2O to final volume.
    8) Filter and cool down to 4 °C before use. Cover with foil to protect from light.
2. Sucrose

    10%: 10 g Sucrose in 100 ml PBS

    30%: 30 g Sucrose in 100 ml PBS
3. 1% Glycine: 1 g Glycine in 100 ml PBS
4. 0.1% Triton X-100: 100 µl Triton X-100 + 100 ml PBS
5. 2% BSA: 2 g BSA in 100 ml PBS

APPENDIX XI

Native Gel Electrophoresis Followed by Immunoblotting

I. Stock solutions and buffers

1. 1 M Tris, pH 7.5:

   Dissolve 121.14g Tris base into 900 ml ddH_2O. Adjust pH to pH 7.5 with HCl. Add ddH_2O to 1 L and autoclave. Can be stored at room temperature indefinitely.

2. 2 M NaCl:

   Dissolve 116.88 g NaCl into 1 L ddH_2O. Can be stored at room temperature indefinitely.

3. 1 M $MgCl_2$:

   Dissolve 95.21 g $MgCl_2$ into 1 L ddH_2O. Can be stored at 4 °C indefinitely.

4. 500 mM ATP in Tris, pH 7.0 25 ml

   ATP, disodium salt trihydrate 7.566 g

   2 M Tris base 15 ml

   Dissolve ATP as much as possible in 15 ml of Tris base. Continue to add Tris base dropwise while stirring until ATP is completely dissolved. Determine the pH and adjust to 7.0 with additional Tris base or HCl until pH = 7.0. Bring the final volume to 25 ml using ddH_2O. Make aliquots and store them at -80 °C.

5. Protein Extraction Buffer: make freshly on the day of use.

50 mM	Tris-HCl pH 7.5
250 mM	Sucrose
5 mM	$MgCl_2$
1 mM	ATP
1 mM	DTT

1x Protease and Phosphatase Inhibitor Cocktail

6. 4X Native Gel Loading Buffer: can be stored at room temperature indefinitely.

   200 mM Tris-HCl pH 6.8

   60% (v/v) Glycerol

   0.05% (w/v) Bromophenol blue

7. 4X Separating Gel Buffer (TBE): can be stored at room temperature indefinitely.

   360 mM Tris pH 8.3

   320 mM Boric acid

   * 0.4 mM EDTA

   * Add freshly on the day of use

8. 10X MAD: make freshly on the day of use.

   50 mM $MgCl_2$

   10 mM ATP

   10 mM DTT

9. Electrophoresis Buffer: 1X TBE + 1X MAD + ddH_2O

10. Blotting Buffer: can be stored at room temperature indefinitely

    25 mM Tris base

    192 mM Glycine

    20% Methanol

    0.1% SDS

11. Native gel casting recipe

For 1 Separating gel (4%):

Reagent	
4X TBE	3.75 ml
30% Bis Acrylamide	2 ml
10% Sucrose	3.75
10X MAD	1.5 ml
ddH_2O	4 ml
10% APS	50 µl
TEMED	10 µl
2,2,2-Trichloroethanol	50 µl

For 3 Stacking gels (2.5%):

Reagent	
1 M Tris-HCl pH 6.8	500 µl
30% Bis Acrylamide	830 µl
ddH_2O	8.7 ml
500 mM ATP pH 7.0	20 µl
10% APS	50 µl
TEMED	10 µl

1) Set up the gel casting system.
2) Make separating gels. Mix well and fill in the solution to the glass plates. Carefully overlap it with ddH_2O.
3) Let the gel polymerize for at least 45 min.
4) Make stacking gels.

5) Pour off the water over layering the gel, rinse with water, dry it, and fill in the stacking gel solution up to the top of the glass plates. Insert the well forming comb between the glass plates.
6) Let the stacking gel polymerize for at least 30 min.
7) Remove the comb and fill the slots with Electrophoresis Buffer.

II. Procedure for Native gel electrophoresis

1. Crush the myocardial tissue into powder.
2. Pulverize the mixture of Native Protein Extraction Buffer and tissue with a pellet pestle. Incubate the homogenates on ice for 30 min.
3. Centrifuge at 15,000 x g for 30 min at 4 °C. Collect the supernatant.
4. Determine protein concentration with BCA reagents. Dilute the samples to comparable concentration with the Protein Extraction Buffer and then add 4X Native Gel Loading Buffer.
5. Load the samples on the gel, connect the power supply to the gel apparatus and run the electrophoresis at 4 °C at a constant voltage of 100 V for 4-4.5 hr.
6. Remove the gel from the glass. Soak the entire gel in the Blotting Buffer for 10 min before transfer.
7. The protein is transferred to a PVDF membrane at a constant 250 mA for 90 min, or constant 40 mA overnight. The subsequent procedures are the same as in Western blot, as described in Appendix VII.

APPENDIX XII

Transthoracic Echocardiography

1. After weighing the mouse, place and anesthetize the mouse in an induction chamber for approximately 1 min until the sedation (under 4.0% isoflurane).
2. Place the mouse on a warm pad in the supine position and maintain the body temperature around 37 °C. Remove hair from the mouse's chest using hair removal cream. Wipe the area with wet gauze to ensure all hair is removed.
3. Keep the mouse under light anesthesia with isoflurane (1-1.5%) in room air supplemented with 100% oxygen through a nose cone. Limbs are taped to the ECG leads for ECG monitoring. Heart rates are maintained at 400-500 beats per minute (maintain anesthesia for proper heart rate).
4. Place an ample amount of warmed ultrasound gen on the shaved chest.
5. Lower the probe (40-MHz) to the gel until it makes contact, and make sure all areas of the probe are covered with gel and the image is free of bubble interference.
6. Place the probe along the long-axis of LV and record a video image of the heart in the long-axis in B-mode. Ensure that the heart is level from the aortic inflow to the apex and that the probe is adjusted to mid-heart. Drop an M-mode line, transition the computer to M-mode, and record an M-mode video at mid heart.
7. Rotate the probe clockwise to 90° and record a video of the LV short-axis view in B-mode. When in B-mode, optimize the cardiac image for wall clarity and the presence of papillary muscle.
8. Once the imaging is complete, remove the residual ultrasound gel on the chest, and return the mouse to the cage for recovery.

9. After collection, videos are reviewed and measured using Vevo LAB software at an offline location.
10. Short-axis videos are reviewed and analyzed using the LV-Trace function. LV endocardium borders are traced manually and the measurements are averaged over a minimum of 3 cardiac cycles. Further, heart rate is also manually measured to confirm the accuracy of ECG heart rate.
11. Use Vevo LAB software 5.6.0 to measure LV internal diameters (LVID;d and LVID;s) and posterior wall thicknesses (LVPW;d and LVPW;s). Utilize the algorithm developed in Vevo LAB software 5.6.0 to calculate the parameters such as: heart rate (HR), LV volume (LVEDV and LVESV), ejection fraction (EF), fractional shortening (FS), stroke volume (SV), cardiac output (CO), and estimated LV mass.

APPENDIX XIII

Source of Chemicals, Reagents and Kits

Description	Source	Catalog #
Forskolin	LC Laboratories	F-9929
Piclamilast	Tocris	4525
H89	LC Laboratories	H-5239
Bortezomib	LC Laboratories	B-1408
Epoxomicin	APExBIO	A2606
Suc-LLVY-AMC	Cayman Chemical	10008119
Z-LLE-AMC	Cayman Chemical	10008117
Bz-VGR-AMC	Enzo Life Sciences	BML-BW9375
Proteasome and phosphatase inhibitor cocktail	Hello Bio Inc.	HB9105
DreamTaq DNA Polymerase; 10X DreamTaq Buffer (includes 20 mM $MgCl_2$)	Thermo Fisher Scientific	EP0705
Pierce™ bicinchoninic acid (BCA) protein assay reagents	Thermo Fisher Scientific	23225
Reducing agent-compatible BCA protein assay kit	Thermo Fisher Scientific	23252
30% Bis Acrylamide	BioRad	1610158
2,2,2-Trichloroethanol	ACROS ORGANICS	115-20-8
Precision Plus Protein dual color standards	Biorad	1610374
ECL™ advanced blocking agents	Cytiva	RPN418
SuperSignal™ West Pico PLUS Chemiluminescent Substrate	Thermo Fisher Scientific	34578
Cellutron Neomyocytes Isolation System	Cellutron Life Technology	nc-6031
Antibiotic Antimycotic Solution. 100X	CORNING	30-004-CI
RNA*later*™ Soln.	Invitrogen	AM7024
TRI Reagent®	Molecular Research Center Inc.	TR 118
DEPC-treated water	fisher scientific	BP561-1
High Capacity cDNA Reverse Transcription Kit	Applied Biosystems	4368814

PowerUp™ SYBR™ Green Master Mix	Applied Biosystems	A25742
Trypsin-EDTA	CORNING	25-053-CI
Dulbecco's modified Eagle medium (DMEM)	Cytiva	SH30243.02

REFERENCES

1. Dobson CM, Šali A, Karplus M. Protein Folding: A Perspective from Theory and Experiment. *Angew Chem Int Ed Engl*. 1998;37:868-893. doi: 10.1002/(sici)1521-3773(19980420)37:7<868::Aid-anie868>3.0.Co;2-h
2. Hartl FU, Hayer-Hartl M. Molecular chaperones in the cytosol: from nascent chain to folded protein. *Science*. 2002;295:1852-1858. doi: 10.1126/science.1068408
3. Amm I, Sommer T, Wolf DH. Protein quality control and elimination of protein waste: the role of the ubiquitin-proteasome system. *Biochim Biophys Acta*. 2014;1843:182-196. doi: 10.1016/j.bbamcr.2013.06.031
4. Hartl FU, Hayer-Hartl M. Converging concepts of protein folding in vitro and in vivo. *Nat Struct Mol Biol*. 2009;16:574-581. doi: 10.1038/nsmb.1591
5. Wang X, Su H, Ranek MJ. Protein quality control and degradation in cardiomyocytes. *J Mol Cell Cardiol*. 2008;45:11-27. doi: 10.1016/j.yjmcc.2008.03.025
6. Chen B, Retzlaff M, Roos T, Frydman J. Cellular strategies of protein quality control. *Cold Spring Harb Perspect Biol*. 2011;3:a004374. doi: 10.1101/cshperspect.a004374
7. Wang X, Robbins J. Heart failure and protein quality control. *Circ Res*. 2006;99:1315-1328. doi: 10.1161/01.RES.0000252342.61447.a2
8. Muratani M, Tansey WP. How the ubiquitin-proteasome system controls transcription. *Nat Rev Mol Cell Biol*. 2003;4:192-201. doi: 10.1038/nrm1049
9. Voutsadakis IA. The ubiquitin-proteasome system and signal transduction pathways regulating Epithelial Mesenchymal transition of cancer. *J Biomed Sci*. 2012;19:67. doi: 10.1186/1423-0127-19-67
10. Portbury AL, Ronnebaum SM, Zungu M, Patterson C, Willis MS. Back to your heart: ubiquitin proteasome system-regulated signal transduction. *J Mol Cell Cardiol*. 2012;52:526-537. doi: 10.1016/j.yjmcc.2011.10.023
11. Dang F, Nie L, Wei W. Ubiquitin signaling in cell cycle control and tumorigenesis. *Cell Death Differ*. 2021;28:427-438. doi: 10.1038/s41418-020-00648-0
12. Abbas R, Larisch S. Killing by Degradation: Regulation of Apoptosis by the Ubiquitin-Proteasome-System. *Cells*. 2021;10. doi: 10.3390/cells10123465
13. Buchberger A, Bukau B, Sommer T. Protein quality control in the cytosol and the endoplasmic reticulum: brothers in arms. *Mol Cell*. 2010;40:238-252. doi: 10.1016/j.molcel.2010.10.001
14. Franić D, Zubčić K, Boban M. Nuclear Ubiquitin-Proteasome Pathways in Proteostasis Maintenance. *Biomolecules*. 2021;11. doi: 10.3390/biom11010054
15. Ciechanover A, Schwartz AL. The ubiquitin-proteasome pathway: the complexity and myriad functions of proteins death. *Proc Natl Acad Sci U S A*. 1998;95:2727-2730. doi: 10.1073/pnas.95.6.2727
16. Glickman MH, Ciechanover A. The ubiquitin-proteasome proteolytic pathway: destruction for the sake of construction. *Physiol Rev*. 2002;82:373-428. doi: 10.1152/physrev.00027.2001
17. Ciechanover A. The ubiquitin proteolytic system: from a vague idea, through basic mechanisms, and onto human diseases and drug targeting. *Neurology*. 2006;66:S7-19. doi: 10.1212/01.wnl.0000192261.02023.b8

18. Schulman BA, Harper JW. Ubiquitin-like protein activation by E1 enzymes: the apex for downstream signalling pathways. *Nat Rev Mol Cell Biol*. 2009;10:319-331. doi: 10.1038/nrm2673
19. Ye Y, Rape M. Building ubiquitin chains: E2 enzymes at work. *Nat Rev Mol Cell Biol*. 2009;10:755-764. doi: 10.1038/nrm2780
20. Yang Q, Zhao J, Chen D, Wang Y. E3 ubiquitin ligases: styles, structures and functions. *Mol Biomed*. 2021;2:23. doi: 10.1186/s43556-021-00043-2
21. Zheng N, Shabek N. Ubiquitin Ligases: Structure, Function, and Regulation. *Annu Rev Biochem*. 2017;86:129-157. doi: 10.1146/annurev-biochem-060815-014922
22. Li W, Tu D, Brunger AT, Ye Y. A ubiquitin ligase transfers preformed polyubiquitin chains from a conjugating enzyme to a substrate. *Nature*. 2007;446:333-337. doi: 10.1038/nature05542
23. Tu D, Li W, Ye Y, Brunger AT. Structure and function of the yeast U-box-containing ubiquitin ligase Ufd2p. *Proc Natl Acad Sci U S A*. 2007;104:15599-15606. doi: 10.1073/pnas.0701369104
24. McClellan AJ, Laugesen SH, Ellgaard L. Cellular functions and molecular mechanisms of non-lysine ubiquitination. *Open Biol*. 2019;9:190147. doi: 10.1098/rsob.190147
25. Zinngrebe J, Montinaro A, Peltzer N, Walczak H. Ubiquitin in the immune system. *EMBO Rep*. 2014;15:28-45. doi: 10.1002/embr.201338025
26. Pickart CM, Fushman D. Polyubiquitin chains: polymeric protein signals. *Curr Opin Chem Biol*. 2004;8:610-616. doi: 10.1016/j.cbpa.2004.09.009
27. Varadan R, Walker O, Pickart C, Fushman D. Structural properties of polyubiquitin chains in solution. *J Mol Biol*. 2002;324:637-647. doi: 10.1016/s0022-2836(02)01198-1
28. Eddins MJ, Varadan R, Fushman D, Pickart CM, Wolberger C. Crystal structure and solution NMR studies of Lys48-linked tetraubiquitin at neutral pH. *J Mol Biol*. 2007;367:204-211. doi: 10.1016/j.jmb.2006.12.065
29. Ulrich HD. Degradation or maintenance: actions of the ubiquitin system on eukaryotic chromatin. *Eukaryot Cell*. 2002;1:1-10. doi: 10.1128/ec.1.1.1-10.2002
30. Hicke L, Dunn R. Regulation of membrane protein transport by ubiquitin and ubiquitin-binding proteins. *Annu Rev Cell Dev Biol*. 2003;19:141-172. doi: 10.1146/annurev.cellbio.19.110701.154617
31. Madiraju C, Novack JP, Reed JC, Matsuzawa SI. K63 ubiquitination in immune signaling. *Trends Immunol*. 2022;43:148-162. doi: 10.1016/j.it.2021.12.005
32. Spence J, Gali RR, Dittmar G, Sherman F, Karin M, Finley D. Cell cycle-regulated modification of the ribosome by a variant multiubiquitin chain. *Cell*. 2000;102:67-76. doi: 10.1016/s0092-8674(00)00011-8
33. Dikic I. Proteasomal and Autophagic Degradation Systems. *Annu Rev Biochem*. 2017;86:193-224. doi: 10.1146/annurev-biochem-061516-044908
34. Ohtake F, Tsuchiya H, Saeki Y, Tanaka K. K63 ubiquitylation triggers proteasomal degradation by seeding branched ubiquitin chains. *Proc Natl Acad Sci U S A*. 2018;115:E1401-e1408. doi: 10.1073/pnas.1716673115
35. Dittmar G, Winklhofer KF. Linear Ubiquitin Chains: Cellular Functions and Strategies for Detection and Quantification. *Front Chem*. 2019;7:915. doi: 10.3389/fchem.2019.00915
36. van Well EM, Bader V, Patra M, Sánchez-Vicente A, Meschede J, Furthmann N, Schnack C, Blusch A, Longworth J, Petrasch-Parwez E, Mori K, Arzberger T, Trümbach

D, Angersbach L, Showkat C, Sehr DA, Berlemann LA, Goldmann P, Clement AM, Behl C, Woerner AC, Saft C, Wurst W, Haass C, Ellrichmann G, Gold R, Dittmar G, Hipp MS, Hartl FU, Tatzelt J, Winklhofer KF. A protein quality control pathway regulated by linear ubiquitination. *Embo j*. 2019;38. doi: 10.15252/embj.2018100730
37. Nguyen HC, Wang W, Xiong Y. Cullin-RING E3 Ubiquitin Ligases: Bridges to Destruction. *Subcell Biochem*. 2017;83:323-347. doi: 10.1007/978-3-319-46503-6_12
38. Hatakeyama S, Yada M, Matsumoto M, Ishida N, Nakayama KI. U box proteins as a new family of ubiquitin-protein ligases. *J Biol Chem*. 2001;276:33111-33120. doi: 10.1074/jbc.M102755200
39. Sluimer J, Distel B. Regulating the human HECT E3 ligases. *Cell Mol Life Sci*. 2018;75:3121-3141. doi: 10.1007/s00018-018-2848-2
40. Smit JJ, Sixma TK. RBR E3-ligases at work. *EMBO Rep*. 2014;15:142-154. doi: 10.1002/embr.201338166
41. Goto J, Otaki Y, Watanabe T, Watanabe M. The Role of HECT-Type E3 Ligase in the Development of Cardiac Disease. *Int J Mol Sci*. 2021;22. doi: 10.3390/ijms22116065
42. Borlepawar A, Frey N, Rangrez AY. A systematic view on E3 ligase Ring TRIMmers with a focus on cardiac function and disease. *Trends Cardiovasc Med*. 2019;29:1-8. doi: 10.1016/j.tcm.2018.05.007
43. Bai T, Wang F, Mellen N, Zheng Y, Cai L. Diabetic cardiomyopathy: role of the E3 ubiquitin ligase. *Am J Physiol Endocrinol Metab*. 2016;310:E473-483. doi: 10.1152/ajpendo.00467.2015
44. Goto J, Otaki Y, Watanabe T, Kobayashi Y, Aono T, Watanabe K, Wanezaki M, Kutsuzawa D, Kato S, Tamura H, Nishiyama S, Arimoto T, Takahashi H, Shishido T, Watanabe M. HECT (Homologous to the E6-AP Carboxyl Terminus)-Type Ubiquitin E3 Ligase ITCH Attenuates Cardiac Hypertrophy by Suppressing the Wnt/β-Catenin Signaling Pathway. *Hypertension*. 2020;76:1868-1878. doi: 10.1161/hypertensionaha.120.15487
45. Otaki Y, Takahashi H, Watanabe T, Funayama A, Netsu S, Honda Y, Narumi T, Kadowaki S, Hasegawa H, Honda S, Arimoto T, Shishido T, Miyamoto T, Kamata H, Nakajima O, Kubota I. HECT-Type Ubiquitin E3 Ligase ITCH Interacts With Thioredoxin-Interacting Protein and Ameliorates Reactive Oxygen Species-Induced Cardiotoxicity. *J Am Heart Assoc*. 2016;5. doi: 10.1161/jaha.115.002485
46. Zhang N, Zhang Y, Qian H, Wu S, Cao L, Sun Y. Selective targeting of ubiquitination and degradation of PARP1 by E3 ubiquitin ligase WWP2 regulates isoproterenol-induced cardiac remodeling. *Cell Death Differ*. 2020;27:2605-2619. doi: 10.1038/s41418-020-0523-2
47. Wang S, Sun A, Li L, Zhao G, Jia J, Wang K, Ge J, Zou Y. Up-regulation of BMP-2 antagonizes TGF-β1/ROCK-enhanced cardiac fibrotic signalling through activation of Smurf1/Smad6 complex. *J Cell Mol Med*. 2012;16:2301-2310. doi: 10.1111/j.1582-4934.2012.01538.x
48. Cunnington RH, Nazari M, Dixon IM. c-Ski, Smurf2, and Arkadia as regulators of TGF-beta signaling: new targets for managing myofibroblast function and cardiac fibrosis. *Can J Physiol Pharmacol*. 2009;87:764-772. doi: 10.1139/y09-076
49. Clague MJ, Urbé S, Komander D. Breaking the chains: deubiquitylating enzyme specificity begets function. *Nat Rev Mol Cell Biol*. 2019;20:338-352. doi: 10.1038/s41580-019-0099-1

50. Reyes-Turcu FE, Ventii KH, Wilkinson KD. Regulation and cellular roles of ubiquitin-specific deubiquitinating enzymes. *Annu Rev Biochem*. 2009;78:363-397. doi: 10.1146/annurev.biochem.78.082307.091526
51. de Poot SAH, Tian G, Finley D. Meddling with Fate: The Proteasomal Deubiquitinating Enzymes. *J Mol Biol*. 2017;429:3525-3545. doi: 10.1016/j.jmb.2017.09.015
52. Voges D, Zwickl P, Baumeister W. The 26S proteasome: a molecular machine designed for controlled proteolysis. *Annu Rev Biochem*. 1999;68:1015-1068. doi: 10.1146/annurev.biochem.68.1.1015
53. Cascio P, Call M, Petre BM, Walz T, Goldberg AL. Properties of the hybrid form of the 26S proteasome containing both 19S and PA28 complexes. *Embo j*. 2002;21:2636-2645. doi: 10.1093/emboj/21.11.2636
54. Zhang Z, Krutchinsky A, Endicott S, Realini C, Rechsteiner M, Standing KG. Proteasome activator 11S REG or PA28: recombinant REG alpha/REG beta hetero-oligomers are heptamers. *Biochemistry*. 1999;38:5651-5658. doi: 10.1021/bi990056+
55. Realini C, Jensen CC, Zhang Z, Johnston SC, Knowlton JR, Hill CP, Rechsteiner M. Characterization of recombinant REGalpha, REGbeta, and REGgamma proteasome activators. *J Biol Chem*. 1997;272:25483-25492. doi: 10.1074/jbc.272.41.25483
56. Saeki Y. Ubiquitin recognition by the proteasome. *J Biochem*. 2017;161:113-124. doi: 10.1093/jb/mvw091
57. Tanaka K. The proteasome: overview of structure and functions. *Proc Jpn Acad Ser B Phys Biol Sci*. 2009;85:12-36. doi: 10.2183/pjab.85.12
58. Kaur G, Batra S. Emerging role of immunoproteasomes in pathophysiology. *Immunol Cell Biol*. 2016;94:812-820. doi: 10.1038/icb.2016.50
59. Murata S, Takahama Y, Kasahara M, Tanaka K. The immunoproteasome and thymoproteasome: functions, evolution and human disease. *Nat Immunol*. 2018;19:923-931. doi: 10.1038/s41590-018-0186-z
60. Hisamatsu H, Shimbara N, Saito Y, Kristensen P, Hendil KB, Fujiwara T, Takahashi E, Tanahashi N, Tamura T, Ichihara A, Tanaka K. Newly identified pair of proteasomal subunits regulated reciprocally by interferon gamma. *J Exp Med*. 1996;183:1807-1816. doi: 10.1084/jem.183.4.1807
61. Gomes AV, Zong C, Edmondson RD, Li X, Stefani E, Zhang J, Jones RC, Thyparambil S, Wang GW, Qiao X, Bardag-Gorce F, Ping P. Mapping the murine cardiac 26S proteasome complexes. *Circ Res*. 2006;99:362-371. doi: 10.1161/01.RES.0000237386.98506.f7
62. Bai M, Zhao X, Sahara K, Ohte Y, Hirano Y, Kaneko T, Yashiroda H, Murata S. In-depth Analysis of the Lid Subunits Assembly Mechanism in Mammals. *Biomolecules*. 2019;9. doi: 10.3390/biom9060213
63. Smith DM, Chang SC, Park S, Finley D, Cheng Y, Goldberg AL. Docking of the proteasomal ATPases' carboxyl termini in the 20S proteasome's alpha ring opens the gate for substrate entry. *Mol Cell*. 2007;27:731-744. doi: 10.1016/j.molcel.2007.06.033
64. Mayor T, Sharon M, Glickman MH. Tuning the proteasome to brighten the end of the journey. *Am J Physiol Cell Physiol*. 2016;311:C793-c804. doi: 10.1152/ajpcell.00198.2016
65. Lander GC, Estrin E, Matyskiela ME, Bashore C, Nogales E, Martin A. Complete subunit architecture of the proteasome regulatory particle. *Nature*. 2012;482:186-191. doi: 10.1038/nature10774

66. Lasker K, Förster F, Bohn S, Walzthoeni T, Villa E, Unverdorben P, Beck F, Aebersold R, Sali A, Baumeister W. Molecular architecture of the 26S proteasome holocomplex determined by an integrative approach. *Proc Natl Acad Sci U S A*. 2012;109:1380-1387. doi: 10.1073/pnas.1120559109
67. Pathare GR, Nagy I, Bohn S, Unverdorben P, Hubert A, Körner R, Nickell S, Lasker K, Sali A, Tamura T, Nishioka T, Förster F, Baumeister W, Bracher A. The proteasomal subunit Rpn6 is a molecular clamp holding the core and regulatory subcomplexes together. *Proc Natl Acad Sci U S A*. 2012;109:149-154. doi: 10.1073/pnas.1117648108
68. Hartl FU, Bracher A, Hayer-Hartl M. Molecular chaperones in protein folding and proteostasis. *Nature*. 2011;475:324-332. doi: 10.1038/nature10317
69. Powers ET, Balch WE. Diversity in the origins of proteostasis networks--a driver for protein function in evolution. *Nat Rev Mol Cell Biol*. 2013;14:237-248. doi: 10.1038/nrm3542
70. Sandri M, Robbins J. Proteotoxicity: an underappreciated pathology in cardiac disease. *J Mol Cell Cardiol*. 2014;71:3-10. doi: 10.1016/j.yjmcc.2013.12.015
71. Galluzzi L, Bravo-San Pedro JM, Vitale I, Aaronson SA, Abrams JM, Adam D, Alnemri ES, Altucci L, Andrews D, Annicchiarico-Petruzzelli M, Baehrecke EH, Bazan NG, Bertrand MJ, Bianchi K, Blagosklonny MV, Blomgren K, Borner C, Bredesen DE, Brenner C, Campanella M, Candi E, Cecconi F, Chan FK, Chandel NS, Cheng EH, Chipuk JE, Cidlowski JA, Ciechanover A, Dawson TM, Dawson VL, De Laurenzi V, De Maria R, Debatin KM, Di Daniele N, Dixit VM, Dynlacht BD, El-Deiry WS, Fimia GM, Flavell RA, Fulda S, Garrido C, Gougeon ML, Green DR, Gronemeyer H, Hajnoczky G, Hardwick JM, Hengartner MO, Ichijo H, Joseph B, Jost PJ, Kaufmann T, Kepp O, Klionsky DJ, Knight RA, Kumar S, Lemasters JJ, Levine B, Linkermann A, Lipton SA, Lockshin RA, López-Otín C, Lugli E, Madeo F, Malorni W, Marine JC, Martin SJ, Martinou JC, Medema JP, Meier P, Melino S, Mizushima N, Moll U, Muñoz-Pinedo C, Nuñez G, Oberst A, Panaretakis T, Penninger JM, Peter ME, Piacentini M, Pinton P, Prehn JH, Puthalakath H, Rabinovich GA, Ravichandran KS, Rizzuto R, Rodrigues CM, Rubinsztein DC, Rudel T, Shi Y, Simon HU, Stockwell BR, Szabadkai G, Tait SW, Tang HL, Tavernarakis N, Tsujimoto Y, Vanden Berghe T, Vandenabeele P, Villunger A, Wagner EF, Walczak H, White E, Wood WG, Yuan J, Zakeri Z, Zhivotovsky B, Melino G, Kroemer G. Essential versus accessory aspects of cell death: recommendations of the NCCD 2015. *Cell Death Differ*. 2015;22:58-73. doi: 10.1038/cdd.2014.137
72. Henning RH, Brundel B. Proteostasis in cardiac health and disease. *Nat Rev Cardiol*. 2017;14:637-653. doi: 10.1038/nrcardio.2017.89
73. Golenhofen N, Perng MD, Quinlan RA, Drenckhahn D. Comparison of the small heat shock proteins alphaB-crystallin, MKBP, HSP25, HSP20, and cvHSP in heart and skeletal muscle. *Histochem Cell Biol*. 2004;122:415-425. doi: 10.1007/s00418-004-0711-z
74. Zhang H, Gomez AM, Wang X, Yan Y, Zheng M, Cheng H. ROS regulation of microdomain Ca(2+) signalling at the dyads. *Cardiovasc Res*. 2013;98:248-258. doi: 10.1093/cvr/cvt050
75. Nah J, Fernández Á F, Kitsis RN, Levine B, Sadoshima J. Does Autophagy Mediate Cardiac Myocyte Death During Stress? *Circ Res*. 2016;119:893-895. doi: 10.1161/circresaha.116.309765

76. Wang X, Wang H. Priming the Proteasome to Protect against Proteotoxicity. *Trends Mol Med*. 2020;26:639-648. doi: 10.1016/j.molmed.2020.02.007
77. Chen Q, Liu JB, Horak KM, Zheng H, Kumarapeli AR, Li J, Li F, Gerdes AM, Wawrousek EF, Wang X. Intrasarcoplasmic amyloidosis impairs proteolytic function of proteasomes in cardiomyocytes by compromising substrate uptake. *Circ Res*. 2005;97:1018-1026. doi: 10.1161/01.RES.0000189262.92896.0b
78. Loescher CM, Hobbach AJ, Linke WA. Titin (TTN): from molecule to modifications, mechanics, and medical significance. *Cardiovasc Res*. 2022;118:2903-2918. doi: 10.1093/cvr/cvab328
79. Roberts AM, Ware JS, Herman DS, Schafer S, Baksi J, Bick AG, Buchan RJ, Walsh R, John S, Wilkinson S, Mazzarotto F, Felkin LE, Gong S, MacArthur JA, Cunningham F, Flannick J, Gabriel SB, Altshuler DM, Macdonald PS, Heinig M, Keogh AM, Hayward CS, Banner NR, Pennell DJ, O'Regan DP, San TR, de Marvao A, Dawes TJ, Gulati A, Birks EJ, Yacoub MH, Radke M, Gotthardt M, Wilson JG, O'Donnell CJ, Prasad SK, Barton PJ, Fatkin D, Hubner N, Seidman JG, Seidman CE, Cook SA. Integrated allelic, transcriptional, and phenomic dissection of the cardiac effects of titin truncations in health and disease. *Sci Transl Med*. 2015;7:270ra276. doi: 10.1126/scitranslmed.3010134
80. Fomin A, Gärtner A, Cyganek L, Tiburcy M, Tuleta I, Wellers L, Folsche L, Hobbach AJ, von Frieling-Salewsky M, Unger A, Hucke A, Koser F, Kassner A, Sielemann K, Streckfuß-Bömeke K, Hasenfuss G, Goedel A, Laugwitz KL, Moretti A, Gummert JF, Dos Remedios CG, Reinecke H, Knöll R, van Heesch S, Hubner N, Zimmermann WH, Milting H, Linke WA. Truncated titin proteins and titin haploinsufficiency are targets for functional recovery in human cardiomyopathy due to TTN mutations. *Sci Transl Med*. 2021;13:eabd3079. doi: 10.1126/scitranslmed.abd3079
81. Fang X, Bogomolovas J, Wu T, Zhang W, Liu C, Veevers J, Stroud MJ, Zhang Z, Ma X, Mu Y, Lao DH, Dalton ND, Gu Y, Wang C, Wang M, Liang Y, Lange S, Ouyang K, Peterson KL, Evans SM, Chen J. Loss-of-function mutations in co-chaperone BAG3 destabilize small HSPs and cause cardiomyopathy. *J Clin Invest*. 2017;127:3189-3200. doi: 10.1172/jci94310
82. Stürner E, Behl C. The Role of the Multifunctional BAG3 Protein in Cellular Protein Quality Control and in Disease. *Front Mol Neurosci*. 2017;10:177. doi: 10.3389/fnmol.2017.00177
83. Martin TG, Kirk JA. Under construction: The dynamic assembly, maintenance, and degradation of the cardiac sarcomere. *J Mol Cell Cardiol*. 2020;148:89-102. doi: 10.1016/j.yjmcc.2020.08.018
84. Wang X, Robbins J. Proteasomal and lysosomal protein degradation and heart disease. *J Mol Cell Cardiol*. 2014;71:16-24. doi: 10.1016/j.yjmcc.2013.11.006
85. Thibaudeau TA, Anderson RT, Smith DM. A common mechanism of proteasome impairment by neurodegenerative disease-associated oligomers. *Nat Commun*. 2018;9:1097. doi: 10.1038/s41467-018-03509-0
86. Zhang H, Wang X. Priming the proteasome by protein kinase G: a novel cardioprotective mechanism of sildenafil. *Future Cardiol*. 2015;11:177-189. doi: 10.2217/fca.15.3
87. Predmore JM, Wang P, Davis F, Bartolone S, Westfall MV, Dyke DB, Pagani F, Powell SR, Day SM. Ubiquitin proteasome dysfunction in human hypertrophic and dilated cardiomyopathies. *Circulation*. 2010;121:997-1004. doi: 10.1161/circulationaha.109.904557

88. Kassiotis C, Ballal K, Wellnitz K, Vela D, Gong M, Salazar R, Frazier OH, Taegtmeyer H. Markers of autophagy are downregulated in failing human heart after mechanical unloading. *Circulation*. 2009;120:S191-197. doi: 10.1161/circulationaha.108.842252
89. Wohlschlaeger J, Sixt SU, Stoeppler T, Schmitz KJ, Levkau B, Tsagakis K, Vahlhaus C, Schmid C, Peters J, Schmid KW, Milting H, Baba HA. Ventricular unloading is associated with increased 20s proteasome protein expression in the myocardium. *J Heart Lung Transplant*. 2010;29:125-132. doi: 10.1016/j.healun.2009.07.022
90. Day SM, Divald A, Wang P, Davis F, Bartolone S, Jones R, Powell SR. Impaired assembly and post-translational regulation of 26S proteasome in human end-stage heart failure. *Circ Heart Fail*. 2013;6:544-549. doi: 10.1161/circheartfailure.112.000119
91. Willis MS, Patterson C. Proteotoxicity and cardiac dysfunction. *N Engl J Med*. 2013;368:1755. doi: 10.1056/NEJMc1302511
92. Nelson R, Eisenberg D. Structural models of amyloid-like fibrils. *Adv Protein Chem*. 2006;73:235-282. doi: 10.1016/s0065-3233(06)73008-x
93. Agnetti G, Halperin VL, Kirk JA, Chakir K, Guo Y, Lund L, Nicolini F, Gherli T, Guarnieri C, Caldarera CM, Tomaselli GF, Kass DA, Van Eyk JE. Desmin modifications associate with amyloid-like oligomers deposition in heart failure. *Cardiovasc Res*. 2014;102:24-34. doi: 10.1093/cvr/cvu003
94. Sanbe A, Osinska H, Saffitz JE, Glabe CG, Kayed R, Maloyan A, Robbins J. Desmin-related cardiomyopathy in transgenic mice: a cardiac amyloidosis. *Proc Natl Acad Sci U S A*. 2004;101:10132-10136. doi: 10.1073/pnas.0401900101
95. Sidorova TN, Mace LC, Wells KS, Yermalitskaya LV, Su PF, Shyr Y, Byrne JG, Petracek MR, Greelish JP, Hoff SJ, Ball SK, Glabe CG, Brown NJ, Barnett JV, Murray KT. Quantitative Imaging of Preamyloid Oligomers, a Novel Structural Abnormality, in Human Atrial Samples. *J Histochem Cytochem*. 2014;62:479-487. doi: 10.1369/0022155414535782
96. Röcken C, Peters B, Juenemann G, Saeger W, Klein HU, Huth C, Roessner A, Goette A. Atrial amyloidosis: an arrhythmogenic substrate for persistent atrial fibrillation. *Circulation*. 2002;106:2091-2097. doi: 10.1161/01.cir.0000034511.06350.df
97. Podduturi V, Armstrong DR, Hitchcock MA, Roberts WC, Guileyardo JM. Isolated atrial amyloidosis and the importance of molecular classification. *Proc (Bayl Univ Med Cent)*. 2013;26:387-389. doi: 10.1080/08998280.2013.11929013
98. Pellman J, Sheikh F. A new mechanism links preamyloid oligomer formation in the myocyte stress response associated with atrial fibrillation. *J Mol Cell Cardiol*. 2015;80:110-113. doi: 10.1016/j.yjmcc.2014.12.005
99. Weekes J, Morrison K, Mullen A, Wait R, Barton P, Dunn MJ. Hyperubiquitination of proteins in dilated cardiomyopathy. *Proteomics*. 2003;3:208-216. doi: 10.1002/pmic.200390029
100. Kostin S, Pool L, Elsässer A, Hein S, Drexler HC, Arnon E, Hayakawa Y, Zimmermann R, Bauer E, Klövekorn WP, Schaper J. Myocytes die by multiple mechanisms in failing human hearts. *Circ Res*. 2003;92:715-724. doi: 10.1161/01.Res.0000067471.95890.5c
101. Birks EJ, Latif N, Enesa K, Folkvang T, Luong le A, Sarathchandra P, Khan M, Ovaa H, Terracciano CM, Barton PJ, Yacoub MH, Evans PC. Elevated p53 expression is associated with dysregulation of the ubiquitin-proteasome system in dilated cardiomyopathy. *Cardiovasc Res*. 2008;79:472-480. doi: 10.1093/cvr/cvn083

102. Hein S, Arnon E, Kostin S, Schönburg M, Elsässer A, Polyakova V, Bauer EP, Klövekorn WP, Schaper J. Progression from compensated hypertrophy to failure in the pressure-overloaded human heart: structural deterioration and compensatory mechanisms. *Circulation*. 2003;107:984-991. doi: 10.1161/01.cir.0000051865.66123.b7
103. Georgiopoulos G, Makris N, Laina A, Theodorakakou F, Briasoulis A, Trougakos IP, Dimopoulos MA, Kastritis E, Stamatelopoulos K. Cardiovascular Toxicity of Proteasome Inhibitors: Underlying Mechanisms and Management Strategies: JACC: CardioOncology State-of-the-Art Review. *JACC CardioOncol*. 2023;5:1-21. doi: 10.1016/j.jaccao.2022.12.005
104. Goldfarb LG, Dalakas MC. Tragedy in a heartbeat: malfunctioning desmin causes skeletal and cardiac muscle disease. *J Clin Invest*. 2009;119:1806-1813. doi: 10.1172/jci38027
105. McLendon PM, Robbins J. Desmin-related cardiomyopathy: an unfolding story. *Am J Physiol Heart Circ Physiol*. 2011;301:H1220-1228. doi: 10.1152/ajpheart.00601.2011
106. Wang X, Osinska H, Dorn GW, 2nd, Nieman M, Lorenz JN, Gerdes AM, Witt S, Kimball T, Gulick J, Robbins J. Mouse model of desmin-related cardiomyopathy. *Circulation*. 2001;103:2402-2407. doi: 10.1161/01.cir.103.19.2402
107. Wang X, Osinska H, Klevitsky R, Gerdes AM, Nieman M, Lorenz J, Hewett T, Robbins J. Expression of R120G-alphaB-crystallin causes aberrant desmin and alphaB-crystallin aggregation and cardiomyopathy in mice. *Circ Res*. 2001;89:84-91. doi: 10.1161/hh1301.092688
108. Li J, Horak KM, Su H, Sanbe A, Robbins J, Wang X. Enhancement of proteasomal function protects against cardiac proteinopathy and ischemia/reperfusion injury in mice. *J Clin Invest*. 2011;121:3689-3700. doi: 10.1172/jci45709
109. Tian Z, Zheng H, Li J, Li Y, Su H, Wang X. Genetically induced moderate inhibition of the proteasome in cardiomyocytes exacerbates myocardial ischemia-reperfusion injury in mice. *Circ Res*. 2012;111:532-542. doi: 10.1161/circresaha.112.270983
110. Cattin ME, Bertrand AT, Schlossarek S, Le Bihan MC, Skov Jensen S, Neuber C, Crocini C, Maron S, Lainé J, Mougenot N, Varnous S, Fromes Y, Hansen A, Eschenhagen T, Decostre V, Carrier L, Bonne G. Heterozygous LmnadelK32 mice develop dilated cardiomyopathy through a combined pathomechanism of haploinsufficiency and peptide toxicity. *Hum Mol Genet*. 2013;22:3152-3164. doi: 10.1093/hmg/ddt172
111. Li J, Ma W, Yue G, Tang Y, Kim IM, Weintraub NL, Wang X, Su H. Cardiac proteasome functional insufficiency plays a pathogenic role in diabetic cardiomyopathy. *J Mol Cell Cardiol*. 2017;102:53-60. doi: 10.1016/j.yjmcc.2016.11.013
112. Schlossarek S, Englmann DR, Sultan KR, Sauer M, Eschenhagen T, Carrier L. Defective proteolytic systems in Mybpc3-targeted mice with cardiac hypertrophy. *Basic Res Cardiol*. 2012;107:235. doi: 10.1007/s00395-011-0235-3
113. Herrmann J, Wohlert C, Saguner AM, Flores A, Nesbitt LL, Chade A, Lerman LO, Lerman A. Primary proteasome inhibition results in cardiac dysfunction. *Eur J Heart Fail*. 2013;15:614-623. doi: 10.1093/eurjhf/hft034
114. Collins GA, Goldberg AL. The Logic of the 26S Proteasome. *Cell*. 2017;169:792-806. doi: 10.1016/j.cell.2017.04.023
115. Bard JAM, Bashore C, Dong KC, Martin A. The 26S Proteasome Utilizes a Kinetic Gateway to Prioritize Substrate Degradation. *Cell*. 2019;177:286-298.e215. doi: 10.1016/j.cell.2019.02.031

116. Guo X, Huang X, Chen MJ. Reversible phosphorylation of the 26S proteasome. *Protein Cell*. 2017;8:255-272. doi: 10.1007/s13238-017-0382-x
117. Goldberg AL, Kim HT, Lee D, Collins GA. Mechanisms That Activate 26S Proteasomes and Enhance Protein Degradation. *Biomolecules*. 2021;11. doi: 10.3390/biom11060779
118. VerPlank JJS, Goldberg AL. Regulating protein breakdown through proteasome phosphorylation. *Biochem J*. 2017;474:3355-3371. doi: 10.1042/bcj20160809
119. Pereira ME, Wilk S. Phosphorylation of the multicatalytic proteinase complex from bovine pituitaries by a copurifying cAMP-dependent protein kinase. *Arch Biochem Biophys*. 1990;283:68-74. doi: 10.1016/0003-9861(90)90613-4
120. Marambaud P, Wilk S, Checler F. Protein kinase A phosphorylation of the proteasome: a contribution to the alpha-secretase pathway in human cells. *J Neurochem*. 1996;67:2616-2619. doi: 10.1046/j.1471-4159.1996.67062616.x
121. Zong C, Gomes AV, Drews O, Li X, Young GW, Berhane B, Qiao X, French SW, Bardag-Gorce F, Ping P. Regulation of murine cardiac 20S proteasomes: role of associating partners. *Circ Res*. 2006;99:372-380. doi: 10.1161/01.Res.0000237389.40000.02
122. Lu H, Zong C, Wang Y, Young GW, Deng N, Souda P, Li X, Whitelegge J, Drews O, Yang PY, Ping P. Revealing the dynamics of the 20 S proteasome phosphoproteome: a combined CID and electron transfer dissociation approach. *Mol Cell Proteomics*. 2008;7:2073-2089. doi: 10.1074/mcp.M800064-MCP200
123. Lokireddy S, Kukushkin NV, Goldberg AL. cAMP-induced phosphorylation of 26S proteasomes on Rpn6/PSMD11 enhances their activity and the degradation of misfolded proteins. *Proc Natl Acad Sci U S A*. 2015;112:E7176-7185. doi: 10.1073/pnas.1522332112
124. Zhang F, Hu Y, Huang P, Toleman CA, Paterson AJ, Kudlow JE. Proteasome function is regulated by cyclic AMP-dependent protein kinase through phosphorylation of Rpt6. *J Biol Chem*. 2007;282:22460-22471. doi: 10.1074/jbc.M702439200
125. VerPlank JJS, Lokireddy S, Zhao J, Goldberg AL. 26S Proteasomes are rapidly activated by diverse hormones and physiological states that raise cAMP and cause Rpn6 phosphorylation. *Proc Natl Acad Sci U S A*. 2019;116:4228-4237. doi: 10.1073/pnas.1809254116
126. Myeku N, Clelland CL, Emrani S, Kukushkin NV, Yu WH, Goldberg AL, Duff KE. Tau-driven 26S proteasome impairment and cognitive dysfunction can be prevented early in disease by activating cAMP-PKA signaling. *Nat Med*. 2016;22:46-53. doi: 10.1038/nm.4011
127. Asai M, Tsukamoto O, Minamino T, Asanuma H, Fujita M, Asano Y, Takahama H, Sasaki H, Higo S, Asakura M, Takashima S, Hori M, Kitakaze M. PKA rapidly enhances proteasome assembly and activity in in vivo canine hearts. *J Mol Cell Cardiol*. 2009;46:452-462. doi: 10.1016/j.yjmcc.2008.11.001
128. Zhang H, Pan B, Wu P, Parajuli N, Rekhter MD, Goldberg AL, Wang X. PDE1 inhibition facilitates proteasomal degradation of misfolded proteins and protects against cardiac proteinopathy. *Sci Adv*. 2019;5:eaaw5870. doi: 10.1126/sciadv.aaw5870
129. Krawutschke C, Koesling D, Russwurm M. Cyclic GMP in Vascular Relaxation: Export Is of Similar Importance as Degradation. *Arterioscler Thromb Vasc Biol*. 2015;35:2011-2019. doi: 10.1161/atvbaha.115.306133

130. Taoro-González L, Cabrera-Pastor A, Sancho-Alonso M, Felipo V. Intracellular and extracelluar cyclic GMP in the brain and the hippocampus. *Vitam Horm*. 2022;118:247-288. doi: 10.1016/bs.vh.2021.11.006
131. Patil CS, Singh VP, Jain NK, Kulkarni SK. Inhibitory effect of sildenafil on gastrointestinal smooth muscle: role of NO-cGMP transduction pathway. *Indian J Exp Biol*. 2005;43:167-171.
132. Ranek MJ, Terpstra EJ, Li J, Kass DA, Wang X. Protein kinase g positively regulates proteasome-mediated degradation of misfolded proteins. *Circulation*. 2013;128:365-376. doi: 10.1161/circulationaha.113.001971
133. Dhein S, van Koppen CJ, Brodde OE. Muscarinic receptors in the mammalian heart. *Pharmacol Res*. 2001;44:161-182. doi: 10.1006/phrs.2001.0835
134. Brodde OE, Bruck H, Leineweber K, Seyfarth T. Presence, distribution and physiological function of adrenergic and muscarinic receptor subtypes in the human heart. *Basic Res Cardiol*. 2001;96:528-538. doi: 10.1007/s003950170003
135. Ranek MJ, Kost CK, Jr., Hu C, Martin DS, Wang X. Muscarinic 2 receptors modulate cardiac proteasome function in a protein kinase G-dependent manner. *J Mol Cell Cardiol*. 2014;69:43-51. doi: 10.1016/j.yjmcc.2014.01.017
136. VerPlank JJS, Tyrkalska SD, Fleming A, Rubinsztein DC, Goldberg AL. cGMP via PKG activates 26S proteasomes and enhances degradation of proteins, including ones that cause neurodegenerative diseases. *Proc Natl Acad Sci U S A*. 2020;117:14220-14230. doi: 10.1073/pnas.2003277117
137. VerPlank JJS, Gawron J, Silvestri NJ, Feltri ML, Wrabetz L, Goldberg AL. Raising cGMP restores proteasome function and myelination in mice with a proteotoxic neuropathy. *Brain*. 2022;145:168-178. doi: 10.1093/brain/awab249
138. Hoeller D, Dikic I. Targeting the ubiquitin system in cancer therapy. *Nature*. 2009;458:438-444. doi: 10.1038/nature07960
139. Orlowski RZ, Kuhn DJ. Proteasome inhibitors in cancer therapy: lessons from the first decade. *Clin Cancer Res*. 2008;14:1649-1657. doi: 10.1158/1078-0432.Ccr-07-2218
140. Min M, Lindon C. Substrate targeting by the ubiquitin-proteasome system in mitosis. *Semin Cell Dev Biol*. 2012;23:482-491. doi: 10.1016/j.semcdb.2012.01.015
141. Dephoure N, Zhou C, Villén J, Beausoleil SA, Bakalarski CE, Elledge SJ, Gygi SP. A quantitative atlas of mitotic phosphorylation. *Proc Natl Acad Sci U S A*. 2008;105:10762-10767. doi: 10.1073/pnas.0805139105
142. Nagano K, Shinkawa T, Mutoh H, Kondoh O, Morimoto S, Inomata N, Ashihara M, Ishii N, Aoki Y, Haramura M. Phosphoproteomic analysis of distinct tumor cell lines in response to nocodazole treatment. *Proteomics*. 2009;9:2861-2874. doi: 10.1002/pmic.200800667
143. Olsen JV, Vermeulen M, Santamaria A, Kumar C, Miller ML, Jensen LJ, Gnad F, Cox J, Jensen TS, Nigg EA, Brunak S, Mann M. Quantitative phosphoproteomics reveals widespread full phosphorylation site occupancy during mitosis. *Sci Signal*. 2010;3:ra3. doi: 10.1126/scisignal.2000475
144. Kettenbach AN, Schweppe DK, Faherty BK, Pechenick D, Pletnev AA, Gerber SA. Quantitative phosphoproteomics identifies substrates and functional modules of Aurora and Polo-like kinase activities in mitotic cells. *Sci Signal*. 2011;4:rs5. doi: 10.1126/scisignal.2001497

145. Guo X, Wang X, Wang Z, Banerjee S, Yang J, Huang L, Dixon JE. Site-specific proteasome phosphorylation controls cell proliferation and tumorigenesis. *Nat Cell Biol*. 2016;18:202-212. doi: 10.1038/ncb3289
146. Guo X, Dixon JE. The 26S proteasome: A cell cycle regulator regulated by cell cycle. *Cell Cycle*. 2016;15:875-876. doi: 10.1080/15384101.2016.1151728
147. Marcotte R, Sayad A, Brown KR, Sanchez-Garcia F, Reimand J, Haider M, Virtanen C, Bradner JE, Bader GD, Mills GB, Pe'er D, Moffat J, Neel BG. Functional Genomic Landscape of Human Breast Cancer Drivers, Vulnerabilities, and Resistance. *Cell*. 2016;164:293-309. doi: 10.1016/j.cell.2015.11.062
148. Porrello ER, Mahmoud AI, Simpson E, Hill JA, Richardson JA, Olson EN, Sadek HA. Transient regenerative potential of the neonatal mouse heart. *Science*. 2011;331:1078-1080. doi: 10.1126/science.1200708
149. Bergmann O, Bhardwaj RD, Bernard S, Zdunek S, Barnabé-Heider F, Walsh S, Zupicich J, Alkass K, Buchholz BA, Druid H, Jovinge S, Frisén J. Evidence for cardiomyocyte renewal in humans. *Science*. 2009;324:98-102. doi: 10.1126/science.1164680
150. Malliaras K, Zhang Y, Seinfeld J, Galang G, Tseliou E, Cheng K, Sun B, Aminzadeh M, Marbán E. Cardiomyocyte proliferation and progenitor cell recruitment underlie therapeutic regeneration after myocardial infarction in the adult mouse heart. *EMBO Mol Med*. 2013;5:191-209. doi: 10.1002/emmm.201201737
151. Beltrami AP, Urbanek K, Kajstura J, Yan SM, Finato N, Bussani R, Nadal-Ginard B, Silvestri F, Leri A, Beltrami CA, Anversa P. Evidence that human cardiac myocytes divide after myocardial infarction. *N Engl J Med*. 2001;344:1750-1757. doi: 10.1056/nejm200106073442303
152. Li S, Ma W, Cai B. Targeting cardiomyocyte proliferation as a key approach of promoting heart repair after injury. *Mol Biomed*. 2021;2:34. doi: 10.1186/s43556-021-00047-y
153. Johnson J, Mohsin S, Houser SR. Cardiomyocyte Proliferation as a Source of New Myocyte Development in the Adult Heart. *Int J Mol Sci*. 2021;22. doi: 10.3390/ijms22157764
154. Poolman RA, Gilchrist R, Brooks G. Cell cycle profiles and expressions of p21CIP1 AND P27KIP1 during myocyte development. *Int J Cardiol*. 1998;67:133-142. doi: 10.1016/s0167-5273(98)00320-9
155. Erickson JR, He BJ, Grumbach IM, Anderson ME. CaMKII in the cardiovascular system: sensing redox states. *Physiol Rev*. 2011;91:889-915. doi: 10.1152/physrev.00018.2010
156. Feng N, Anderson ME. CaMKII is a nodal signal for multiple programmed cell death pathways in heart. *J Mol Cell Cardiol*. 2017;103:102-109. doi: 10.1016/j.yjmcc.2016.12.007
157. Dewenter M, von der Lieth A, Katus HA, Backs J. Calcium Signaling and Transcriptional Regulation in Cardiomyocytes. *Circ Res*. 2017;121:1000-1020. doi: 10.1161/circresaha.117.310355
158. Ling H, Zhang T, Pereira L, Means CK, Cheng H, Gu Y, Dalton ND, Peterson KL, Chen J, Bers D, Brown JH. Requirement for Ca2+/calmodulin-dependent kinase II in the transition from pressure overload-induced cardiac hypertrophy to heart failure in mice. *J Clin Invest*. 2009;119:1230-1240. doi: 10.1172/jci38022

159. Baier MJ, Klatt S, Hammer KP, Maier LS, Rokita AG. Ca(2+)/calmodulin-dependent protein kinase II is essential in hyperacute pressure overload. *J Mol Cell Cardiol*. 2020;138:212-221. doi: 10.1016/j.yjmcc.2019.12.002
160. Joiner ML, Koval OM, Li J, He BJ, Allamargot C, Gao Z, Luczak ED, Hall DD, Fink BD, Chen B, Yang J, Moore SA, Scholz TD, Strack S, Mohler PJ, Sivitz WI, Song LS, Anderson ME. CaMKII determines mitochondrial stress responses in heart. *Nature*. 2012;491:269-273. doi: 10.1038/nature11444
161. Mesubi OO, Anderson ME. Atrial remodelling in atrial fibrillation: CaMKII as a nodal proarrhythmic signal. *Cardiovasc Res*. 2016;109:542-557. doi: 10.1093/cvr/cvw002
162. Zhang R, Khoo MS, Wu Y, Yang Y, Grueter CE, Ni G, Price EE, Jr., Thiel W, Guatimosim S, Song LS, Madu EC, Shah AN, Vishnivetskaya TA, Atkinson JB, Gurevich VV, Salama G, Lederer WJ, Colbran RJ, Anderson ME. Calmodulin kinase II inhibition protects against structural heart disease. *Nat Med*. 2005;11:409-417. doi: 10.1038/nm1215
163. Zhang T, Maier LS, Dalton ND, Miyamoto S, Ross J, Jr., Bers DM, Brown JH. The deltaC isoform of CaMKII is activated in cardiac hypertrophy and induces dilated cardiomyopathy and heart failure. *Circ Res*. 2003;92:912-919. doi: 10.1161/01.Res.0000069686.31472.C5
164. Hegyi B, Bers DM, Bossuyt J. CaMKII signaling in heart diseases: Emerging role in diabetic cardiomyopathy. *J Mol Cell Cardiol*. 2019;127:246-259. doi: 10.1016/j.yjmcc.2019.01.001
165. Nassal D, Gratz D, Hund TJ. Challenges and Opportunities for Therapeutic Targeting of Calmodulin Kinase II in Heart. *Front Pharmacol*. 2020;11:35. doi: 10.3389/fphar.2020.00035
166. Cheng J, Xu L, Lai D, Guilbert A, Lim HJ, Keskanokwong T, Wang Y. CaMKII inhibition in heart failure, beneficial, harmful, or both. *Am J Physiol Heart Circ Physiol*. 2012;302:H1454-1465. doi: 10.1152/ajpheart.00812.2011
167. Djakovic SN, Schwarz LA, Barylko B, DeMartino GN, Patrick GN. Regulation of the proteasome by neuronal activity and calcium/calmodulin-dependent protein kinase II. *J Biol Chem*. 2009;284:26655-26665. doi: 10.1074/jbc.M109.021956
168. Djakovic SN, Marquez-Lona EM, Jakawich SK, Wright R, Chu C, Sutton MA, Patrick GN. Phosphorylation of Rpt6 regulates synaptic strength in hippocampal neurons. *J Neurosci*. 2012;32:5126-5131. doi: 10.1523/jneurosci.4427-11.2012
169. Bingol B, Wang CF, Arnott D, Cheng D, Peng J, Sheng M. Autophosphorylated CaMKIIalpha acts as a scaffold to recruit proteasomes to dendritic spines. *Cell*. 2010;140:567-578. doi: 10.1016/j.cell.2010.01.024
170. Hamilton AM, Oh WC, Vega-Ramirez H, Stein IS, Hell JW, Patrick GN, Zito K. Activity-dependent growth of new dendritic spines is regulated by the proteasome. *Neuron*. 2012;74:1023-1030. doi: 10.1016/j.neuron.2012.04.031
171. Jarome TJ, Kwapis JL, Ruenzel WL, Helmstetter FJ. CaMKII, but not protein kinase A, regulates Rpt6 phosphorylation and proteasome activity during the formation of long-term memories. *Front Behav Neurosci*. 2013;7:115. doi: 10.3389/fnbeh.2013.00115
172. Xu J, Kawahata I, Izumi H, Fukunaga K. T-Type Ca(2+) Enhancer SAK3 Activates CaMKII and Proteasome Activities in Lewy Body Dementia Mice Model. *Int J Mol Sci*. 2021;22. doi: 10.3390/ijms22126185

173. Zhang X, Hu C, Yuan XP, Yuan YP, Song P, Kong CY, Teng T, Hu M, Xu SC, Ma ZG, Tang QZ. Osteocrin, a novel myokine, prevents diabetic cardiomyopathy via restoring proteasomal activity. *Cell Death Dis*. 2021;12:624. doi: 10.1038/s41419-021-03922-2
174. Schaler AW, Myeku N. Cilostazol, a phosphodiesterase 3 inhibitor, activates proteasome-mediated proteolysis and attenuates tauopathy and cognitive decline. *Transl Res*. 2018;193:31-41. doi: 10.1016/j.trsl.2017.11.004
175. Owona BA, Zug C, Schluesener HJ, Zhang ZY. Protective Effects of Forskolin on Behavioral Deficits and Neuropathological Changes in a Mouse Model of Cerebral Amyloidosis. *J Neuropathol Exp Neurol*. 2016;75:618-627. doi: 10.1093/jnen/nlw043
176. Kumarapeli AR, Horak KM, Glasford JW, Li J, Chen Q, Liu J, Zheng H, Wang X. A novel transgenic mouse model reveals deregulation of the ubiquitin-proteasome system in the heart by doxorubicin. *Faseb j*. 2005;19:2051-2053. doi: 10.1096/fj.05-3973fje
177. Gilon T, Chomsky O, Kulka RG. Degradation signals for ubiquitin system proteolysis in Saccharomyces cerevisiae. *Embo j*. 1998;17:2759-2766. doi: 10.1093/emboj/17.10.2759
178. Gilon T, Chomsky O, Kulka RG. Degradation signals recognized by the Ubc6p-Ubc7p ubiquitin-conjugating enzyme pair. *Mol Cell Biol*. 2000;20:7214-7219. doi: 10.1128/mcb.20.19.7214-7219.2000
179. Vicart P, Caron A, Guicheney P, Li Z, Prévost MC, Faure A, Chateau D, Chapon F, Tomé F, Dupret JM, Paulin D, Fardeau M. A missense mutation in the alphaB-crystallin chaperone gene causes a desmin-related myopathy. *Nat Genet*. 1998;20:92-95. doi: 10.1038/1765
180. Ye S, Dhillon S, Ke X, Collins AR, Day IN. An efficient procedure for genotyping single nucleotide polymorphisms. *Nucleic Acids Res*. 2001;29:E88-88. doi: 10.1093/nar/29.17.e88
181. Medrano RF, de Oliveira CA. Guidelines for the tetra-primer ARMS-PCR technique development. *Mol Biotechnol*. 2014;56:599-608. doi: 10.1007/s12033-014-9734-4
182. Xu J. Preparation, culture, and immortalization of mouse embryonic fibroblasts. *Curr Protoc Mol Biol*. 2005;Chapter 28:Unit 28 21. doi: 10.1002/0471142727.mb2801s70
183. Ackers-Johnson M, Li PY, Holmes AP, O'Brien SM, Pavlovic D, Foo RS. A Simplified, Langendorff-Free Method for Concomitant Isolation of Viable Cardiac Myocytes and Nonmyocytes From the Adult Mouse Heart. *Circ Res*. 2016;119:909-920. doi: 10.1161/circresaha.116.309202
184. Guo L, Prall W, Yang X. Assays for the Degradation of Misfolded Proteins in Cells. *J Vis Exp*. 2016. doi: 10.3791/54266
185. Pan B, Li J, Parajuli N, Tian Z, Wu P, Lewno MT, Zou J, Wang W, Bedford L, Mayer RJ, Fang J, Liu J, Cui T, Su H, Wang X. The Calcineurin-TFEB-p62 Pathway Mediates the Activation of Cardiac Macroautophagy by Proteasomal Malfunction. *Circ Res*. 2020;127:502-518. doi: 10.1161/circresaha.119.316007
186. Wang X, Li J, Zheng H, Su H, Powell SR. Proteasome functional insufficiency in cardiac pathogenesis. *Am J Physiol Heart Circ Physiol*. 2011;301:H2207-2219. doi: 10.1152/ajpheart.00714.2011
187. Dong X, Liu J, Zheng H, Glasford JW, Huang W, Chen QH, Harden NR, Li F, Gerdes AM, Wang X. In situ dynamically monitoring the proteolytic function of the ubiquitin-proteasome system in cultured cardiac myocytes. *Am J Physiol Heart Circ Physiol*. 2004;287:H1417-1425. doi: 10.1152/ajpheart.01233.2003

188. Zheng Q, Su H, Ranek MJ, Wang X. Autophagy and p62 in cardiac proteinopathy. *Circ Res*. 2011;109:296-308. doi: 10.1161/circresaha.111.244707
189. Demasi M, Simões V, Bonatto D. Cross-talk between redox regulation and the ubiquitin-proteasome system in mammalian cell differentiation. *Biochim Biophys Acta*. 2015;1850:1594-1606. doi: 10.1016/j.bbagen.2014.10.031
190. Hernebring M, Brolén G, Aguilaniu H, Semb H, Nyström T. Elimination of damaged proteins during differentiation of embryonic stem cells. *Proc Natl Acad Sci U S A*. 2006;103:7700-7705. doi: 10.1073/pnas.0510944103
191. Goldfarb LG, Park KY, Cervenáková L, Gorokhova S, Lee HS, Vasconcelos O, Nagle JW, Semino-Mora C, Sivakumar K, Dalakas MC. Missense mutations in desmin associated with familial cardiac and skeletal myopathy. *Nat Genet*. 1998;19:402-403. doi: 10.1038/1300
192. Winter L, Türk M, Harter PN, Mittelbronn M, Kornblum C, Norwood F, Jungbluth H, Thiel CT, Schlötzer-Schrehardt U, Schröder R. Downstream effects of plectin mutations in epidermolysis bullosa simplex with muscular dystrophy. *Acta Neuropathol Commun*. 2016;4:44. doi: 10.1186/s40478-016-0314-7
193. Maloyan A, Osinska H, Lammerding J, Lee RT, Cingolani OH, Kass DA, Lorenz JN, Robbins J. Biochemical and mechanical dysfunction in a mouse model of desmin-related myopathy. *Circ Res*. 2009;104:1021-1028. doi: 10.1161/circresaha.108.193516
194. Tannous P, Zhu H, Johnstone JL, Shelton JM, Rajasekaran NS, Benjamin IJ, Nguyen L, Gerard RD, Levine B, Rothermel BA, Hill JA. Autophagy is an adaptive response in desmin-related cardiomyopathy. *Proc Natl Acad Sci U S A*. 2008;105:9745-9750. doi: 10.1073/pnas.0706802105
195. Alam S, Abdullah CS, Aishwarya R, Morshed M, Nitu SS, Miriyala S, Panchatcharam M, Kevil CG, Orr AW, Bhuiyan MS. Dysfunctional Mitochondrial Dynamic and Oxidative Phosphorylation Precedes Cardiac Dysfunction in R120G-αB-Crystallin-Induced Desmin-Related Cardiomyopathy. *J Am Heart Assoc*. 2020;9:e017195. doi: 10.1161/jaha.120.017195
196. Su H, Wang X. The ubiquitin-proteasome system in cardiac proteinopathy: a quality control perspective. *Cardiovasc Res*. 2010;85:253-262. doi: 10.1093/cvr/cvp287
197. Vilchez D, Morantte I, Liu Z, Douglas PM, Merkwirth C, Rodrigues AP, Manning G, Dillin A. RPN-6 determines C. elegans longevity under proteotoxic stress conditions. *Nature*. 2012;489:263-268. doi: 10.1038/nature11315
198. Chen S, Zhang Y, Lighthouse JK, Mickelsen DM, Wu J, Yao P, Small EM, Yan C. A Novel Role of Cyclic Nucleotide Phosphodiesterase 10A in Pathological Cardiac Remodeling and Dysfunction. *Circulation*. 2020;141:217-233. doi: 10.1161/circulationaha.119.042178
199. Zoccarato A, Surdo NC, Aronsen JM, Fields LA, Mancuso L, Dodoni G, Stangherlin A, Livie C, Jiang H, Sin YY, Gesellchen F, Terrin A, Baillie GS, Nicklin SA, Graham D, Szabo-Fresnais N, Krall J, Vandeput F, Movsesian M, Furlan L, Corsetti V, Hamilton G, Lefkimmiatis K, Sjaastad I, Zaccolo M. Cardiac Hypertrophy Is Inhibited by a Local Pool of cAMP Regulated by Phosphodiesterase 2. *Circ Res*. 2015;117:707-719. doi: 10.1161/circresaha.114.305892
200. Liu Y, Chen J, Fontes SK, Bautista EN, Cheng Z. Physiological and pathological roles of protein kinase A in the heart. *Cardiovasc Res*. 2022;118:386-398. doi: 10.1093/cvr/cvab008

201. Antos CL, Frey N, Marx SO, Reiken S, Gaburjakova M, Richardson JA, Marks AR, Olson EN. Dilated cardiomyopathy and sudden death resulting from constitutive activation of protein kinase a. *Circ Res*. 2001;89:997-1004. doi: 10.1161/hh2301.100003
202. Osadchii OE. Cardiac hypertrophy induced by sustained beta-adrenoreceptor activation: pathophysiological aspects. *Heart Fail Rev*. 2007;12:66-86. doi: 10.1007/s10741-007-9007-4
203. Enns LC, Bible KL, Emond MJ, Ladiges WC. Mice lacking the Cβ subunit of PKA are resistant to angiotensin II-induced cardiac hypertrophy and dysfunction. *BMC Res Notes*. 2010;3:307. doi: 10.1186/1756-0500-3-307
204. Reiken S, Wehrens XH, Vest JA, Barbone A, Klotz S, Mancini D, Burkhoff D, Marks AR. Beta-blockers restore calcium release channel function and improve cardiac muscle performance in human heart failure. *Circulation*. 2003;107:2459-2466. doi: 10.1161/01.Cir.0000068316.53218.49
205. Keller JN, Hanni KB, Markesbery WR. Impaired proteasome function in Alzheimer's disease. *J Neurochem*. 2000;75:436-439. doi: 10.1046/j.1471-4159.2000.0750436.x
206. Bi M, Du X, Jiao Q, Chen X, Jiang H. Expanding the role of proteasome homeostasis in Parkinson's disease: beyond protein breakdown. *Cell Death Dis*. 2021;12:154. doi: 10.1038/s41419-021-03441-0
207. Tomaru U, Takahashi S, Ishizu A, Miyatake Y, Gohda A, Suzuki S, Ono A, Ohara J, Baba T, Murata S, Tanaka K, Kasahara M. Decreased proteasomal activity causes age-related phenotypes and promotes the development of metabolic abnormalities. *Am J Pathol*. 2012;180:963-972. doi: 10.1016/j.ajpath.2011.11.012
208. Donohue TM, Osna NA, Kharbanda KK, Thomes PG. Lysosome and proteasome dysfunction in alcohol-induced liver injury. *Liver Research*. 2019;3:191-205. doi: https://doi.org/10.1016/j.livres.2019.11.001
209. Otoda T, Takamura T, Misu H, Ota T, Murata S, Hayashi H, Takayama H, Kikuchi A, Kanamori T, Shima KR, Lan F, Takeda T, Kurita S, Ishikura K, Kita Y, Iwayama K, Kato K, Uno M, Takeshita Y, Yamamoto M, Tokuyama K, Iseki S, Tanaka K, Kaneko S. Proteasome dysfunction mediates obesity-induced endoplasmic reticulum stress and insulin resistance in the liver. *Diabetes*. 2013;62:811-824. doi: 10.2337/db11-1652
210. Yaku K, Matsui-Yuasa I, Kojima-Yuasa A. 1'-Acetoxychavicol Acetate Increases Proteasome Activity by Activating cAMP-PKA Signaling. *Planta Med*. 2018;84:153-159. doi: 10.1055/s-0043-118806